Beamforming and scan pattern performance evaluation of rotating maritime multi-beam phased array surveillance radar

by

Lourens van Heerden

Supervised by

Prof. Daniel O'Hagan

and

Dr. Francois Schonken

Department of Electrical Engineering

University of Cape Town

Submitted to the Department of Electrical Engineering at the University of Cape Town in partial fulfilment of the academic requirements for a Master of Engineering degree.

June 2022

Declaration

1. I know the meaning of plagiarism and declare that all the work in the document, save for that which is properly acknowledged, is my own.
2. This dissertation has been submitted to the Turnitin module (or equivalent similarity and originality checking software) and I confirm that my supervisor has seen my report and any concerns revealed by such have been resolved with my supervisor.
3. I have used the IEEE convention for citation and referencing. Each contribution and quotation in this report from the work(s) of other people has been attributed, and has been cited and referenced.
4. This dissertation is being submitted for the degree of Master of Engineering in the University of Cape Town (UCT).

Signed by candidate

Signature: .....

YOUR NAME

Date: 07/06/2022 .....

Acknowledgements

First of all, I would like to thank my Heavenly Father for providing me the courage and determination to persevere throughout the challenges in life to reach my goals and dreams.

To my wife, Kumarie, daughter, Abigail and son, Leon, thank you for your support and encouragement throughout this journey - willingly sacrificing our time together on many evenings and weekends. Also to Keshet, a loyal companion sleeping at my feet, seeing me through late nights and early mornings.

To my parents, Leon and Chrissie, thank you for your encouragement, faith and inspiration.

To my supervisors, Prof. Daniel O'Hagan and Dr. Francois Schonken thank you for your guidance and support.

I would also like to show gratitude to Dr. Jacques Cilliers from the Council for Scientific and Industrial Research (CSIR) for allowing me access to the sea clutter reflectivity datasets.

Abstract

Modern naval ships face a wide spectrum of threats, from fast-moving sea-skimming missiles to slow-moving unmanned vehicles and boats. The rotating phased array naval surveillance radar provides 360° azimuth coverage at large elevation angles for early warning to initiate the appropriate action and countermeasures timeously.

This dissertation aimed to provide a simulation model to test and evaluate the effect of different beamforming and scan patterns on the detection performance of different possible targets in the maritime environment per antenna rotation. MATLAB, with various Phased Array Toolbox objects, was used as the platform to create the simulation model. A wide variety of variables were adjusted to test the effect on detection performance per rotation against a specified target. It distinguished between air (fast) targets with a medium Pulse repetition frequency (PRF) waveform and surface (slow and low) targets with a low PRF waveform. Coherent and non-coherent (surface only) processing algorithms were used. Complex clutter data sets from the CSIR Fynmeet sea clutter measurement trial were adapted according to the Georgia Institute of Technology (GIT) model, clutter area model and radar range equation to be inserted into each pulse. The output was a detection table for the air and surface channel for the evaluated sector per rotation. In order to determine detection performance, multiple rotations and target scans with clutter data offsets were required.

The simulation model provided insight into the effect of beamforming and scan patterns on the detection performance of both fast and slow-moving targets. It was found that with coherent fast target air surveillance and sufficient clutter suppression, a fast-moving target could be detected with a detection probability of 1 and a false alarm probability of 0. This could be achieved with a single or dual-axis stacked beam. In a single axis stacked beam, only non-coherent integration of low quantity, low PRF pulse bursts could be used for the surface channel as time resources were limited to a single beamwidth. In this case, cell averaging constant false alarm rate (CA-CFAR) detection provided better results in a homogeneous and small target signal-to-clutter ratio (SCR) environment (as was the case at far ranges). The detection probability was 1 and false alarm probability was 0.03. In a spiky and large target SCR environment (as was the case at near ranges), constant threshold detection performed better. The detection probability was 1 and false alarm probability was 0. High Doppler resolution coherent integration of a large number of low PRF pulses could be used in a dual-

axis beam for the surface channel. This type of detection provided results comparable to non-coherent detection. The detection probability was 1 and false alarm probability was 0.02 at far ranges, and 1 and 0.06 respectively at near ranges. When the target's Doppler frequency was within the clutter's Doppler spectrum, the target was not detectable.

Contents

List of Figures

List of Tables

Nomenclature

Abbreviations

2D	Two dimensional
3D	Three dimensional
AAW	Anti-air warfare
ADC	Analog-to-digital converter
ASU	Anti-surface warfare
CA-CFAR	Cell averaging constant false alarm rate
CFAR	Constant false alarm rate
CNR	Clutter-to-noise ratio
COO	Concept of operations
CPI	Coherent processing interval
CSIR	Council for Scientific and Industrial Research
CUT	Cell under test
FFT	Fast Fourier transform
GaN-on-SiC	Gallium Nitride on Silicon Carbide
GIT	Georgia Institute of Technology
GOCA-CFAR	Greatest-of cell averaging constant false alarm rate
MLE	Maximum-likelihood estimation

NCPI	Non-coherent processing interval
PDF	Probability density function
PRF	Pulse repetition frequency
PRI	Pulse repetition interval
RCS	Radar cross section
RF	Radio frequency
SCR	Signal-to-clutter ratio
SINR	Signal-to-interference-plus-noise ratio
SLC	Sidelobe canceller
SNR	Signal-to-noise ratio
SSM	Surface-to-surface missile
T/R	Transmit/receive
TWT	Travelling wave tube

Symbols

α	CFAR constant
α_{CA}	CA-CFAR constant
α_{GO}	GOCA-CFAR constant
ΔR	Range resolution
$\hat{f}_{GO,lag}$	GOCA-CFAR lagging window interference power estimate
$\hat{f}_{GO,lead}$	GOCA-CFAR leading window interference power estimate
$\hat{g}$	CFAR interference power estimate
$\hat{g}_{CA}$	CA-CFAR interference power estimate
$\hat{g}_{GO}$	GOCA-CFAR interference power estimate
λ	Wavelength

$\mathbf{W}_a$	Planar array element signal weights
$\mathbf{W}_h$	Horizontal array element signal weights
$\mathbf{W}_v$	Vertical array element signal weights
ϕ	Phase of a plane wave
ϕ_{gr}	Grazing angle
σ^0	Clutter area reflectivity
σ_c	Clutter RCS
σ_n^2	Array element noise power
σ_s^2	Array element signal power
σ_ϕ	Roughness parameter
θ_w	Wind direction relative to look direction
A_c	Illuminated clutter area
A_i	Multipath interference parameter
a_n	Weight at n^{th} element
A_u	Wind direction dependence
A_w	Sea state variation
A_{mn}	Signal at $\mathrm{mn}^{\mathrm{th}}$ element
az	Antenna relative azimuth angle
az_s	Antenna relative beam steering azimuth angle
az_{ship}	Ship relative azimuth
B	Bandwidth
b	Scale parameter
B_{az}	Azimuth beamwidth
B_{el}	Elevation beamwidth

c	RF wave propogation speed
E	Array field pattern *or* Signal envelope
E_a	Array factor
E_e	Element field pattern
E_n	Array noise factor
el	Antenna relative elevation angle
el_s	Antenna relative beam steering elevation angle
el_{ship}	Ship relative elevation
F	Noise figure
f_s	Sampling frequency
G	Gain *or* Guard cell
G_a	Array gain
h	Height
$h_{1/3}$	Significant wave height
h_{av}	Average wave height
k_B	Boltzmann's constant
P	Single trial probability
P_c	Cumulative probability *or* Clutter average power
P_d	Probability of detection
P_n	Array noise power
P_s	Array signal power
P_t	Transmit power
$P_{d_{GO}}$	Probability of detection for GOCA-CFAR
P_{dc}	Cumulative probability of detection

$P_{fa_{CA}}$	Probability of false alarm for CA-CFAR
$P_{fa_{GO}}$	Probability of false alarm for GOCA-CFAR
P_{fac}	Cumulative probability of false alarm
P_{fa}	Probability of false alarm
PRF	Pulse repetition frequency
PRF_b	Base pulse repetition frequency
R	Range *or* Reference cell
R_b	Range bin range
R_{max}	Maximum range
R_{ua}	Unambiguous range
s	Sea state
$SINR$	Signal-to-interference-plus-noise ratio
SNR_a	Array signal-to-noise ratio
SNR_e	Element signal-to-noise ratio
T	Pulse width *or* Threshold *or* Temperature
U	Wind velocity
v	Shape parameter
v_{max}	Maximum velocity
v_{ua}	Unambiguous velocity

Chapter 1

Introduction

1.1 Background

In the wake of severe worldwide defence budget cuts, naval combat system engineers are required to follow thorough requirement and analysis processes. This is done to deliver a naval ship that will fulfil intended missions and roles at the minimum cost. A typical design process broadly follows steps, as shown in Fig 1.1, and is described in the following subsections [1].

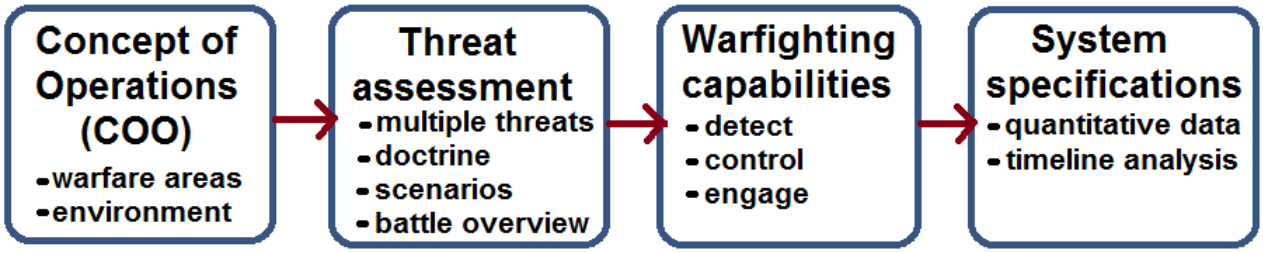

Fig. 1.1. Combat system specification and selection process.

1.1.1 Concept of operations

A Concept of operations (COO) is prepared which describes how the Navy intends to deploy the ship with an associated mission profile. A COO for a modern multi-mission naval ship, as was used in this study, typically includes conventional 'blue-water' operations, but also places much emphasis on littoral warfare operations, such as anti-piracy missions in coastal areas or maritime security and maritime defence missions encountering asymmetric threats.

1.1.2 Threat assessment

A threat assessment, applicable fleet doctrine, scenarios and battle overviews are produced. A multi-mission ship operating in the 'blue-water' and littoral warfare operational areas can encounter a wide spectrum of threats [2].

At the low end of the threat spectrum, small slow-moving targets like unmanned aerial vehicles (UAVs) and manned or unmanned small boats are undertaking threatening tasks against bigger naval vessels. The small slow-moving threat is particularly challenging because of the effects sea clutter has on radar-based target discrimination.

At the high end of the threat spectrum, modern sea skimming surface-to-surface missiles (SSM) and high-diving anti-ship missiles are being introduced with reduced radar cross sections (RCS) and increasingly higher acceleration manoeuvres. The sea-skimming threat is particularly challenging because its detection is limited by the radar horizon, resulting in limited reaction time for defensive actions. A high track update rate is required for accurate track maintenance of this type of target.

1.1.3 Required war fighting capabilities

A broad definition of the required war fighting capabilities in the applicable warfare areas is then created. Familiar functions such as detect, control, and engage are used as outlined in Table 1.1.

Table 1.1. Conceptual war fighting capabilities.

Warfare Areas / Function	Anti-surface warfare (ASU)	Anti-air warfare (AAW)
Detect	Detect surface targets	Detect air targets
Control	Track surface targets	Track air targets
Engage	Engage surface threats	Engage air threats with soft or hard kill effectors

1.1.4 System specifications

Quantitative data are added to the war fighting capabilities to formulate the performance requirements and eventually a system specification for each warfare area. Quantitative data is typically derived from various sources. For example, exploration of different subsystems already available on the market, environmental and geographical factors (for example the radar horison), the typical threat profile and other factors.

An important tool in this process is the use of weapon channel timeline analysis. Fig 1.2 is an illustration of an arbitrary timeline for a ship point defence against a missile threat flying at $333\,m/s$. If, for example, the missile characteristics are known, this data can be used along with knowledge of the ship's decision making system, fire control systems and own weapon systems to determine the initial detection and tracking performance requirements of the surveillance radar (illustrated in Fig 1.2 as the timeline between range A and B). From Fig 1.2, it can be seen that the surveillance radar must have performed detection, tracking and classification of the threat when it reaches a range of $21\,km$ (range B) in order to allow enough time for a correct kill plan assessment, high accuracy tracking and weapon engagement. This of course is a single arbitrary example. In practise a variety of timelines with different threats, sensor and weapon combinations will be analysed.

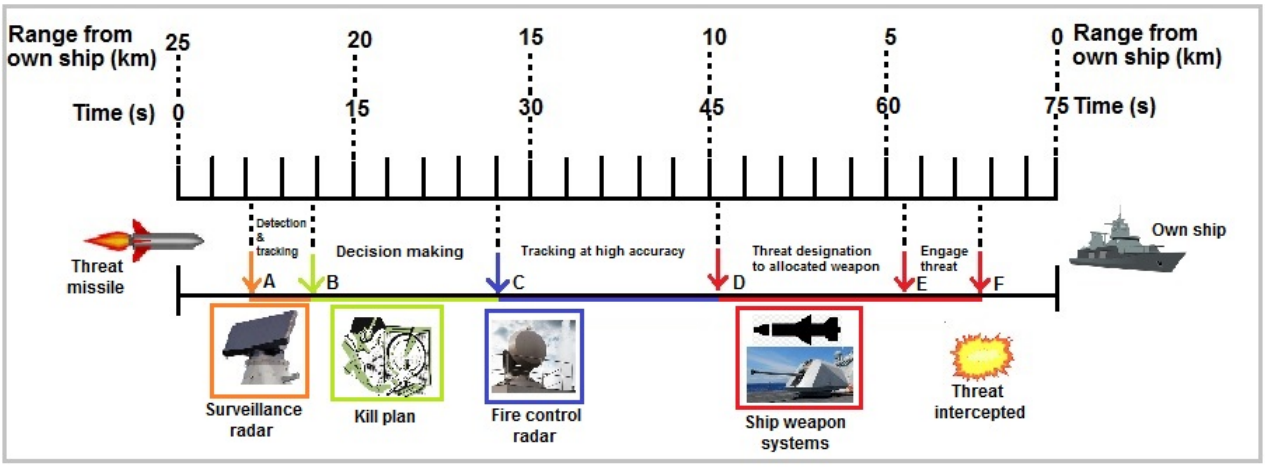

Fig. 1.2. Arbitrary ship weapon channel timeline for point defence against a missile threat.

For slow asymmetric threats at the low end of the spectrum like UAVs and small boats, the initial detection and tracking range can be much less due to the slower speed of the target. This will allow sufficient time for further classification by optical systems and possible engagement if required. Asymmetric threats might not always pose a direct danger to the ship, and the range requirement could, for example, be extended to sufficiently perform constabulary duties against these targets over an extended area. A brief example overview of some quantitative system specifications elements, applicable to this study, for the different warfare areas is outlined in Table 1.2. The total elements can exceed 200 for complex warships.

Table 1.2. System specification elements example.

Air detection	
System specification	Threshold value
Detection probability (P_d) > 0.9 for a SSM with the following characteristics: $speed \leq 333\,m/s$ $RCS \geq 0.1\,m^2$ (SW 0) $altitude \geq 10\,m$ $sea\ state \leq 3$ Probability of false alarm (P_{fa}) $\leq 1 \times 10^{-5}$	$23\,km$
$P_d > 0.9$ for a UAV with the following characteristics: $speed \leq 15\,m/s$ $RCS \geq 0.05\,m^2$ (SW 0) $altitude = 10\ to\ 100\,m$ $sea\ state \leq 3$ $P_{fa} \leq 0.05$	$15\,km$
Surface detection	
System specification	Threshold value
$P_d > 0.9$ for a small boat with the following characteristics: $speed \leq 11\,m/s$ $RCS \geq 3\,m^2$ (SW 0) $sea\ state \leq 3$ $P_{fa} \leq 0.05$	$10\,km$

1.2 Problem statement

The surveillance radar is the logical choice as the primary subsystem for initial air detection and tracking against the SSM threat. Sufficient Doppler processing and clutter suppression provide the naval surveillance radar with the capability to meet initial detection requirements of a fast-moving target, even with a relatively low RCS. Modern phased array three-dimensional (3D) naval surveillance radars make use of state of the art front-end technology, which includes active transmitters and receivers on element or subarray level, as well as digital beamforming technology. These technologies enable the use of multiple simultaneous stacked beams covering a wide elevation angle and, in some cases, azimuth too. Additionally, some modern phased array radars can actively scan off antenna boresight multiple times on a target of interest during a sector scan and rotation to increase the track update rate and accuracies. These radars provide a considerable increase in radar resources such as time, energy, phase and processing budgets compared to, for example, older pencil beam phased array systems [3].

For a surveillance radar optimised for air detection and tracking of high speed manoeuvring

targets, the detection and tracking of slow air and surface targets masked in sea clutter is a conflicting requirement. Reliable and accurate instantaneous Doppler measurement can possibly increase the probability to detect and track slow-moving, low flying objects such as modern UAVs and small boats in sea clutter environment. But increasing the Doppler resolution requires long observation times to achieve good clutter-target discrimination. This time and energy directed at low elevation angles, can compromise the ability to scan the surveillance volume rapidly for detection of fast-moving air targets. Fig 1.3 illustrates the shorter reaction time required for the fast-moving air targets which conflicts with the longer observation time required for slow-moving air and surface targets.

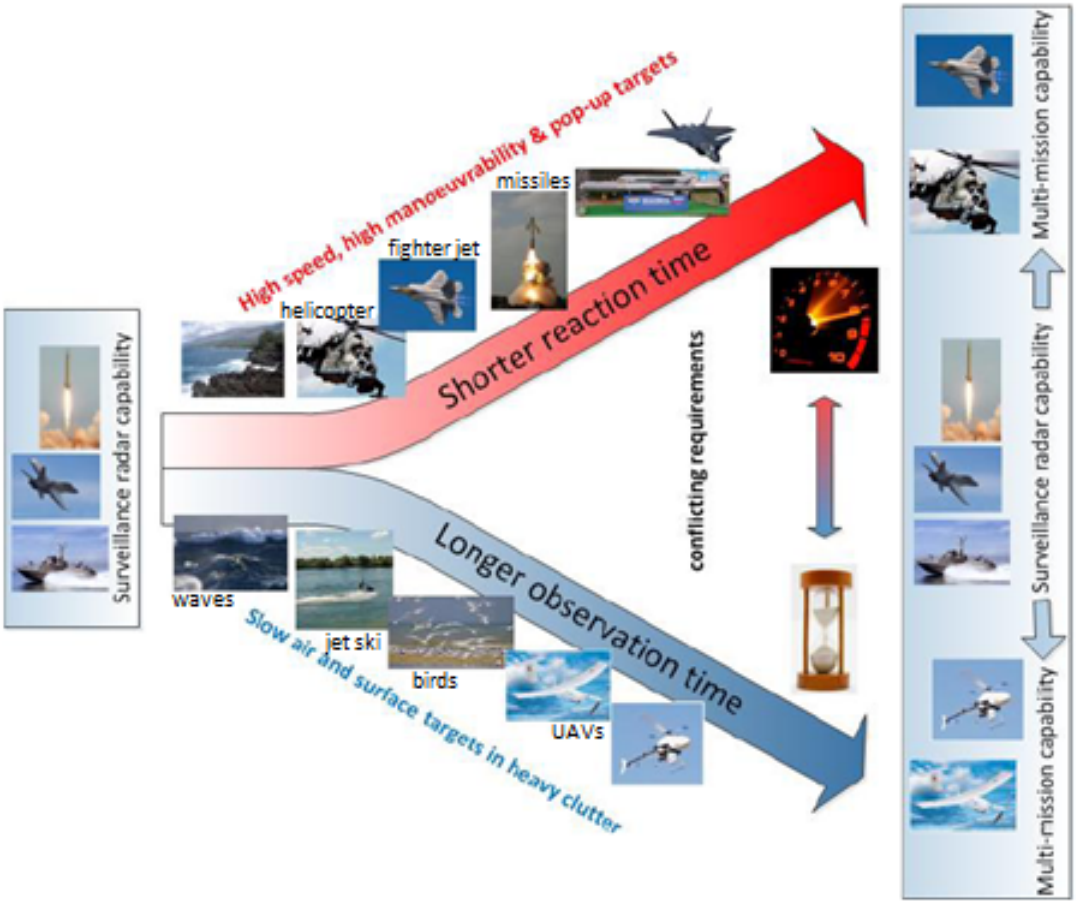

Fig. 1.3. Operational threats and the conflicting requirements they pose to a modern surveillance radar [2].

A model is therefore required to evaluate the effect of different beamforming and scan patterns on the detection performance of the maritime surveillance radar. This need to be applied to both fast-moving air targets and/ or slow air and surface targets in a single scan.

1.3 Objectives of the study

The first objective of this dissertation was to create a simulation model in MATLAB to evaluate the detection performance of different beamforming and scan pattern techniques for rotating maritime multi-beam electronically steered array surveillance radars.

The second objective was to obtain an idea of realistic system detection specifications for both low and high end threats for a multi-mission naval ship by means of the simulation. Furthermore, the feasibility of utilising a single surveillance radar to perform these diverse functions was evaluated.

The detection performance was measured against an SSM and UAV for a multi-mission naval ship. For the purpose of this dissertation, a typical SSM was considered as a priority threat. The air detection range performance was therefore specified from the arbitrary timeline for this target. Appropriate transmit powers were determined for the beamforming and scan patterns to detect this target at the required range. A detection range performance for the lower end asymmetrical threats was then derived based on the available radar transmit power in the presence of real clutter data adapted to fit the range profile.

1.4 Scope and limitations

The dissertation and simulation model was limited to a 3D pulse-Doppler naval surveillance target and acquisition radar, with a rotating electronically steered phased array antenna utilised for point defence. Spatially, a single wide transmit beam and multiple simultaneous receive beams covering the transmit area were used. The multi-beam feature was established by means of digital beamforming (distributed receivers). Modern phased array naval surveillance radars often have different modes of operation to optimally track an identified threat. For this study, a general surveillance mode to detect the targets of interest was evaluated with appropriate radar operating parameters. The study didn't limit the array architecture to a certain type (for example a subarray digital or element digital array), but rather discussed possible array architectures that could achieve the scan and beamforming techniques.

There were a considerable number of variables applicable to this study and simulation model. Some significant independent variables for this research topic and simulation are target RCS models, target speed, target altitude, sea clutter data, false alarm probability, transmit power, pulse repetition intervals (PRIs), coherent processing interval (CPI) length, beamforming (limited to single or multiple stacked beams) and beam scanning techniques. The most significant dependent variable was the detection performance. Some significant constant radar operating parameters that were used, are the antenna size, antenna rotation rate, receive beamwidth, maximum elevation angle, antenna gain, frequency, pulse widths, receiver noise, bandwidth and matched filtering techniques.

Through the simulation model, different beamforming and scan pattern techniques could be compared in a reconfigurable manner. The idea was not to create a complete real world radar simulation, although a considerable number of radar features were included. Some of the limitations of the study and simulation model were that:

- It didn't take into consideration the impact of the atmosphere and is thus a free space path loss simulation. This included effects such as attenuation and ducting.
- It didn't consider the effect of multipath.
- It only focused on detection performance, and there weren't any parameter estimation analysis such as target bearing and elevation accuracy estimation.
- It didn't include any tracking algorithms for testing of track formation.
- The clutter data used was for a staring radar at a higher altitude than a ship, not a rotating radar on a ship's mast, which can introduce some additional clutter effects and decorrelation.

1.5 Plan of Development

Chapter 1 describes the objectives of the study. Chapter 2 focuses on important concepts and principles that are included in the simulation model. Chapter 3 focuses on the design of the radar simulation model. Chapter 4 provides results of some simulations and discussions of these results in line with the objectives of this study.

Chapter 2

Theory

This chapter focused on important concepts and principles that were included in the simulation model. Some fundamental concepts of phased array theory, recent technological advances and phased array architectures were discussed. The performance attributes of these architectures were compared. The chapter further included concepts such as sea clutter, beam pattern synthesis, constant false alarm rate (CFAR) detectors and ambiguity resolution.

2.1 Phased array theory

A planar array is capable of steering a beam in two dimensions. For the purpose of this study, a spherical reference coordinate system was used where the coordinates range (R), azimuth (az) and elevation (el) defined the position of a target. The azimuth angle was the angle between the x-axis and the orthogonal projection of the wave vector onto the xy-plane. The angle was positive in going from the x-axis toward the y-axis. Azimuth angles were between $-180°$ and $180°$. The elevation angle was the angle between the wave vector and its orthogonal projection onto the xy-plane. The angle was positive when going toward the positive z-axis from the xy plane. Elevation angles were between $-90°$ and $90°$. This is illustrated in Fig 2.1.

In Fig 2.1 the antenna elements are located on the zy-plane. This implies that the boresight was on the x-axis. This was the default location of antenna elements in the coordinate system in the MATLAB phased array toolbox, which did not accommodate for the rotation of the antenna. However, the antennas simulated in this study needed to be rotating. The simulation model accomplished a pseudo rotation by rotating the target around the antenna. The study thus referred to an antenna relative coordinate system (with the boresight pointing towards the positive x-axis), as per Fig 2.1. The antenna relative beam was referenced to the ship structure and was called the ship relative coordinate system (with the bow pointing towards the positive x-axis) as per Fig 2.2. The antenna relative angles were denoted simply as 'az' and 'el' while the ship relative angles were denoted as 'az_{ship}' and 'el_{ship}'. This is illustrated in Fig 2.2.

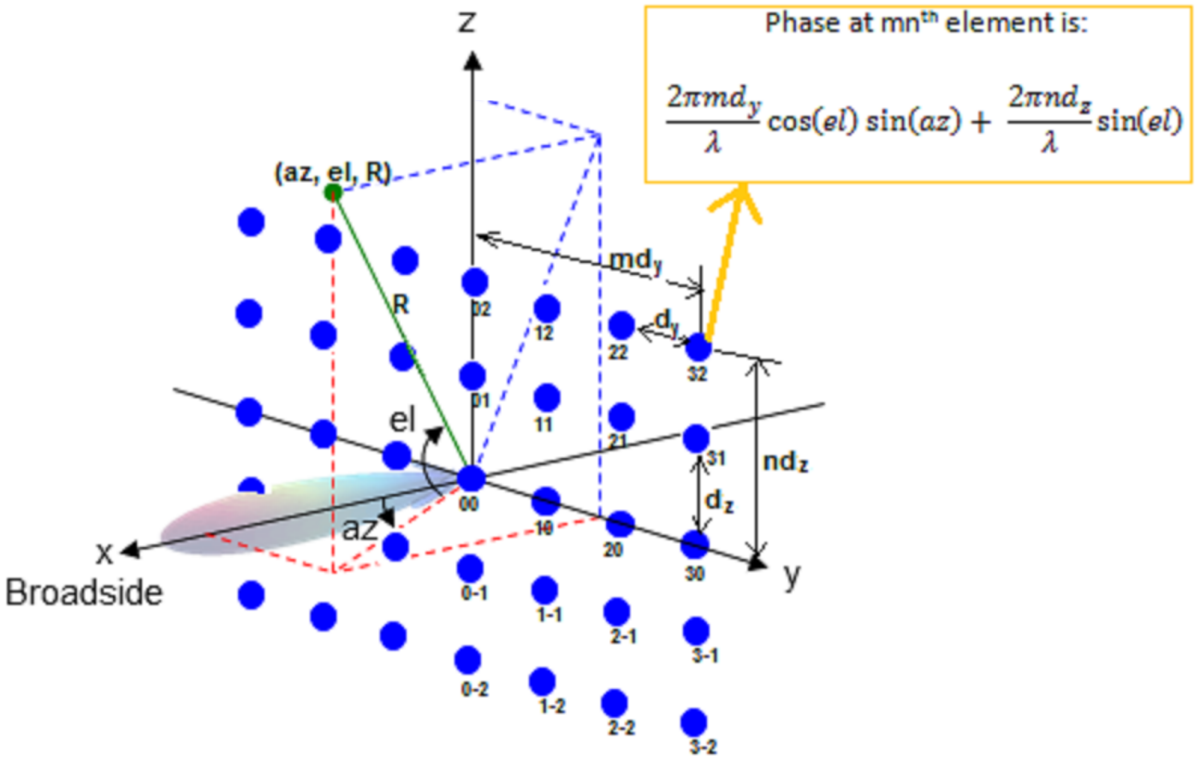

Fig. 2.1. Planar array antenna relative coordinate system, element geometry and phasing.

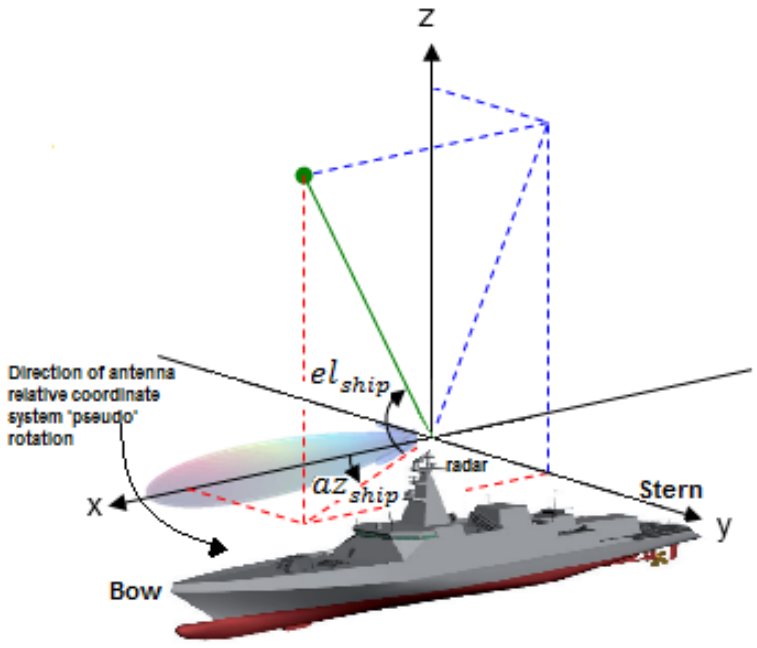

Fig. 2.2. Ship relative coordinate system.

For the planar array in Fig 2.1 it was shown that the phase at the mn$^{\text{th}}$ element for a plane wave, with wavelength λ approaching the array at angle az and el was:

$$\phi(m,n) = \frac{2\pi m d_y}{\lambda}\cos(el)\sin(az) + \frac{2\pi n d_z}{\lambda}\sin(el) \tag{2.1}$$

where d_y and d_z were the y-axis and z-axis distances respectively between consecutive elements. The phased array formed a pattern by adding weights (amplitude and phase) to each element and the summation of the element signals. Through further mathematical manipulation the array factor for an uneven number of elements symmetrical in the y-axis direction ($2M+1$ elements) and z-axis direction ($2N+1$ elements) was determined as:

$$E_a(az,el) = \sum_{m=-M}^{M}\sum_{n=-N}^{N} |A_{mn}| e^{\frac{j2\pi}{\lambda}[md_y(\cos(el)\sin(az)-\cos(el_s)\sin(az_s))+nd_z(\sin(el)-\sin(el_s))]} \tag{2.2}$$

where $|A_{mn}|$ was the amplitude of the signal at the mn$^{\text{th}}$ element, az_s and el_s were the azimuth and elevation steering angles respectively. The formula could be adapted for an even number of elements symmetical in the y- and z-axis directions ($2M$ or $2N$ elements). In general, the total array field pattern was the product of the element field pattern and the array factor:

$$E(az,el) = E_e(az,el)E_a(az,el) \tag{2.3}$$

where E_e was the element field pattern.

2.2 Phased array architectures

Throughout even the earliest days of radar, designers faced problems that required some means of moving the beam other than physically moving the whole antenna [4]. Phased array systems provide a solution by means of electronically pointing an antenna beam. Some significant technological advances in this field from recent times are discussed in the following subsection.

2.2.1 Recent technological advances

Transmitter technology evolved from high-power centralised transmitters, typically klystron vacuum tube amplifiers or travelling wave tube (TWT) amplifiers, capable of outputting hundreds of kilowatts of peak power at microwave frequencies to state of the art solid state transmitter modules, typically Gallium Nitride-on-Silicon Carbide (GaN-on-SiC) based high power transistors [5]. The solid state transmitters not only provide a considerable improvement in reliability, but also provide the capability of a distributed transmitter architecture. In the early days of solid state distributed devices, there was concern about coherence, uniformity, and

reliability. But over time constant improvement reduced the risk with large yields and reduced costs. This concern is illustrated quite fittingly in Fig 2.3. Today, solid state high power transmit amplifiers, low-loss radio frequency (RF) switches, low-noise receive amplifiers, phase shifters, and variable attenuators are integrated at each element radiator (or per subarray) into what are commonly known as transmit/receive (T/R) modules [6]. A typical T/R module block diagram is shown in Fig 2.4. Depending on the array architecture, components like the phase shifter and beamformer might be virtually implemented after digitisation.

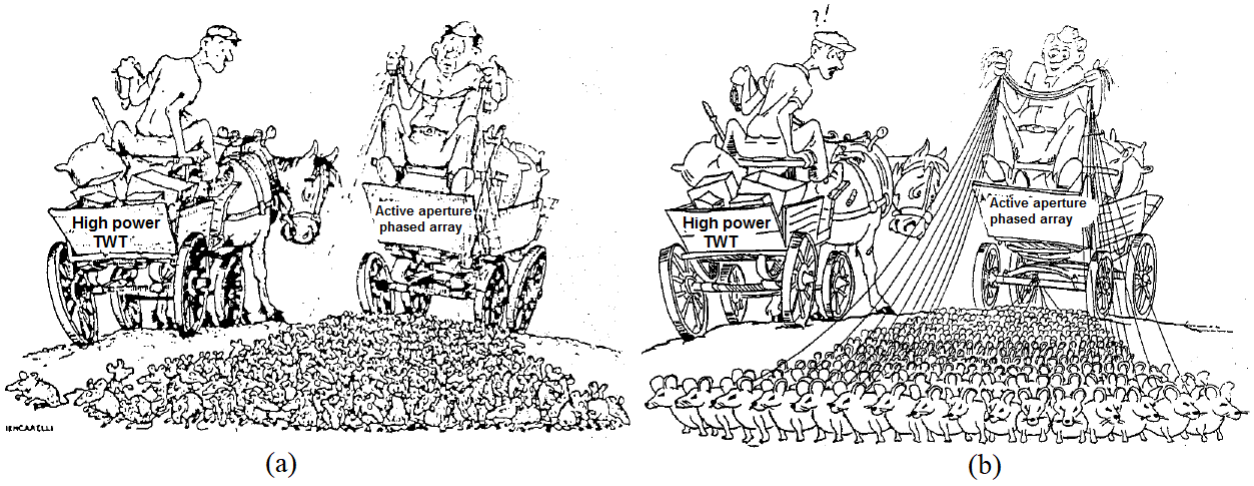

Fig. 2.3. (a) Initial concerns about coherence and uniformity for solid state modules was (b) undone through improvement in technology [4].

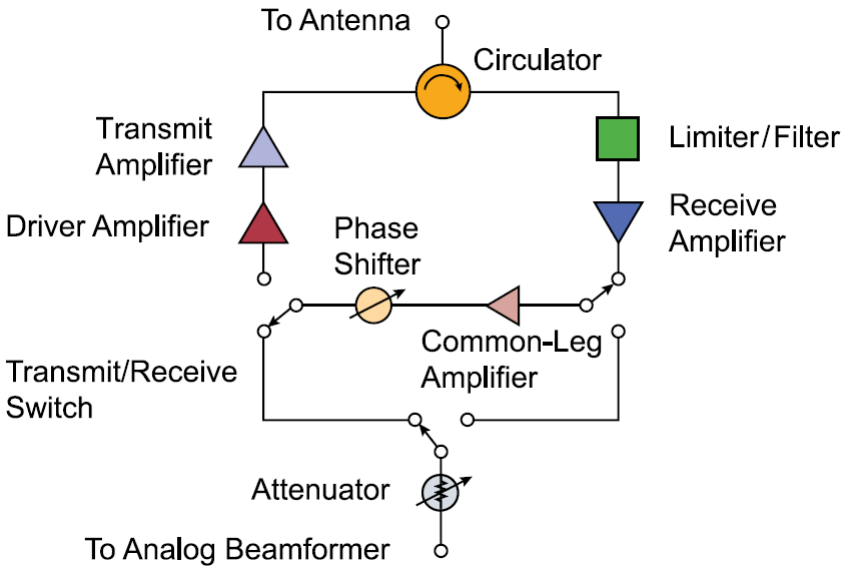

Fig. 2.4. T/R module block diagram [5].

Improvement in the dynamic range and the ability to handle greater processing loads, analog-

to-digital converters (ADCs) have allowed the digital processing march to continue further up the radar system to the subarray and even individual antenna elements. Hardware elements such as waveguides, beamformers and phase shifters are now being implemented in the virtual domain. This allows the possibility to create and point as many beams simultaneously as the available digital processing power can allow, with improved reliability.

2.2.2 Types of array architectures

Four general architecture categories of phased arrays can be described as analog passive, analog active, subarray digital and element digital. An analog passive array is one in which the array is fed by a centralised high-power transmit amplifier, a single receiver, an analog power-combining network and an analog phase shifter at every subarray or element (Fig 2.5 (a)). An analog active array is one where the transmit power amplifiers, low-noise amplifiers, and phase shifters are distributed throughout the array at subarray or element level - usually through T/R modules (Fig 2.5 (b)). Subarray digital and element digital arrays are active (distributed transmit amplifier) and distributed receiver arrays where RF signals are converted to digital signals at the subarray or element level respectively, with the beamforming performed by a digital signal processor (Fig 2.5 (c) and (d)).

In practise, phased array radar systems might not strictly follow these architectures, and a system could be a hybrid combination of different architectures, for example a system could comprise of an analog passive transmit channel with a digital subarray receive channel. Fig 2.6 shows a timeline plot for the evolution that phased array architecture technologies have undergone over the past 55 years in the United States Defence environment [5].

2.2.3 Array architecture performance comparison

Various radar attributes for the different array architectures can be compared, for example antenna patterns, beam control (including beam-shape flexibility, multiple simultaneous beams and adaptive interference suppression), instantaneous dynamic range, in-band linearity, the impact of phase noise on clutter attenuation and angle measurement accuracy [6]. The antenna patterns, beam control and angle estimation accuracy (for beam summation) will be briefly discussed in this subsection as these form a significant part of the study and simulation. The rest of the attributes will not be discussed but also play a significant role in array architecture performance.

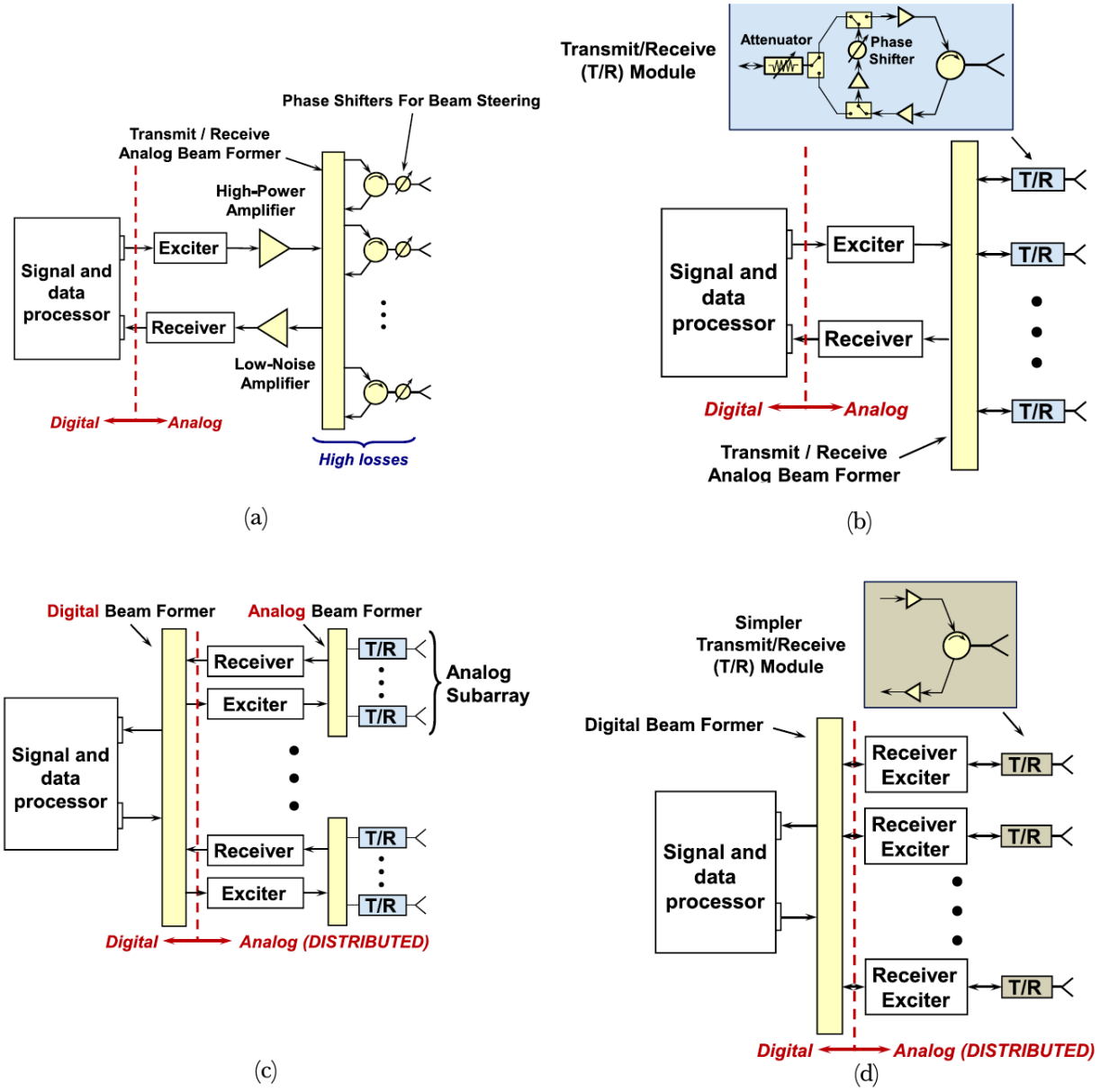

Fig. 2.5. Simplified block diagrams showing key features of the phased array radar architecture evolution in the last few decades: (a) analog passive phased arrays; (b) analog active phased arrays, including the basic features of a T/R module; (c) subarray digital arrays, which use the same T/R modules of active phased arrays; and (d) element digital arrays, which do not require phase shifters, variable attenuators or additional amplification in the T/R module [6].

Analog arrays (passive or active)

Other than the ability to steer beams in space, the array pattern performance (sidelobe levels and beam shapes) is generally fixed by a hardwired design. This leaves little flexibility to

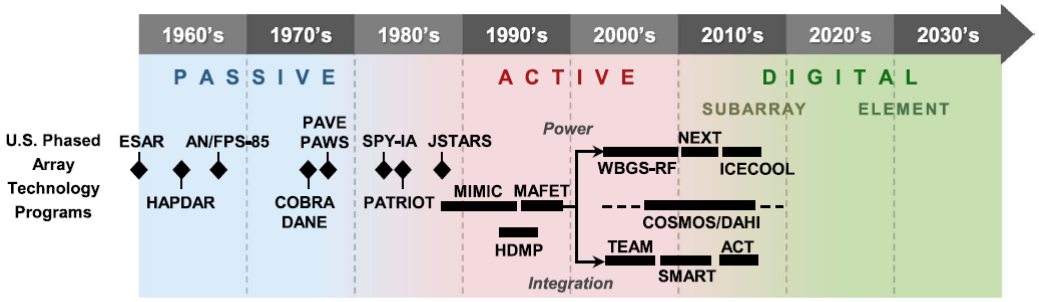

Fig. 2.6. US phased array technology development programs timeline [5].

optimise performance for various radar modes or operating conditions, especially as these evolve over the life of the radar. Furthermore, very few beams can be formed simultaneously and will require additional hardware manifolds for each beam [6].

For angle estimation, analog array radars typically require three separate low power beamforming hardware manifolds on receive to produce sum, azimuth difference, and elevation difference beams for conventional monopulse tracking. Alternatively, angle estimation could be done through centroid tracking from differential angle scanning.

An example analog passive array antenna system can consist of horizontal (along the y-axis) subarray planks stacked on top of each other in the vertical (z-axis) direction. Each horizontal subarray can have its own elements and beamformer with a fixed phase to steer the beam in azimuth and elevation to zero degrees. Each subarray has a phase shifter to control the phase. The example array is illustrated in Fig 2.7. Comparing the fixed azimuth steering angle (hardwired beamforming network) of zero degrees for the subarray with equation 2.2, the steering phase along the y-axis (m-element direction) will be zero and the array factor was reduced to:

$$E_a(az, el) = \sum_{m=-M}^{M} \sum_{n=-N}^{N} |A_{mn}| e^{\frac{j2\pi}{\lambda}[md_y(\cos(el)\sin(az)) + nd_z(\sin(el) - \sin(el_s))]} \tag{2.4}$$

From equation 2.4, it was seen that the array factor steering only depends on the elevation angle el_s and implied a boresight beam that can only be steered in elevation. Furthermore, there was only one instantiation of the array factor, which implies only one steerable beam. Fig 2.8 is an array power pattern simulation (in linear scale) for transmit and receive and illustrates how this type of rotating phased array antenna and beam could work on a ship as surveillance radar. While the antenna rotates, the elevation volume is scanned with consecutive elevation beam positions. It is clear that the beam dwell time on a target is very little for this type of array, however all the energy is concentrated within the pencil beam. Some examples of passive arrays used on naval ships are the Hensholdt TRS-3D (Fig (a)) [7], Thales MRR [8] and fixed panel Lockheed Martin AN-SPY 1 (Fig 2.9 (b)) [5].

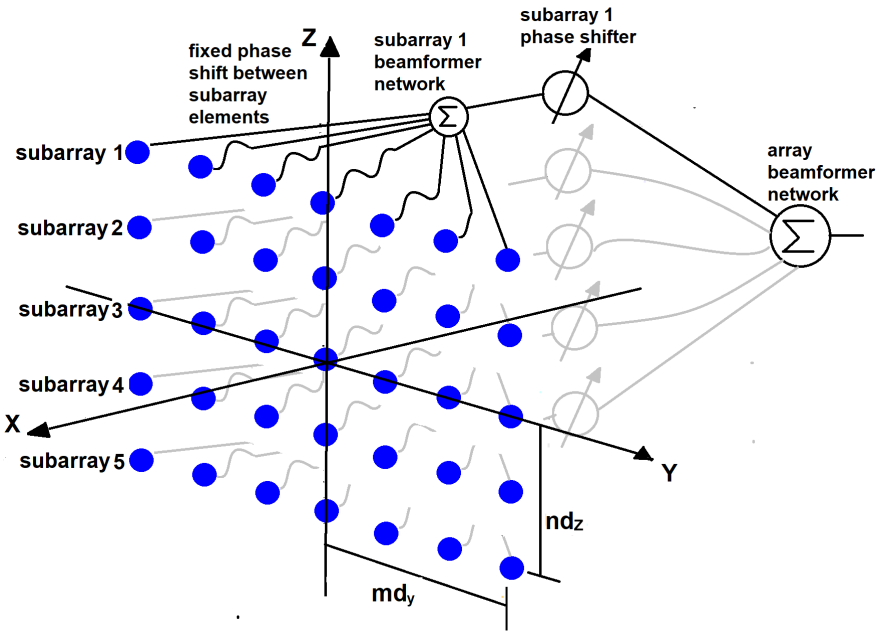

Fig. 2.7. Passive analog array system with phase shifters at subarray level.

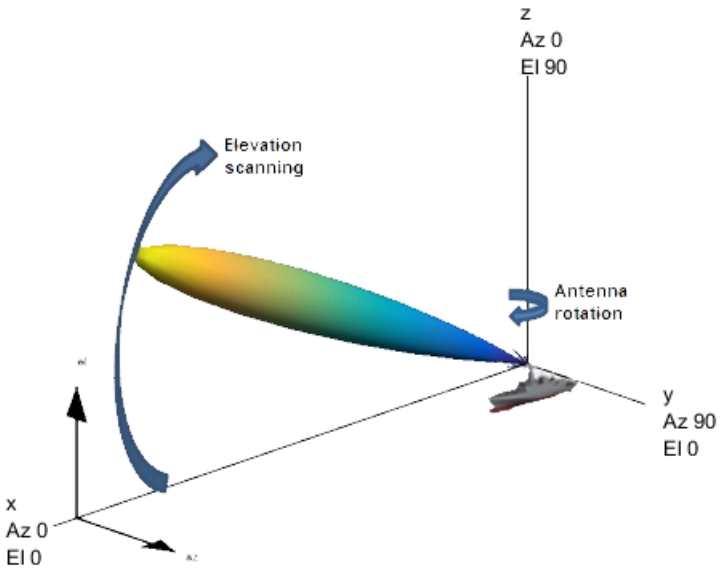

Fig. 2.8. Passive analog array transmit and receive power pattern simulation (in linear scale) of a pencil beam on a rotating ship surveillance radar.

Subarray digital arrays

Subarray digital arrays are often used to provide digital array capability while reducing the number of transceivers and/or ADCs. These arrays can produce multiple receive beams;

Fig. 2.9. Pictures of the (a) Hensholdt TRS-3D installed on the Finnish Hamina class fast attack craft [9] and (b) fixed panel Lockheed Martin AN-SPY 1 installed on the United States Ticonderoga class cruiser [10].

however, the beams are spatially constrained to a single axis stacked along the steered subarray beam. The beam pattern of a subarray digital array can be thought of as the product of the element pattern, the subarray pattern, and the array factor of the array of subarrays. It is furthermore possible to partially reconfigure the overall beam shape by digitally adjusting the weights at subarray level - again this is constrained by the subarray beam. Element analog phase shifters can be used to steer the subarray patterns to the desired direction. Multiple beams are then created digitally at the array factor level [6].

For angle estimation, subarray digital array radars typically can perform monopulse techniques along the axis where the digital beams are stacked without the need for separate hardware manifolds for the sum and difference channels. Alternatively, other more accurate angle estimation techniques can be used, for example, maximum-likelihood estimation (MLE) from measurements taken from multiple simultaneous beam offsets. Angle estimation along the perpendicular axis to the axis where the digital beams are stacked, is normally limited to conventional methods like centroiding [6].

An example of a subarray digital array antenna system can consist of T/R modules (with phase shifters) at element level. Horizontal subarrays (along the y-axis) are stacked on top of each other in the vertical (z-axis) direction and each subarray has its own beamformer network. The subarray signals are then digitised for digital phase shifting and array summation. This example array is illustrated in Fig 2.10.

The “one time per pulse” hardware azimuth steerable angle for the element level phase shifters (subarray beam steering angle along the y-axis (m-element direction)), and the “multiple per

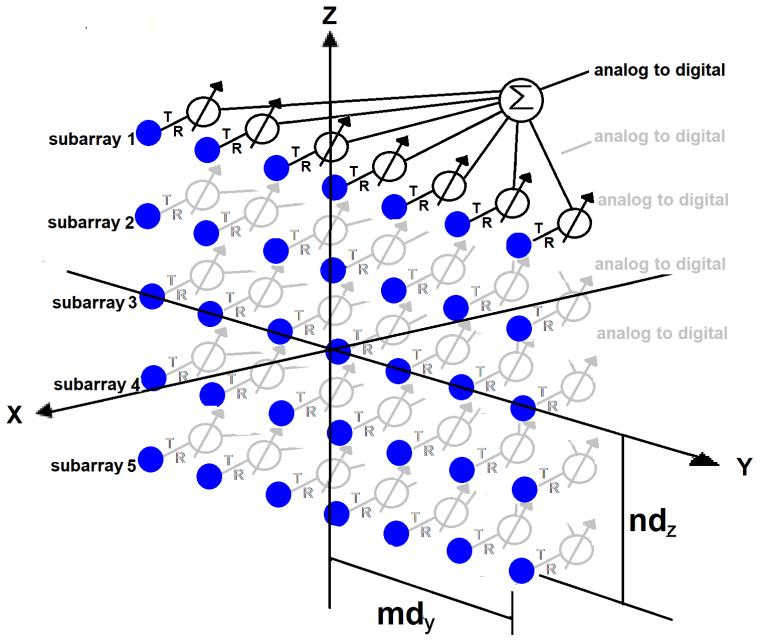

Fig. 2.10. Subarray digital array with T/R modules (including phase shifters) at element level. The subarray beamformer networks will each run into an analog to digital converter. The subarray phase shifters and array beamformer can be implemented digitally.

pulse" digital elevation steerable angles for the subarray phase shifters (along the z-axis (n-element direction)) were compared with equation 2.2. The array factor was then written as:

$$E_{ai}(az, el) = \sum_{m=-M}^{M} \sum_{n=-N}^{N} |A_{mn}| e^{\frac{j2\pi}{\lambda}[md_y(\cos(el)\sin(az) - \cos(el_{s1})\sin(az_{s1})) + nd_z(\sin(el) - \sin(el_{si}))]} \quad (2.5)$$

In equation 2.5, subscript $i \in [1, p]$ denoted the beams that are digitally formed and p denoted the number of beams. Fig 2.11 (a) is an array receive power pattern simulation (in a linear scale) of multiple beams and illustrates how this type of rotating phased array antenna and beam could work on a ship as surveillance radar. While the antenna rotates, the elevation volume is searched with multiple simultaneous elevation beams digitally formed. Fig 2.11 (b) is an array transmit power pattern simulation (in a logarithmic scale), formed through particular adjustment of the weights, which covers the complete elevation volume of interest. The reason for using a linear scale in Fig 2.11 (a) (versus a logarithmic scale in Fig 2.11 (b)) was to reduce the relative size of the large number of total sidelobes, which will clutter the figure.

It was seen from equation 2.5 that the phase steering terms $\cos(el_{s1})$ and $\sin(az_{s1})$ along the subarray elements (m-direction) could only be adjusted for the first receive beam. This implied that for $az_{s1} \neq 0$, as the phase steering term $\sin(el_{si})$ was adjusted digitally for a next elevation

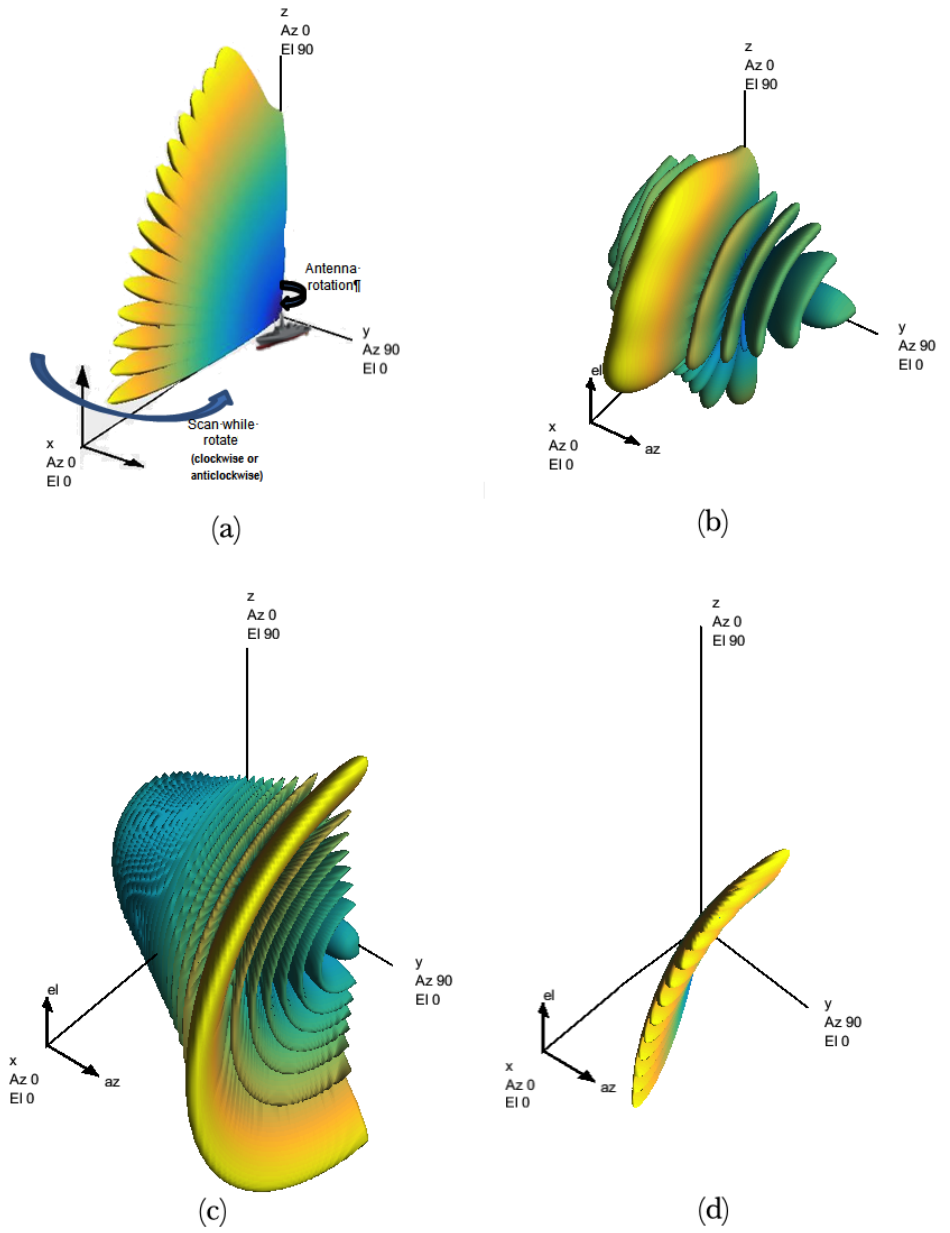

Fig. 2.11. Subarray digital array beamforming and scan pattern simulations: (a) Subarray digital array receive power pattern simulation (in linear scale) of stacked beams for a rotating ship surveillance radar; (b) Subarray digital array transmit power pattern simulation (in logarithmic scale); (c) Subarray power pattern simulation (in a logarithmic scale) scanned to 30°; and (d) A stack of multiple beam power patterns (in a linear scale) are simulated for a subarray digital array and scanned to 30° showing the dependence on the subarray factor.

beam, inevitably this next beam had an azimuth offset from the first beam. This was due to the dependence of the array factor on the subarray pattern. Fig 2.11 (c) shows the subarray power pattern simulation (in a logarithmic scale) scanned to 30° and the beam feathering is visible. In Fig 2.11 (d) a stack of multiple beam power patterns (in a linear scale) are simulated and scanned to 30°, and the dependence on the subarray factor (Fig 2.11 (c)) is visible. The beam dwell time on a target is considerably more than that of a passive system, however the energy is distributed throughout the elevation of interest. Some examples of subarray digital arrays used on naval ships are the receive channel of the SAAB Sea Giraffe AMB (Fig 2.12 (a)) [11] and the Hensholdt TRS-4D (Fig 2.12 (b)) [12].

(a) (b)

Fig. 2.12. Pictures of the (a) SAAB Sea Giraffe AMB and (b) Hensholdt TRS-4D and [7].

Element digital arrays

Element digital arrays have a transceiver with digitisation at each element. Beamforming is simplified and flexible. Phase and amplitude weights are applied by digital operations and beamforming is performed by digital summations across the array. It is possible to reconfigure the overall beam shape by digitally adjusting excitation coefficients at element level, limited only by the element pattern. A major benefit of digital arrays is the ability to provide multiple, simultaneous and independently steered receive beams. For an element-level digital array, the individual beams can be independently scanned anywhere within the array scan volume. The number of simultaneous receive beams is limited by the data rate capability, processing power and element pattern [6]. This capability gives rise to the term “dual axis multi-beam”, which implies full control of multiple receive beams in both azimuth and elevation directions [2]. Of importance to consider is the loss in transmit gain if wide volumes are covered simultaneously.

Receive calibration of an element-level digital array is generally simplified relative to an analog array.

For angle estimation, element digital array radars typically can perform monopulse techniques along the azimuth and elevation axis where the digital beams are formed without the need of separate hardware manifolds for the sum and difference channels. Other more accurate angle estimation techniques can also be used, for example MLE [6].

An example of an element digital array antenna system can consist of T/R modules (without hardware phase shifters) at element level. The element signals are digitised for digital phase shifting and array summation. The example array is illustrated in Fig 2.13. Comparing this type of beamforming with equation 2.2 the array factor was written as:

$$E_{ai}(az, el) = \sum_{m=-M}^{M} \sum_{n=-N}^{N} |A_{mn}| e^{\frac{j2\pi}{\lambda}[md_y(\cos(el)\sin(az) - \cos(el_{si})\sin(az_{si})) + nd_z(\sin(el) - \sin(el_{si}))]} \tag{2.6}$$

In equation 2.6, subscript $i \in [1, p]$ denoted the beams that are digitally formed and p denoted the number of beams. Fig 2.14 (a) is an element digital array receive power pattern simulation (in a linear scale) of multiple beams. This illustrates how this type of rotating phased array antenna and beam could work on a ship as a surveillance radar. While the antenna rotates, the surveillance volume is searched with multiple simultaneous azimuth and elevation beams digitally formed. Fig 2.14 (b) is the array transmit power pattern simulation (in a logarithmic scale), formed through particular adjustment of the excitation coefficients, which covers the complete azimuth and elevation volume of interest in Fig 2.14 (a). Fig 2.14 (c) shows a possible element digital receive power pattern simulation (in a linear scale) of multiple beams in azimuth to search the surface. Fig 2.14 (d) is the associated transmit power pattern (in a logarithmic scale). The beam dwell time on a target is more than that of a passive or digital subarray system, however the energy is distributed throughout the volume of interest. An example of an element digital array used on naval ships is the Thales NS100 [2].

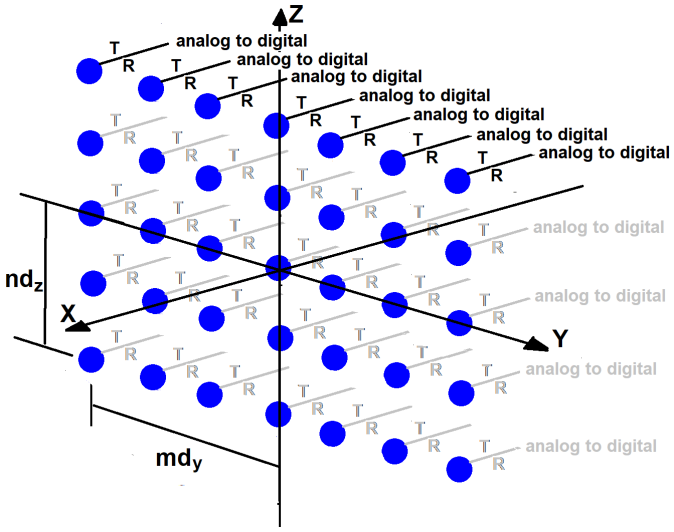

Fig. 2.13. Element digital array with T/R modules (excluding phase shifters) and digitisation at element level.

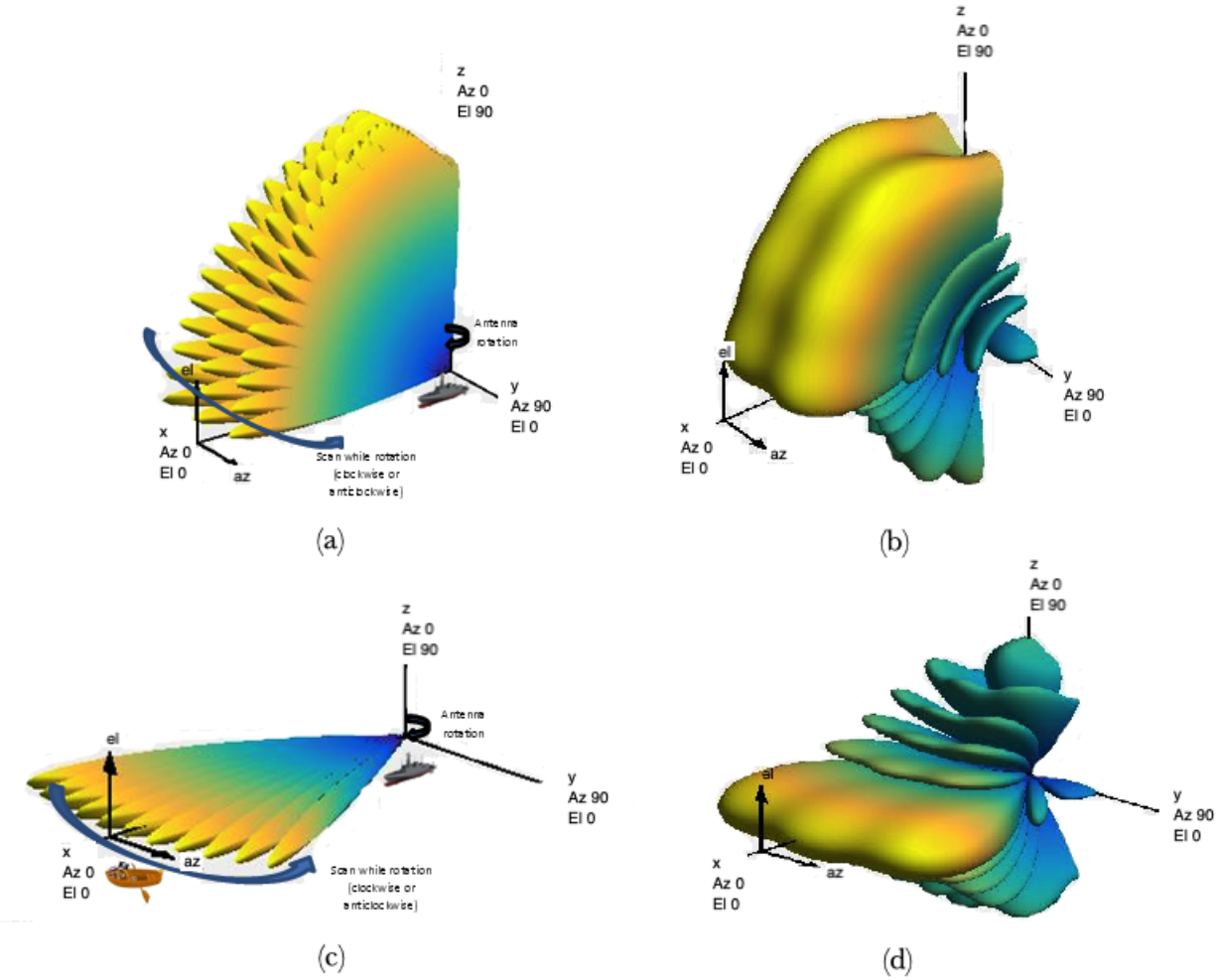

Fig. 2.14. Element digital array beamforming and scan pattern simulations: (a) element digital array receive power pattern simulation (in a linear scale) for a rotating ship surveillance radar; (b) the associated array transmit power pattern simulation (in a logarithmic scale); (c) element digital receive power pattern simulation (in a linear scale) for surface surveillance; and (d) the associated array transmit power pattern (in a logarithmic scale).

2.3 Sea clutter

The effect of sea clutter is normally most prevalent in low elevation beams formed by a digital multibeam array surveillance radar. To remove false detections of sea clutter when searching for high end fast-moving targets, a naval surveillance radar system normally suppresses the clutter through Doppler filtering. In this case, the effect of the sea surface is limited to influencing the radar blind speed spectrum and mutlipath interference. However, when searching for slow targets, the sea clutter cannot be suppressed as this will inevitably also reduce the target of interest's echo. It is therefore important to understand and incorporate the principles of sea clutter into the simulation model.

The simulation model used in this study made use of real clutter data. The clutter data sets were from the X-band CSIR Fynmeet Sea Clutter Measurement Trial [13]. It was adapted and inserted into the return signal across the radar's instrumented range for the low elevation beams. Several features can be used to characterise these sea clutter returns. The following significant characteristics for this study and simulation model are discussed:

- the clutter area reflectivity (σ^0), which determines the clutter RCS and clutter mean power return; and
- the distribution of the clutter amplitudes or power.

2.3.1 Clutter area reflectivity and average power

Clutter area reflectivity

The model that was used to describe σ^0 was the GIT model. This model covers radar frequencies from 1 to 100 GHz and is based on an underlying multipath model as well as other more general trends observed in experimental data sets. It is valid over grazing angles in the region 0.1° to 10° [14].

A standard estimate of wave height is the Douglas sea state, which is shown in Table 2.1 [14]. The wave height, $h_{1/3}$, is the significant wave height, defined as the average peak-to-trough height of the highest one third of the waves. In Table 2.1, the stated wind speed produces the stated wave height.

If the sea state, (s) is available, the wind velocity (in m/s) can be determined using [14]:

$$U = 3.16s^{0.8} \tag{2.7}$$

The average wave height (in m), is given by [14]:

$$h_{av} = 0.00452U^{2.5} \tag{2.8}$$

Table 2.1. The Douglas sea state table.

Douglas sea state	Description	Wave height, $h_{1/3}$, (ft)	Wind speed (kn)
1	Smooth	0 - 1	0 - 6
2	Slight	1 - 3	6 - 12
3	Moderate	3 - 5	12 - 15
4	Rough	5 - 8	15 - 20
5	Very Rough	8 - 12	20 - 25
6	High	12 - 20	25 - 30
7	Very high	20 - 40	30 - 50

A roughness parameter is defined as [14]:

$$\sigma_\phi = (14.4\lambda + 5.5)\frac{\phi_{gr} h_{av}}{\lambda} \tag{2.9}$$

where λ is the RF wavelength (in m) and ϕ_{gr} is the grazing angle (in *radians*). The multipath interference parameter can then be calculated as [14]:

$$A_i = \frac{\sigma_\phi^4}{1 + \sigma_\phi^4} \tag{2.10}$$

The wind direction dependence is given by [14]:

$$A_u = e^{0.2\cos\theta_w(1-2.8\phi_{gr})(\lambda+0.015)^{-0.4}} \tag{2.11}$$

where θ_w (in *radians*), is the wind direction relative to the radar look direction. The variation on the sea state is contained in the factor [14]:

$$A_w = \left(\frac{1.94U}{1 + \frac{U}{15.4}}\right)^{\frac{1.1}{(\lambda+0.0015)^{0.4}}} \tag{2.12}$$

The clutter area reflectivity σ^0 (in dB m^2/m^2) for both polarisations (cross polarisation excluded) are as follow [14]:

$$\sigma^0_{HH} = 10\log(\lambda\phi_{gr}^{0.4} A_i A_u A_w) - 54.09 \tag{2.13}$$

$$\sigma^0_{VV} = \sigma^0_{HH} - 1.05\ln(h_{av} + 0.015) + 1.09\ln(\lambda) + 1.27ln(\phi_{gr} + 0.0001) + 9.7 \tag{2.14}$$

Clutter average power

It can be shown that once the clutter area reflectivity has been calculated, the clutter RCS (in m^2) can be calculated using [14]:

$$\sigma_c = \sigma^0 A_c \tag{2.15}$$

where A_c (in m^2) is the pulse clutter illuminated area and σ^0 is in linear units (m^2/m^2). Fig 2.15 illustrates the method for determining the illuminated area. In the figure, B_{el} and B_{az} are the elevation, ϕ_{gr} is the grazing angle (in *radians*) and azimuth beamwidths respectively (in *radians*). R (in m) is the range from the radar to the illuminated area (normally the middle of the area) and h is the height of the radar. The term $\frac{cT}{2}$ is the range resolution of the radar for an uncompressed pulse where c is the RF wave propagation speed (3×10^8 m/s) and T is the pulse width (in s). If the area illuminated by the pulse is approximated to be rectangular, the illuminated area can be calculated as [14]:

$$A_c = \frac{cT}{2} R B_{az} \sec(\phi_{gr}) \tag{2.16}$$

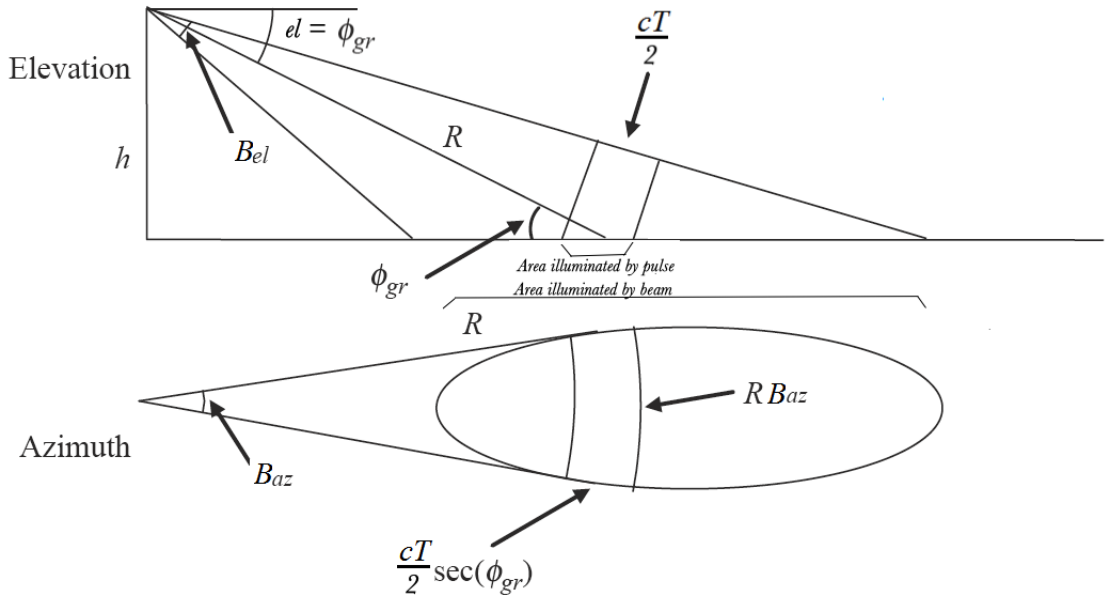

Fig. 2.15. Clutter illuminated area [14].

The average clutter power can now be calculated using the radar range equation [14]:

$$P_c = \frac{P_t G^2 \lambda^2 \sigma_c}{(4\pi)^3 R^4} \tag{2.17}$$

where P_c (in W) is the clutter average power, P_t (in W) is the transmit power and G is the gain of the radar antenna.

2.3.2 Clutter amplitude distribution

The K-distribution for clutter amplitude has been developed by the observation of real clutter data over a wide range of conditions and can be modelled mainly by two components: the

local power and the speckle component. The slow varying large scale structure of the sea mean power level of the clutter is modelled as a gamma process. Clutter speckle is a fast time and space varying component in the sea surface. This can be modelled in the K-distribution as an exponential process. The K-distribution probability density function (PDF) of the clutter envelope is given by [14]:

$$P(E) = \frac{4b^{(v+1)/2}E^v}{\Gamma(v)} K_{v-1}(2E\sqrt{b}) \tag{2.18}$$

where $E = |y|$ is the envelope of the clutter signal y, $K_{v-1}(2E\sqrt{b})$ is the modified Bessel function of the second kind, $\Gamma(v)$ is the Gamma function, b is the scale parameter and v is the shape parameter. It can be shown that the shape parameter depends on the grazing angle, illuminated area, polarisation and swell aspect angle. The relation between the shape and scale parameter is expressed as the mean value of the n-th moment of the envelope [14]:

$$\mathbf{E}(E^n) = b^{-n/2}\frac{\Gamma(1+n/2)\Gamma(v+n/2)}{\Gamma(v)} \tag{2.19}$$

Plots of the K-distribution PDF are shown in Fig 2.16 for various values of the shape parameter, v, equal to the scale parameter, b. When $v = \infty$ it reduces to the Rayleigh distribution, and when v gets smaller ($0 < v < 1$), it corresponds to spiky clutter [14].

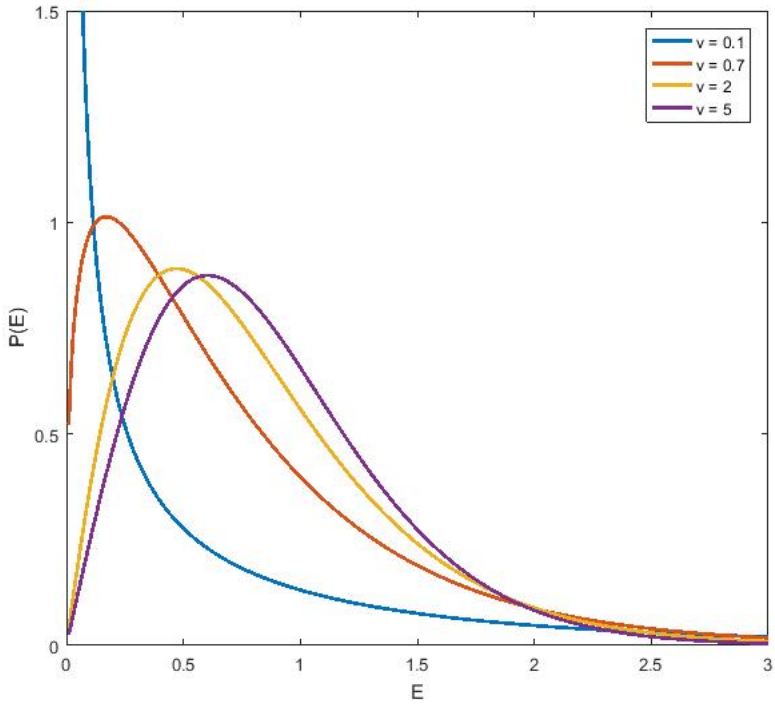

Fig. 2.16. K-distribution PDF for various values of the shape parameter.

The K-distribution model has no dependence on wind speed or sea state. Data for the model was collected with pulse-to-pulse frequency agility at radar frequencies from 9 to 10 GHz, range resolution of $4.2\,m$, grazing angles of 0.1° to 10° and vertical polarisation [15]. The radar parameters used from the Fynmeet trials in this study was for fixed frequency at 9 GHz, range resolution of $15\,m$, grazing angles between 0.314° to 1.27° and vertical polarisation.

In practice, for fixed frequency operation, the speckle component will decorrelate over a period of 5 to $10\,ms$ due to the inherent motion of the clutter scatterers [14]. A radar system can capitalise on this decorrelation to detect a slow-moving target in sea clutter if a longer observation time is used. However, the slow varying large scale structure of the sea will decorrelate over longer periods in the order of seconds.

It should also be mentioned that there are discrete spikes in sea clutter, which could be included in the K-distribution, with a modified version called the KA-distribution [14]. These spikes have an exponential distribution, and only decorrelate over a time period in the order of seconds. The KA-distribution was not used in this study however, these spikes could have been present in the real clutter data used. Furthermore, antenna rotation scanning will introduce some decorrelation of the clutter. The direct effect of rotation scanning on clutter decorrelation was not be tested in the model created in this study as the real clutter data used is from a non-rotating antenna.

2.4 Beam pattern synthesis

It is not always desirable to use the standard minimum beamwidth pattern of the phased array antenna. Sometimes it could be required to synthesise low sidelobes or nulls in the direction of interference signals. In other cases it might be required to change the pattern of the main beam pattern. The particular case of changing the pattern of the main beam pattern is called beam shaping [16]. Beam shaping is useful when a single transmit beam is required to cover the entire search volume of interest, where multiple standard minimum beamwidth patterns will be formed on receive.

Useful methods for beam shaping of linear arrays are the Fourier transform and the Woodward-Lawson methods. For best performance of beam shaping in planar arrays iterative optimisation techniques should be used [17]. However, for the sake of simplicity and the purpose of this study, the Fourier transform method was used on a subarray and array level for the beam shaping of the transmit beam. The simulation model, created in this study, had the advantage that the transmit and receive signals of the antenna have an independent input of the target aspect angle. This provided the opportunity to use a boresight-only transmit beam, even if azimuth scanning of the beam was required. A pseudo scanning of the boresight transmit beam was introduced by rotating the target around the antenna. This was similar to the method used to introduce the pseudo rotation of the antenna.

For the purpose of the Fourier transform method, the array factor was limited to the two-dimensional (2D) zx-plane. This implied that the azimuth angle was zero. If the linear array elements were arranged along the z-axis and the steering angles (el_s and az_s) were zero, the element weights for an uneven number of elements ($2N+1$) were given as [16]:

$$a_n = \frac{1}{2\pi}\int_{-\pi}^{\pi} E_a(el)e^{-j\frac{2\pi}{\lambda}nd_z\sin(el)}\frac{2\pi}{\lambda}d_z\cos(el)d_{el} \tag{2.20}$$

where $-N \leq n \leq N$. The formula could be adapted for an even number of elements ($2N$) in the z-axis direction. It could also be adapted and applied in the y-axis direction. The amplitudes were normalised with the maximum element weight in this study. Fig 2.17 (a) and (b) were simulations of the shaped 3D beam pattern (in a logarithmic scale) formed for a linear array of 11 and 41 elements in the y-axis direction using the Fourier transform method. The azimuth pattern was designed to be $-20°$ to $20°$. It was seen that more elements result in a better approximation of the intended shaped beam. This is similar to the use of the Fourier transform for frequency spectrum representation of a signal, whereby more harmonics will provide a better approximation of the complete signal. Fig 2.17 (c) and (d) were the shaped 3D beam patterns formed for a linear array of 11 and 41 elements in the z-axis direction. The elevation pattern was designed to be $0°$ to $70°$.

The weights of these two linear arrays were used to formulate the weights required to shape a beam for a planar array. It was the product of these two linear array patterns. Each horizontal linear array in the y-axis direction of the planar array received the calculated weights of the horizontal (y-axis) linear array. The calculated weights of the vertical linear array (z-axis) elements (which in number should be the same as the number of horizontal arrays), were multiplied with the corresponding horizontal linear array. This process was described as the matrix multiplication:

$$\mathbf{W}_a = \mathbf{W}_v\mathbf{W}_h \tag{2.21}$$

where $\mathbf{W}_v$ was a $p \times 1$ matrix where p was the number of elements ($2N+1$ if odd and $2N$ if even) in the vertical linear array and $\mathbf{W}_h$ was a $1 \times q$ matrix where q was the number of elements ($2N+1$ if odd and $2N$ if even) in the horizontal linear array. $\mathbf{W}_a$ was a $p \times q$ matrix, which represented the element weights of the planar array. Fig 2.17 (e) and (f) wer simulations of the final shaped array beam pattern (in a logarithmic scale).

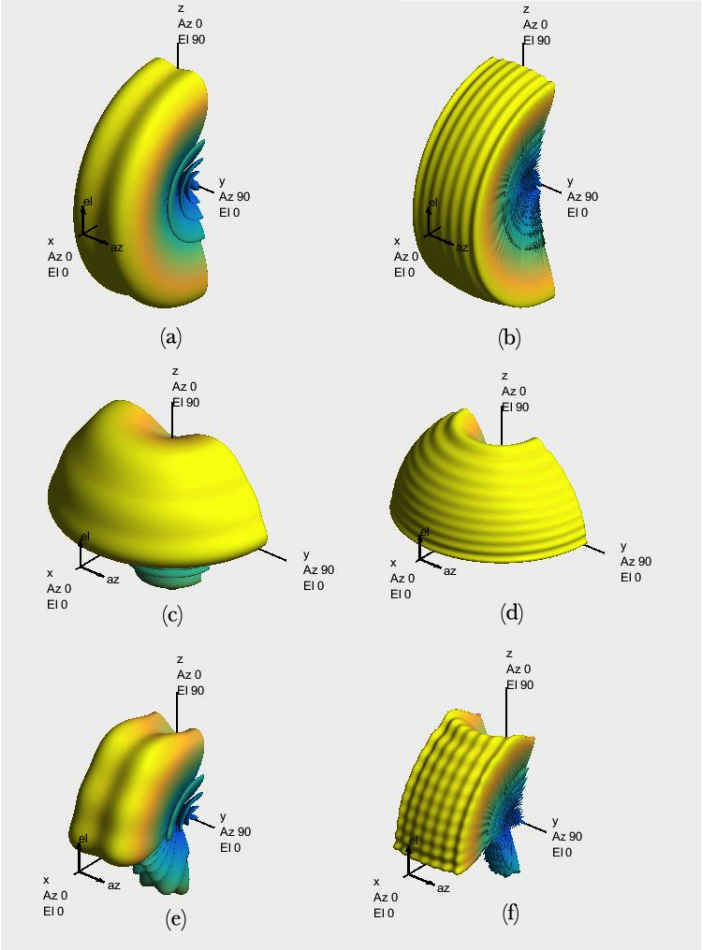

Fig. 2.17. Array beam shapes (in a logarithmic scale) synthesised using the Fourier transform for: (a) a linear array of 11 elements in the y-axis direction (azimuth coverage: -20° to 20°); (b) a linear array of 41 elements in the y-axis direction (azimuth coverage: -20° to 20°); (c) a linear array of 11 elements in the z-axis direction (elevation coverage: 0° to 70°); (d) a linear array of 41 elements in the z-axis direction (elevation coverage: 0° to 70°); (e) a planar array of 11×11 elements, which is the product of the beams in (a) and (c); and (f) a planar array of 41×41 elements, which is the product of the beams in (b) and (d).

2.5 CFAR detection

The problem in reliable target detection by the radar signal processing is that of discriminating a target return from the sea clutter returns and thermal noise. Certain features in the radar returns help us to discriminate between real and spurious target returns. The final discrimination is usually done on the basis of amplitude at a detection threshold and the threshold quantity depends on the chosen features and the signal processing scheme. Typical

signal processing schemes with associated features include the following [14]:

- *Pulse-to-pulse integration.* Pulse-to-pulse integration exploits differences in amplitude statistics and pulse-to-pulse correlation between targets and clutter or noise. Decorrelation of thermal noise happens on a very short time basis in orders less than that of the PRI. Furthermore, signal-to-noise ratio (SNR) gain will also increase with more transmit power in the presence of thermal noise. Sea clutter however will only decorrelate partially after 5 to 10 ms (for the speckle component), which can possibly be capitalised on for longer dwell times. SCR will not increase with more transmit power.
- *Scan-to-scan integration.* Scan-to-scan integration is often used to exploit the longer term correlation characteristics of targets and clutter. In particular, discrete clutter spikes may not be affected by pulse-to-pulse integration, and appear to be target-like. However, such spikes usually only persist over periods in the order of a second or so, specifically the slow varying large scale structure of the sea mean power level and discrete spikes. Longer term integration, from scan-to-scan over several seconds, can be used to distinguish them from real targets. Scan-to-scan integration was not evaluated in the simulation model.
- *Polarisation.* Polarisation can be used to increase the SCR. It will not be an input variable in this simulation.
- *Doppler processing.* The Doppler shifts of moving targets relative to the sea clutter plays an important role in this study and are widely used in naval surveillance radar systems to discriminate targets from sea clutter. Doppler processing is useful and relatively simple to discriminate fast-moving targets through clutter suppression. However, it can become challenging for slow-moving targets in a low elevation beam affected by sea clutter.

A desirable property of a detector is the ability to maintain a given probability of false alarm (P_{fa}) in the presence of interference. A detector that fulfils this purpose is called a CFAR detector. The CFAR detector estimates the interference (noise and clutter) power and adjusts the detector threshold to maintain a fixed P_{fa}. The basic architecture of a CA-CFAR detector is illustrated in Fig 2.18. Each cell in the 2D data set, which includes the range and Doppler spectrum data, for a specific beam is tested. The cell under test (CUT) is located in the center of the CFAR window. The guard cells, denoted as 'G', are not used to estimate the interference power. The reference cells, denoted as 'R', are used to estimate the interference power [18].

The CFAR detector threshold is expressed as the product of the CFAR constant α and the interference power estimator $\hat{g}$ [18]:

$$T = \alpha \hat{g} \tag{2.22}$$

The estimate for the interference power for a CA-CFAR detector cell at position (i, l) of the

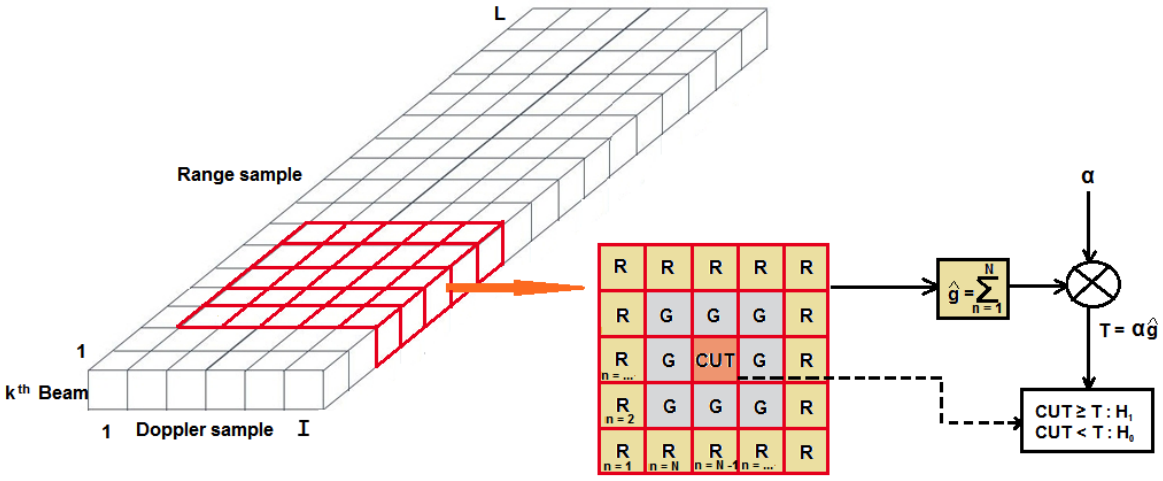

Fig. 2.18. The CA-CFAR detector with a 2D window.

2D data set can be written as [18]:

$$\hat{g}_{CA} = \frac{1}{N}\sum_{n=1}^{N}|y_n|^2 \tag{2.23}$$

where N is the number of cells in the reference window, n is the n-th cell in the reference window and $|y_n|^2$ is the square law output of the signal at the n-th reference cell. The CA-CFAR constant is [18]:

$$\alpha_{CA} = N[P_{fa_{CA}}^{-1/N} - 1] \tag{2.24}$$

where $P_{fa_{CA}}$ is the average probability of false alarm, which is independent of the interference power. CA-CFAR performance can degrade significantly in the presence of interference targets and clutter boundaries. Fig 2.19 is a simulated 2D data set power return with a CA-CFAR threshold. The target return is larger than the threshold, but there are also false returns along the edges where clutter is suppressed.

A solution, as was used in the simulation model in this study, to reduce clutter edge false alarms is the use of the greatest-of CA-CFAR (GOCA-CFAR) [18]. The interference power estimate is computed separately in a leading and lagging window as shown in Fig 2.20.

The larger of the two power estimates in the reference windows is used as the sample mean. It can be expressed as [18]:

$$\hat{g}_{GO} = max(\hat{f}_{GO,lag}, \hat{f}_{GO,lead}) \tag{2.25}$$

where

$$\hat{f}_{GO,lag} = \frac{2}{N}\sum_{n=1}^{N/2}|y_n|^2 \tag{2.26}$$

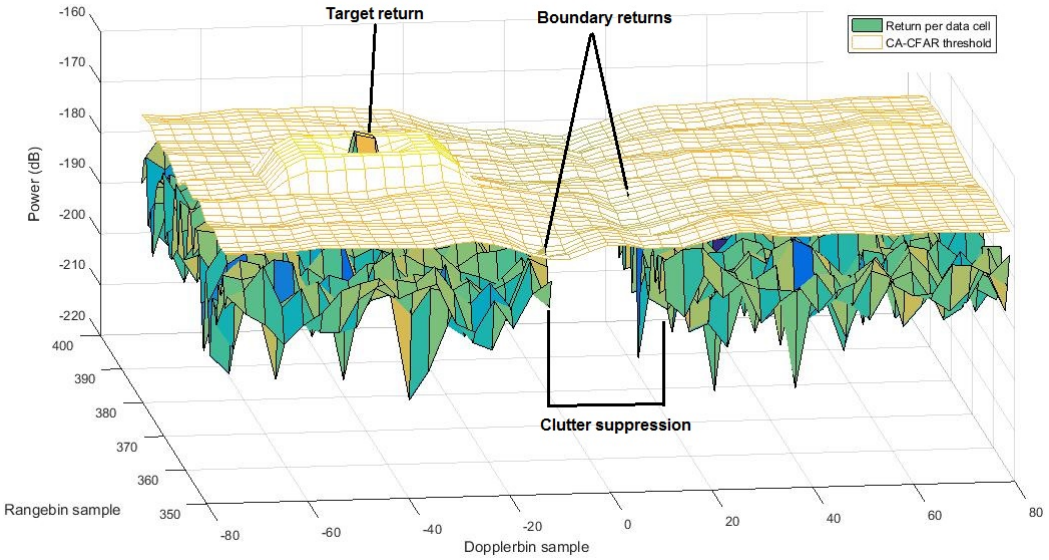

Fig. 2.19. A simulated 2D data set power return with a CA-CFAR threshold. The target return is larger than the threshold, but there are also false returns along the edges where clutter is suppressed.

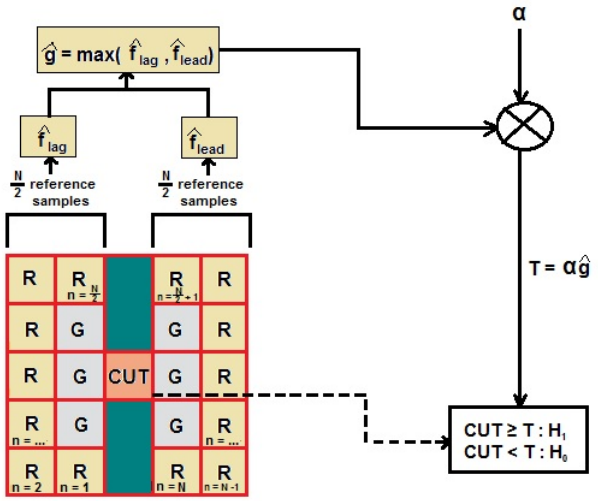

Fig. 2.20. The GOCA-CFAR detector with a 2D leading and lagging reference window.

and

$$\hat{f}_{GO,lead} = \frac{2}{N} \sum_{n=\frac{N}{2}+1}^{N} |y_n|^2 \tag{2.27}$$

Solving the GOCA-CFAR constant (α_{GO}) is more difficult than the CA-CFAR. It involves an

iterative process using the complex relationship with the GOCA-CFAR average probability of false alarm in a homogeneous interference environment as follow [18]:

$$P_{fa_{GO}} = 2\left[\left(1+\frac{2\alpha_{GO}}{N}\right)^{-N/2} - \left(2+\frac{2\alpha_{GO}}{N}\right)^{-N/2}\sum_{k=0}^{\frac{N}{2}-1}\binom{\frac{N}{2}-1+k}{k}\left(2+\frac{2\alpha_{GO}}{N}\right)^{-k}\right] \quad (2.28)$$

The average probability of detection associated with GOCA-CFAR in a homogeneous interference environment is defined as [18]:

$$P_{d_{GO}} = 2\left[\left(1+\frac{2\alpha_{GO}}{N(1+SINR)}\right)^{-N/2} - \left(2+\frac{2\alpha_{GO}}{N(1+SINR)}\right)^{-N/2}\sum_{k=0}^{\frac{N}{2}-1}\binom{\frac{N}{2}-1+k}{k}\left(2+\frac{2\alpha_{GO}}{N(1+SINR)}\right)^{-k}\right] \quad (2.29)$$

where SINR is the Signal-to-Interference-plus-Noise Ratio.

Fig 2.21 is a simulated 2D data set power return with a GOCA-CFAR threshold with similar noise and target power returns as in Fig 2.19. There are no false boundary returns around the clutter suppression area.

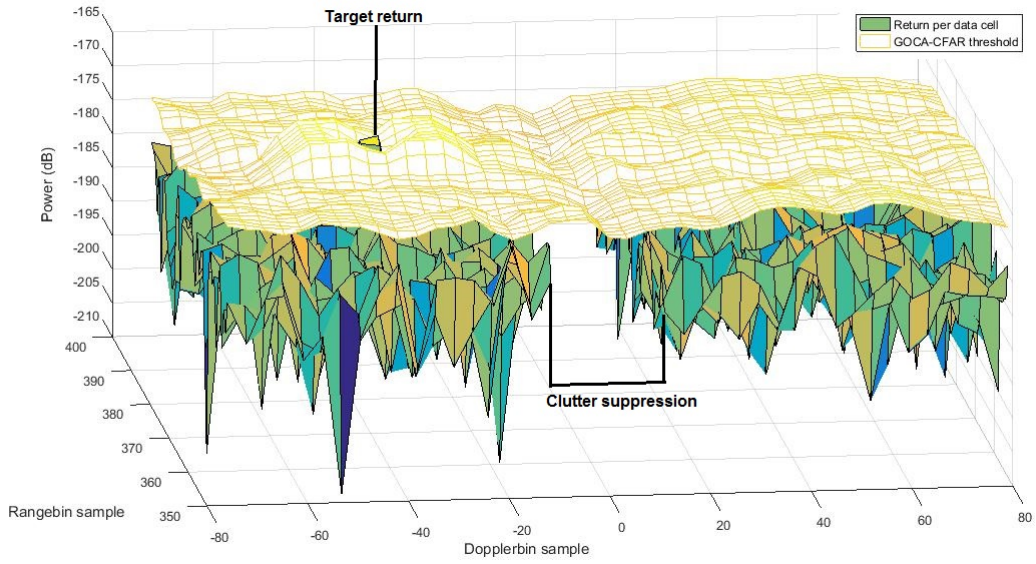

Fig. 2.21. A simulated 2D data set power return with a GOCA-CFAR threshold. The target return is larger than the threshold, with no false returns round the clutter suppression boundary.

2.6 PRF and ambiguity resolution

Pulse-Doppler radar operation can be divided into three regimes according to ambiguity characteristics [18]:

- *Low PRF.* If the PRF is sufficiently low for the range to be unambiguous and the velocity to be ambiguous, the radar is considered to be in low PRF mode. This implies that returns will be limited to the maximum range (in m) determined by:

$$R_{ua} = \frac{c}{2PRF} \tag{2.30}$$

  and the maximum velocity in m/s of the spectrum determined by

$$v_{max} \in \Big[-\frac{\lambda PRF}{4} - \frac{n\lambda PRF}{2}, \frac{\lambda PRF}{4} + \frac{n\lambda PRF}{2} \Big) \tag{2.31}$$

  where n represents unambiguous velocity spectrum multiples required to cover the velocity spectrum of interest. Low PRF mode allows for simple processing as ambiguity resolution is only required in the velocity domain. There are no consecutive pulse return overlaps. This makes it ideal for slow target processing as it avoids the addition of clutter and clutter sidelobe returns from several pulse overlaps. This will maintain an optimal SCR for targets in the clutter spectrum. However, it produces a highly ambiguous velocity spectrum of which a large proportion is affected by clutter, clutter sidelobe pollution and blind zones [19]. The lack of proper clutter-free zones makes this mode not ideal for fast target detection.

- *Medium PRF.* If both the range and velocity are ambiguous the radar is considered to be in medium PRF mode. This implies that target returns will be limited to the maximum range (in m) determined by:

$$R_{max} = \frac{nc}{2PRF} \tag{2.32}$$

  where n represents unambiguous range multiples required to cover the range of interest. The maximum velocity is determined by equation 2.31. Medium PRF mode allows good detection over the range and velocity spectrum. It is the preferred mode for detection of higher velocity targets. A considerable proportion of the velocity spectrum is free of clutter and clutter sidelobe pollution and blind zones for detecting targets moving at velocities beyond the clutter spectrum. The probability of target masking due to eclipsing (radar transmission blind zones) is also insignificant however, it requires a complex range and velocity ambiguity resolution process [19]. Pulse return overlaps will add clutter and clutter sidelobe returns. This reduces the SCR for slow targets in the clutter returns, making it impractical for detection of this type of target.

- *High PRF.* In high PRF mode the range is ambiguous and the velocity unambiguous. This implies that returns will be limited to the maximum range as given in equation 2.32

and the velocity spectrum in m/s by

$$v_{ua} \in \Big[-\frac{\lambda PRF}{4}, \frac{\lambda PRF}{4} \Big) \tag{2.33}$$

High PRF mode allows for relatively simple processing as ambiguity resolution is only required in the range domain. However, it produces a highly ambiguous range. Many overlaps of the pulse returns cause a large addition in clutter and clutter sidelobes. This can severely pollute and extend blind zones in the velocity spectrum degrading slow and fast target detection. With the limited unambiguous range almost the entire range and velocity data window can eventually become completely polluted. Eclipsing can also play a significant role due to the proportion to the limited unambiguous range [19].

The frequency range for low PRF operation is given in X-band ($\lambda = 0.0\overline{3}\,m$) as less than $6\,kHz$, for medium PRF as more than $6kHz$ and less than $24\,kHz$ and for high PRF as more than $24\,kHz$ [19]. The radar model developed in this study, allocated resources to air and surface channels. For the surface channel the resources, including the PRF, were optimised for detection of slow surface or slow low flying targets that will be affected by sea clutter. Therefore a completely unambiguous low PRF waveform was used for this channel. For the air channel the resources, including the PRF, were optimised for detection of fast targets at a wide range of possible elevation angles. An ambiguous range and velocity medium PRF waveform were therefore be used for this channel.

A 2D coincidence algorithm was used to resolve target returns beyond the unambiguous range or velocity for the medium PRF mode [18]. It made use of different PRF rates for each CPI. For each CPI with its associated PRF a 2D data set is obtained as illustrated in Fig 2.22. As can be seen in Fig 2.22, the data set has clutter and eclipsing blind zones. There are also apparent target return positions for a single target. Because the target, in this case, is beyond the unambiguous range and Doppler velocity, the 2D bin position is different for each PRF. In order to determine the true range and Doppler velocity data point, the 2D data sets in Fig 2.22 can be replicated n-times to the required range and Doppler velocity bins. The algorithm then searches for the 2D data point that exhibits detections in all the replicated PRF data sets. This is illustrated in Fig 2.23. As shown in Fig 2.23, the point that exhibits detections in all three data sets is the point at Doppler bin 10 and range bin 13. This represents the true range and Doppler velocity of the target detection.

In general, N PRFs are required to disambiguate $N-1$ targets, to avoid ghost returns. It is also important to consider that the true return could be hidden in a blind zone. In this study, the PRF shift will be selected such that it will guarantee the target shift out of the clutter blind zone for consecutive PRFs. An m-of-n detector will be used with the coincidence algorithm, where $n = N$ and $m \leq N$. For a single target, it is then also important to adjust to a minimum of three PRFs.

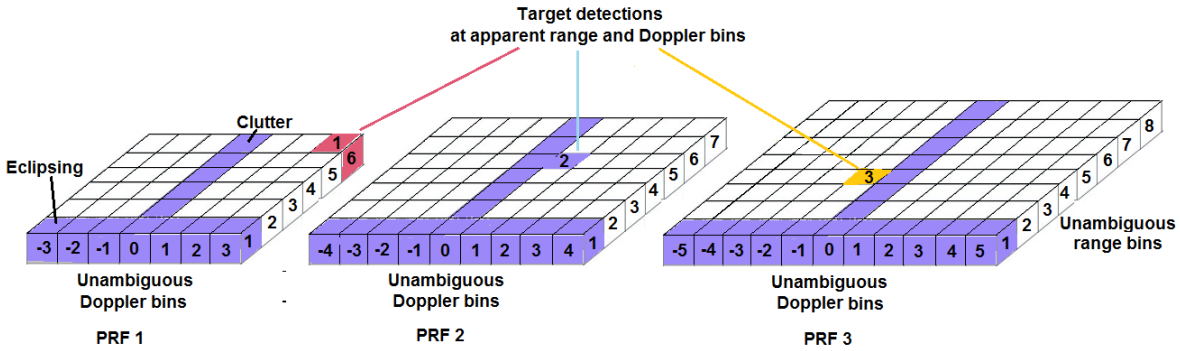

Fig. 2.22. Different unambiguous PRF 2D data sets with the same target's apparent returns. Also illustrated are the clutter and eclipsing blind zones.

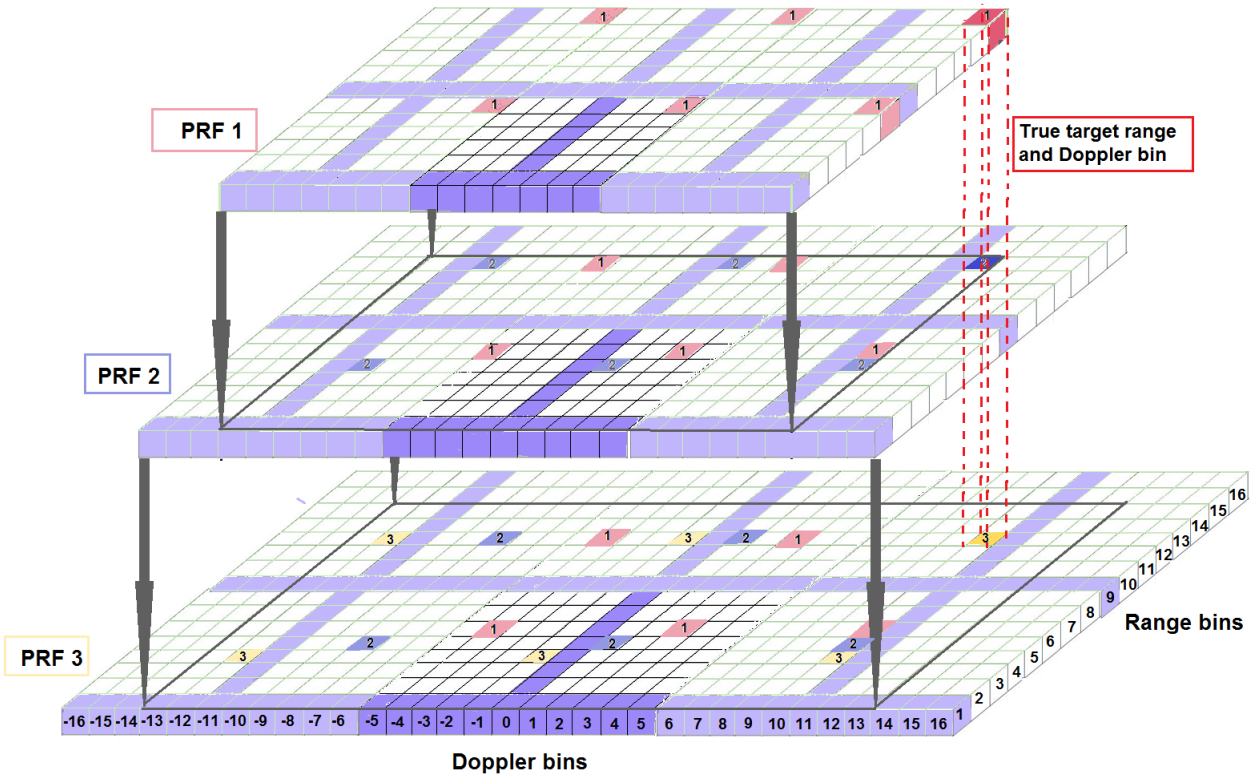

Fig. 2.23. The 2D coincidence algorithm to reslove ambiguous target returns. The point at Doppler bin 10 and range bin 13 represents the true range and Doppler velocity of the target detection.

2.7 Summary

This chapter discussed some of the most important theoretical concepts that were used in the simulation model developed for this study. The equations discussed here were all used in the design and discussion of the results.

Phased array technologies, architectures and some performance attributes of different phased array systems were discussed. These attributes played a role in comparing the detection performances of different beamforming and scan patterns. A summary of the performances attributes of different array architectures discussed in this subsection is outlined in Table 2.2 [6].

Table 2.2. Summary of array architecture performance comparison.

Attribute	Analog (passive or active)	Subarray digital	Element digital
Beam shape flexibility	Fixed	Partially adjustable at subarray level	Fully adjustable
Multiple simultaneous receive beams	Very few, limited by hardware	Multiple beams limited to subarray pattern	Multiple beams limited to element pattern
Angle accuracy	Hardware monopulse channels or centroiding	Digital monopulse or MLE along single axis	Digital monopulse or MLE along dual axis

Real sea clutter data was adapted and used in the radar model. Important characteristics that were modified include the clutter area reflectivity described by the GIT model and the illuminated area, which produces the clutter RCS. The RCS was used to produce the clutter power as a function of range. The K-distribution PDF was the statistical model of choice to analyse the clutter envelope. The direct effect of scanning on clutter decorrelation was not tested.

Beam shaping was used to produce a single transmit beam that is required to cover the entire search volume of interest. For the sake of simplicity and the purpose of this study, the linear array Fourier transform method was used. The planar array boresight transmit weights and resultant beam was shaped through the product of horizontal and vertical linear array patterns. A pseudo scanning of the boresight transmit beam was introduced by rotating the target around the antenna if the beam was required to move off boresight.

Pulse-to-pulse integration and Doppler processing were features used in the simulation model to help distinguish targets from noise and clutter by means of CFAR detection. The desirable property of the CFAR detector is the ability to maintain the P_{fa} in the presence of interference.

The CFAR detector of choice for coherent processing in this study was the GOCA-CFAR due to its ability to reduce clutter edge false alarms in the 2D range-Doppler data set.

For detection of slow surface or low flying targets that are affected by sea clutter, a low PRF waveform was used. This was done to avoid addition of clutter returns. For detection of fast targets at a wide range of possible elevation angles a medium PRF waveform was used. This allowed a considerable proportion of the velocity spectrum to be free of clutter pollution and blind zones for detecting targets moving at velocities beyond the clutter spectrum. Eclipsing zones were also insignificant. A 2D coincidence algorithm was used to resolve target returns beyond the unambiguous range and velocity for the medium PRF waveform.

Chapter 3

Simulation Design

The following chapter focused on the design of the radar simulation model. MATLAB was used as the simulation platform. In particular, the Phased Array Toolbox contributed a considerable number of algorithms to the system design. The chapter discussed the user inputs, simulation model configuration, processing and the outputs. A complete description of all the building blocks of this model was not possible in this dissertation, however a thorough overview with some in-depth insight was provided.

3.1 Inputs

This section briefly described the inputs (independent variables and constants) that can be entered into the simulation model. Inputs were entered through matrix and vector sets. The matrices and vectors were not be discussed in this study. The initial preparation of the inputs for further processing were provided.

Of significance was the ability to define processing sectors (rotation sector divisions) within a specified rotation sector. In these processing sectors variables could be set. Each processing sector could for example, for the air and surface channels, have its own CPI size, non-coherent processing interval (NCPI) size - surface only, PRF(s), transmit beam shape, receive beam stacks and antenna relative scan rate. CPIs were used for Doppler processing in the air or surface channel. NCPIs could typically be used, interleaved with the CPIs, for surface channel only where low PRFs were used to avoid clutter return overlaps. In this case there normally would not be enough pulses available for Doppler processing.

Fig 3.1 shows the concept of the defined processing sectors in a 180° rotation sector. Each processing sector had its own interleaved air and surface channel with unique parameters. It was selected arbitrarily in this case. A sector of 120° was for example defined that included air and interleaved surface channel processing. The beam would have to be electronically scanned

horizontally, while the antenna rotates, to cover the full 180° in a rotation in order to enable fast target air channel detection on every antenna rotation. In this sector, the interleaved surface channel would typically be short low PRF NCPI bursts only. While a sector of 60° was selected exclusively for surface channel processing, allowing multiple horizontal beams for long dwell time CPI bursts and high Doppler resolution. The 60° sector offset could be changed on every rotation to cover the full 180° of surface scanning after 3 antenna rotations.

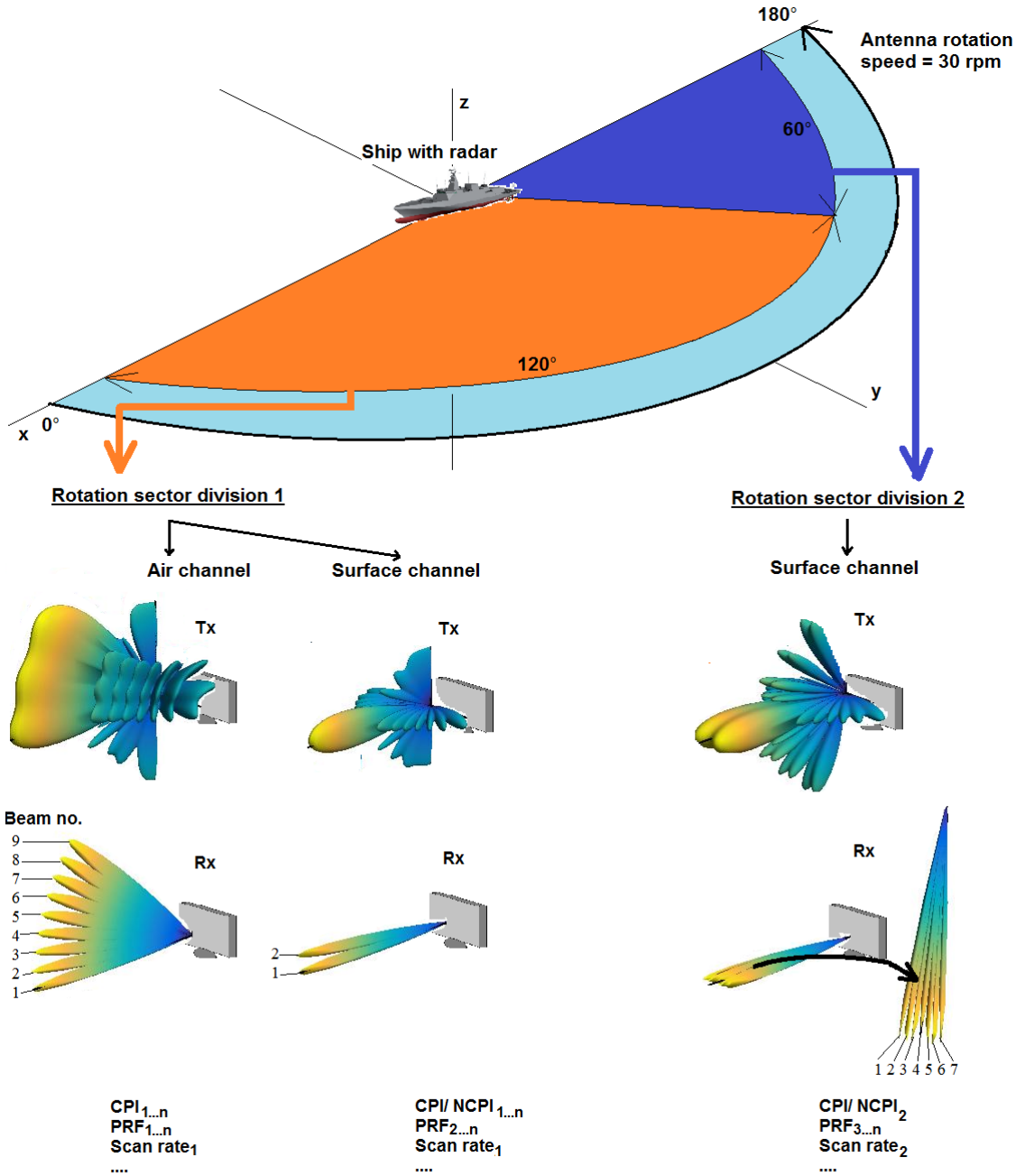

Fig. 3.1. Overview of processing sectors and associated input parameters.

3.1.1 Transmit signal

Range resolution

The range resolution (ΔR, in m) input was used to determine the pulse bandwidth, pulse width and range bin size. The simulation model made use of a simple pulse without any intra-modulation. Complex baseband sampling was used at a sampling frequency (in Hz) set up to be twice the pulse bandwidth. This implied that the sampling time or range gate time would be half the pulse width. The relation of range resolution to range bin size (R_b, in m) can be shown to be:

$$R_b = \frac{\Delta R}{2} \tag{3.1}$$

Peak power

The peak power (in W) input defined the peak power of the synthesised transmit signal. This was prior to transmit amplification gain as used in the Phased Array Toolbox transmitter object.

It will be seen later in this section, that the GOCA-CFAR threshold constant was determined through a non-rotating Monte Carlo simulation in a target free environment (to the associated P_{fa}). The threshold constant was determined through this process due to the complexity of equation 2.28. The desired peak power input was determined through another non-rotating antenna Monte Carlo simulation with the threshold determined from the previous simulation. The simulation was created from the radar simulation model, with the same configuration and processing. The method repetitively allowed the antenna to scan in a thermal noise only (clutter-free) environment with an inserted target at the desired range of initial detection. This represented a priority fast target detection in a suppressed clutter channel (air channel) configuration. The fast target characteristics and range were based on the COO, threat assessment and weapon channel timeline analysis as discussed in chapter 1. It could be possible to calculate the required peak power through the radar range equation and the desired SNR. But the threshold, and not the required SNR, was immediately available. It was therefore preferred to determine the required peak power through simulation.

The non-rotating Monte Carlo method allowed the input of a vector of transmit power values to be assessed, the number of times the test should be repeated per transmit power, the rotation sector, PRF, channel and receive sum beam to be used. The output was a vector of detection probabilities for each transmit power respectively. It is clear that the peak transmit power depended on the fast target (air channel) only. This implied that fast target detection was a priority. The performance of slow target detection was measured with the selected peak power.

Amplification gain

The amplification gain input (in dB) defined the transmit gain of the transmitter amplifier. It was used in the Phased Array Toolbox transmitter object.

3.1.2 Antenna

Position and velocity

The antenna platform position (in m) and velocity (in m/s) inputs were Cartesian position and velocity vector components. The vectors were used in the Phased Array Toolbox platform object. The sensor position and velocity (if accelerating) updated after every PRI.

Rotational speed

The antenna rotational speed (in rpm) input established the counterclockwise pseudo rotation rate whereby the target was rotated around the antenna. In Fig 3.2 the rotational speed is $30rpm$. This value was arbitrarily selected and could be based on various system combat system specifications, for example required target update rate. As mentioned in Chapter 2, the antenna relative coordinate system (with the boresight pointing towards the positive x-axis) would be referenced to the ship relative coordinate system (with the bow pointing towards the positive x-axis) to obtain the true azimuth of the target detection.

Rotation sector of interest

The rotation sector of interest included two inputs, which defined the start and end ship relative azimuth angles (in °) of antenna rotation. This defined the azimuth sector for further input specification over which the antenna rotates with the target and platform position updated at every PRI. The rotation sector of interest in Fig 3.2 is selected as 0° to 180°. Within the rotation sector of interest, sub-sectors could be defined each with unique processing. Also within the rotation sector of interest, was the selected range and sub-sector, which included the target position, within which complete radar processing would be executed.

Array elements

The type of array element could be selected directly from the Phased Array Toolbox antenna objects available. This included isotropic, short dipole, crossed dipole and other elements. The selected element type was ultimately used in the Phased Array Toolbox uniform rectangular

array object. The type of array element would influence the total array pattern as described by equation 2.3.

Other inputs were the number of vertical and horizontal array elements and the distance between the elements of the planar array. These inputs were used in the Phased Array Toolbox uniform rectangular array object. It would determine the minimum array receive beamwidth, which played a role in the number of pulses per CPI. It also played an important role in the transmit and receive weight distributions.

Frequency of operation

In reality the frequency of operation plays an important role in radar system design. It determines the size and weight of the antenna and system, with smaller systems at higher frequencies. The frequency determines the performance against environmental attenuation with lower frequencies having less attenuation. Higher frequency also provides the opportunity for wider bandwidth and better accuracy performance [20]. These specific effects of operating frequency on system design were not tested in the simulation model, although the frequency of operation input (in Hz) was used throughout the simulation model in a variety of processing, such as the phased array weighting and Doppler spectrum. The frequency of operation was selected to correspond with the operating frequency used for the clutter data.

3.1.3 Processing sectors

Rotation sector of interest divisions

The rotation sector of interest divisions input allowed the defined rotation sector to be divided into sub-sectors in which the air and surface channel unambiguous ranges, number of CPIs, PRFs, beamforming, scan patterns and other features could be adjusted. In Fig 3.2 two rotation sector divisions are defined as 0° to 120° and 120° to 180°.

CPIs per rotation sector division

The simulation model was designed in such a way that after each air channel CPI an associated surface channel CPI or NCPI followed. The CPI length was kept constant in a rotation sector division for the air and surface channel respectively. This was done even if the PRF varies from one CPI to the next for the air channel. The reason for this was to maintain the Doppler resolution between CPIs in order to simplify ambiguity resolution in the velocity spectrum. Three different inputs were available for the CPI setup.

- The number of processing intervals (air and associated surface channel) required for ambiguity resolution (with different PRFs for the air channel) and m-of-n detection, were defined for each rotation sector division. In Fig 3.3 there are 3 processing intervals for the first rotation sector division and 1 processing interval for the second rotation sector division. Values were selected arbitrarily in this case and would typically depend on the amount of pulses or dwell time required per CPI.
- The processing intervals per beamwidth dwell time per rotation sector division. In Fig 3.3 there are 3 processing intervals per beamwidth dwell time for the first rotation sector division and 0.7 processing intervals per beamwidth dwell time for the second rotation sector division. It could be seen that defining a processing sector less than one as per the second processing interval, implied that integration will be executed over multiple beams. This normally would require summing the returns of these beam processing channels. Values were selected arbitrarily in this case and would typically depend on the Doppler resolution or integration gain required. The second rotation sector division allowed long dwell time CPI bursts.
- The proportion of the air channel to the surface channel in a processing interval could be defined per rotation sector division. This input ultimately determined the duration of the air channel CPI and its associated surface channel CPI or NCPI. In Fig 3.3 the processing interval for the first rotation sector division has a $7:1$ proportion of air to surface channel dwell time and the second rotation sector division has a $0:1$ proportion. If a zero value was chosen as above for the air channel in the second rotation sector division, it implied that only surface channel processing would be executed in the processing interval. Values were selected arbitrarily in this case. For the first rotation sector division, the interleaved surface channel would typically be short low PRF NCPI bursts only. While the second rotation sector division allowed full use of the processing interval exclusively for the surface channel over multiple horizontal beams for long dwell time CPI bursts and high Doppler resolution.

Sector and range to process

Full processing of the complete rotation sector of interest was very time-consuming on a personal computer. It was therefore made possible to specify a sector and range over which full processing was to be executed. This typically included the area, which includes the target. In Fig 3.2 the sector to process starts at a ship relative angle of 85° and ends at 95°. The range is between $24500\,m$ and $25500\,m$.

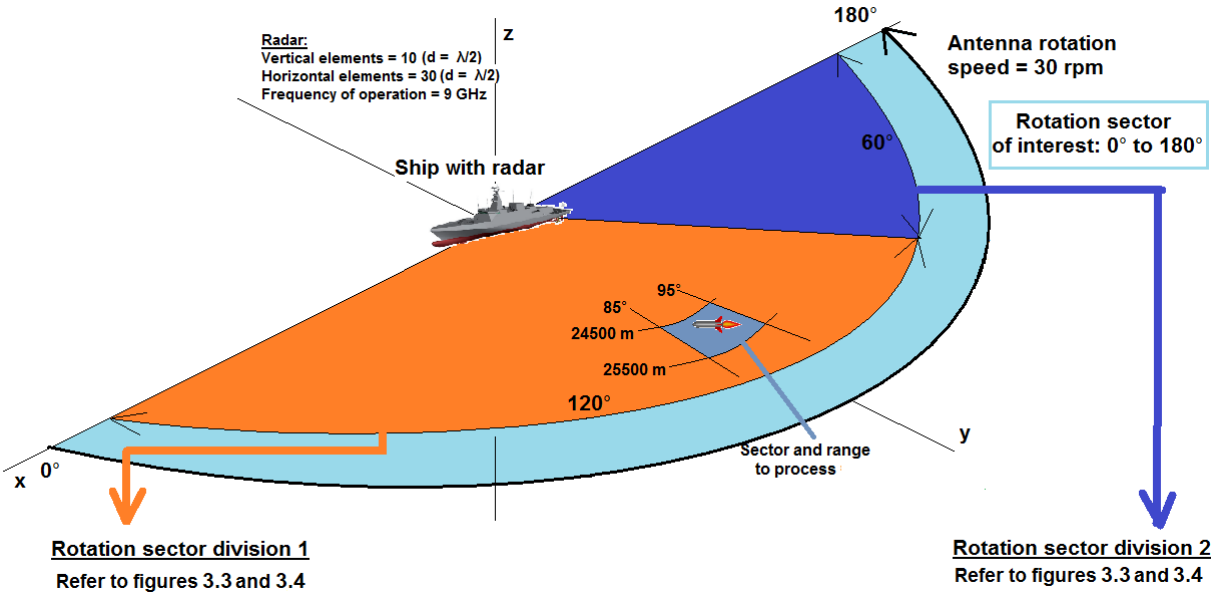

Fig. 3.2. Processing sector inputs.

3.1.4 Pulse repetition frequency

Unambiguous range

The unambiguous range (in m) input was used to determine the PRF for the air and surface channels per rotation sector division. The base PRF (in Hz) was determined as:

$$PRF_b = \frac{c}{2R_{ua}} \tag{3.2}$$

where R_{ua} was the unambiguous range. The PRF was however adjusted (reduced), if needed, to fit the pulses without residual into the channel CPI or NCPI duration as calculated in subsection 3.1.3. This would result in the unambiguous range being slightly larger than that specified. For the air channel, which required ambiguity resolution in range and velocity, the rest of the PRFs (the number of different PRFs is equal to the number of CPIs as determined in 3.1.3) were determined by reducing each PRF such that it would ensure that the target return shifted out of the clutter spectrum and to another frequency bin. The PRFs were further reduced if needed to fit the pulses without residual into the channel CPI duration. For the surface channel, the base PRF was used for all CPIs or NCPIs as no ambiguity resolution was required.

In Fig 3.3 the unambiguous ranges are defined as $15500\,m$ for the air channel and $31000\,m$ for the surface channel in both rotation sector divisions. The adjusted PRFs, number of pulses and ranges are also shown. Ranges were selected arbitrarily with the surface channel unambiguous range typically to the radar horizon and the air channel as required for medium PRF operation.

Maximum range

The maximum range (in m) input was used for the air channel to determine the unambiguous range multiples (per PRF) required to cover the maximum range. The multiples were chosen such that the total range was equal to or larger than the maximum range. In the simulation model, the medium PRF returns did not overlap with the previous pulses as it was in reality. Rather, the model was designed to create a single return waveform over the total range. The return waveform was then folded to represent the pulse with return overlaps. This was repeated at the medium PRF. All other real-time updates for example, target and antenna rotation position, were done as per the real PRF.

Maximum velocity

The maximum velocity input (in m/s) was used for the air channel to determine the unambiguous velocity multiples (per PRF) required to cover the maximum velocity of interest. The multiples were chosen such that the total velocity is equal to or larger than the maximum velocity.

3.1.5 Transmit and receive beams

The azimuth scan rate (in $^\circ/s$) of the transmit and receive beams per rotation sector division could be entered. In Fig 3.3 the arbitrary example angular scan rates are defined as $90^\circ/s$ for the first rotation sector division and $0^\circ/s$ for the second rotation sector division.

The selected scan rate of $90^\circ/s$ for the first rotation sector division implied that after the first rotation sector division of 120° a ship relative azimuth of 180° would be searched. This was done to search the complete rotation sector of interest with the priority air channel. In the second rotation sector division (rotating from 120° to 180°) only surface channel processing was performed, with no scan rate to maximise the target dwell time. In the next rotation, the sector with surface channel processing could for example be shifted to cover a new sector angle. In this way surface surveillance, with maximum dwell time, could be completed after every 3 rotations. This was acceptable as the surface channel was for slow-moving targets that didn't pose an immediate threat.

It has to be noted that in the example, the first rotation sector division already included short dwell surface channel processing interleaved with the air channel. This was not optimal use of radar resources as surface channel processing was performed extensively in the next sector division. However, the interleaved surface channel processing was included for a better understanding of the input possibilities.

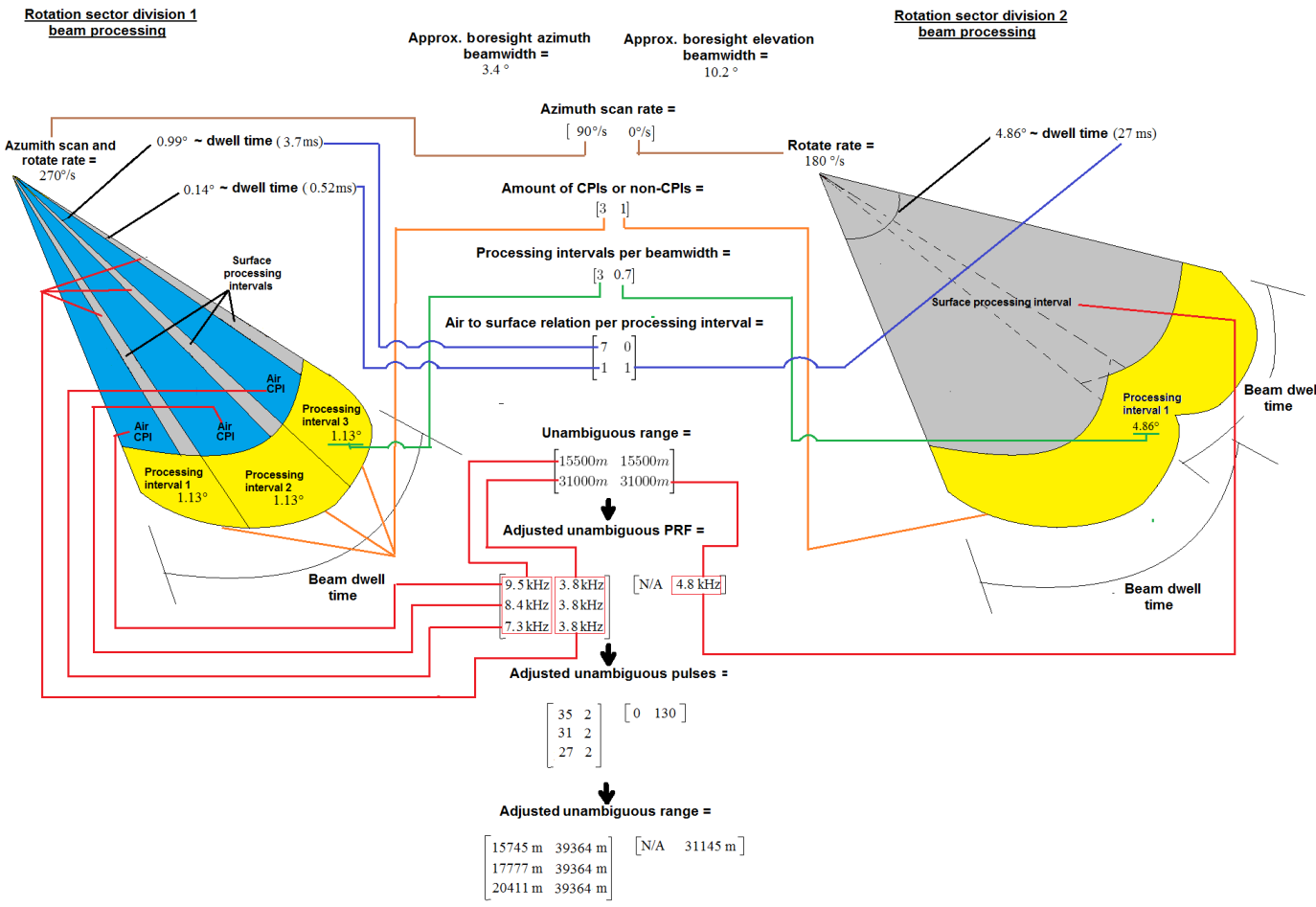

Fig. 3.3. Beam processing intervals and PRF inputs.

Transmit beam

The transmit beam was formed according to the Fourier transform method described in section 2.4. A boresight-only transmit beam was synthesised covering the complete elevation of interest. If the beam was scanned off boresight, a pseudo scanning of the boresight transmit beam was introduced by rotating the target around the antenna. Various inputs were allowed for the synthesis of the transmit beam.

- The antenna relative azimuth angle at which the transmit beam scanning started when the antenna enters a new rotation sector division could be defined. In Fig 3.4 the example transmit beam antenna relative starting angles were defined as 0° for both rotation sector divisions.
- The shape of the linear array beam pattern in azimuth and elevation were defined per rotation sector division. It depended on the volume to be searched as defined in system specifications. The air and surface channels each had their own shape. The defined patterns were used to ultimately define the transmit weights, which were used in the Phased Array Toolbox radiator object. The final element weights were normalised. Furthermore, it is important to note that in the Phased Array Toolbox the array transmit gain (in a linear scale) was equivalent to the array power pattern ($|E_a(az, el)|^2$ for isotropic elements). In Fig 3.4 the transmit beam shape azimuth angles for the air channel are from $-3°$ to $3°$ for the first rotation sector division (there is no air channel processing in the second rotation sector division). The elevation angles for the air channel are from $-5°$ to $45°$. The transmit beam shape azimuth angles for the surface channel are from $-3°$ to $3°$ for the first rotation sector division and $-8°$ to $8°$ for the second rotation sector division. The transmit beam shape elevation angles are from $-5°$ to $10°$ for the first rotation sector division and $-5°$ to $5°$ for the second rotation sector division. Values were selected arbitrarily. It depended on the elevation and azimuth required to be searched. For the surface channel typically low elevation angles were sufficient. The longer dwell time and CPI over multiple beams for the surface channel in the second rotation sector division justified the wider azimuth coverage.

Receive beams

The azimuth and elevation starting angles of the receive beams for the air and surface channels relative to the antenna could be defined per rotation sector division. The beam start angles were used with the scan rate to determine the antenna relative (and ship relative) beam positions after each pulse. It was ultimately used in the Phased Array Toolbox beamformer object.

In Fig 3.4 the example receive beam start positions for the air channel in the first rotation sector division are defined for beam 1 as 0° azimuth and 0° elevation, beam 2 as 0° azimuth and 5° elevation in 5° elevation steps up to beam 9 with 0° azimuth and 40° elevation. The receive

beam start positions for the surface channel in the first rotation sector division are defined for beam 1 as 0° azimuth and 0° elevation and beam 2 as 0° azimuth and 5° elevation. For the second rotation sector division these are defined for beam 1 as −5.1° azimuth and 0° elevation, beam 2 as −3.4° azimuth and 0° elevation in 1.7° azimuth steps up to beam 7 with 5.1° azimuth and 0° elevation. Values were selected arbitrarily. The receive beams volume covered the same volume of the transmit beam.

The output signal power (in W) of the array (with isotropic elements) was [21]:

$$P_s(az, el) = \sigma_s^2 |E_a(az, el)|^2 \tag{3.3}$$

where σ_s^2 was the signal power at the element level. The output noise power was [21]:

$$P_n = \sigma_n^2 |E_n| \tag{3.4}$$

where σ_n^2 was the noise power at the element level and if the noise was spatially isotropic [21]:

$$E_n = \sum_{m=-M}^{M} \sum_{n=-N}^{N} |A_{mn}|^2 \tag{3.5}$$

The SNR after beamforming could be defined as [21]:

$$SNR_a(az, el) = \frac{P_s}{P_n} = \frac{\sigma_s^2 |E_a(az, el)|^2}{\sigma_n^2 |E_n|} \tag{3.6}$$

If the SNR at the element was defined as [21]:

$$SNR_e = \frac{\sigma_s^2}{\sigma_n^2} \tag{3.7}$$

the array gain (G_a) could be defined as the array SNR gain [21]:

$$G_a(az, el) = \frac{SNR_a(az, el)}{SNR_e} = \frac{|E_a(az, el)|^2}{|E_n|} \tag{3.8}$$

It is important to note that in the Phased Array Toolbox the array receive gain (in a linear scale) was as described in equation 3.8 [22]. Furthermore, a distortionless constraint was implemented whereby the weight amplitudes were chosen such that the array factor was normalised at the main response axis (where $az = az_s$ and $el = el_s$) so that [21]:

$$E_a(az_s, el_s) = 1 \tag{3.9}$$

This provided the advantage of keeping the element level received signal 'undistorted' with the same gain factor due to noise decorrelation in the array summation.

Summing of different receive beam signals allowed for possible monopulse angle estimation and coherent integration across multiple beams. Although the model didn't incorporate accurate

angle estimation techniques, coherent integration across multiple beams was possible. The detection processing was performed on the resulting sum beams. In Fig 3.4 the sum beams for the air channel in the first rotation sector division are defined as sum beam 1 = beam 1 + beam 2, sum beam 2 = beam 2 + beam 3 up to sum beam 8 = beam 8 + beam 9. The sum beams for the surface channel in the first rotation sector division are defined as sum beam 1 = beam 1 + beam 2 and for the second rotation sector division are defined as sum beam 1 = beam 1 + beam 2, sum beam 2 = beam 2 + beam 3 up to sum beam 6 = beam 6 + beam 7.

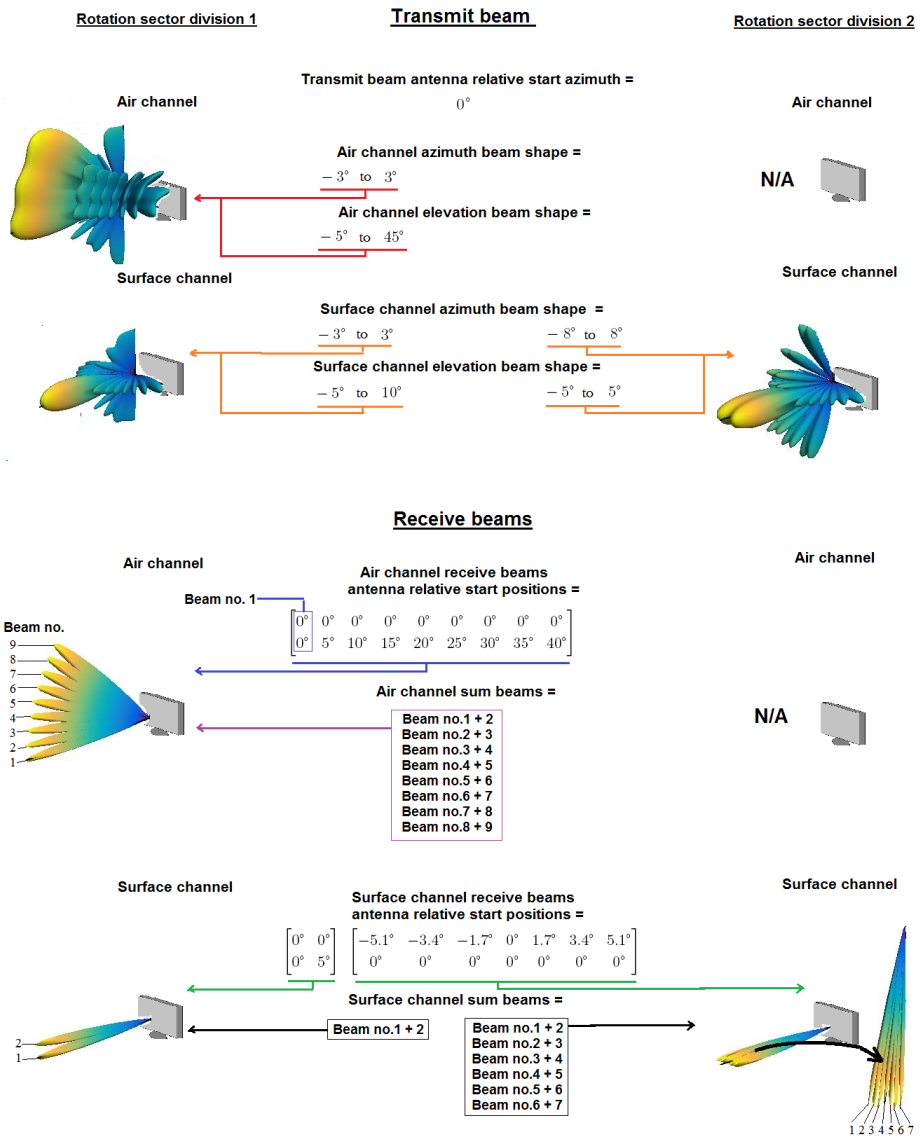

Fig. 3.4. Transmit and receive beam inputs.

3.1.6 Clutter

Complex clutter data sets were used from the CSIR Fynmeet Sea Clutter Measurement Trial [13]. A clutter data set typically consisted of a $Q \times R$ matrix where the Q-dimension represented slow time (per pulse) and the R-dimension represented the fast time (per range bin) of the illuminated patch of ocean. Two sets of clutter could be chosen and inserted whereby the first set contained clutter measurements nearer to the radar, while the second set contained clutter measurements further away. The reason for choosing two sets at different ranges was to accommodate (to some extent) the variation in statistical properties of the data. Typically, these two sets should be taken from the same geographical position, direction and period of day. Only fixed frequency non-rotating operation data were used.

With the clutter data sets, an extensive list of environmental, geographical and radar setup data was provided. More details for the measurement values of the setup data used for the simulations were provided in the following chapter. As far as possible, this data was used as inputs to the model. Inputs related to clutter were the sea state (Douglas), antenna grazing angle, antenna height (in m), azimuth beamwidth (in °), wind azimuth direction relative to the antenna look direction or sector to process (in °), the range at which the closer clutter data should transfer to the far clutter data (in m), the length of the clutter data to use to determine the clutter power (in s), the PRF used for the clutter measurement (in Hz), the maximum speed of the clutter determined from the velocity spectrum (in m/s), the velocity spectrum to suppress in sum beams affected by clutter (in m/s) and the air and surface receive beams per rotation sector division to insert clutter into.

The process to adapt information of the real clutter data sets and prepare clutter to insert into the target and noise signal is illustrated in Fig 3.5. Inputs were used in the GIT model (equations 2.7 to 2.14) to determine the clutter area reflectivity (σ^0). The clutter area model (equation 2.16) was used to determine the clutter area (A_c) for each range bin as a $1 \times N$ vector. The clutter area reflectivity and clutter area vector were then multiplied (according to equation 2.15) to determine the clutter RCS (σ_c) as a $1 \times N$ vector. Using the clutter RCS and other radar system inputs the radar range equation (equation 2.17) was used to determine the average clutter power and signal amplitude. This was a $2 \times N \times M$ matrix where the 2-dimension represents the air and surface channel, the N-dimension the range bins and the M-dimension the sector division.

A specific range bin of the near and far clutter data sets were chosen to determine the average clutter power of the measurement as illustrated in Fig 3.6. For this purpose a period of T-seconds (which should be of considerable length) was selected. The noise in the samples ($(T)(PRF)$-samples) beyond the clutter spectrum was removed by low-pass (LP) filtering the frequency spectrum. The average power and signal amplitude of the filtered signal was determined for the near and far clutter signal. The average clutter signal amplitude matrix from the previous paragraph was divided by the real data average signal amplitude. The

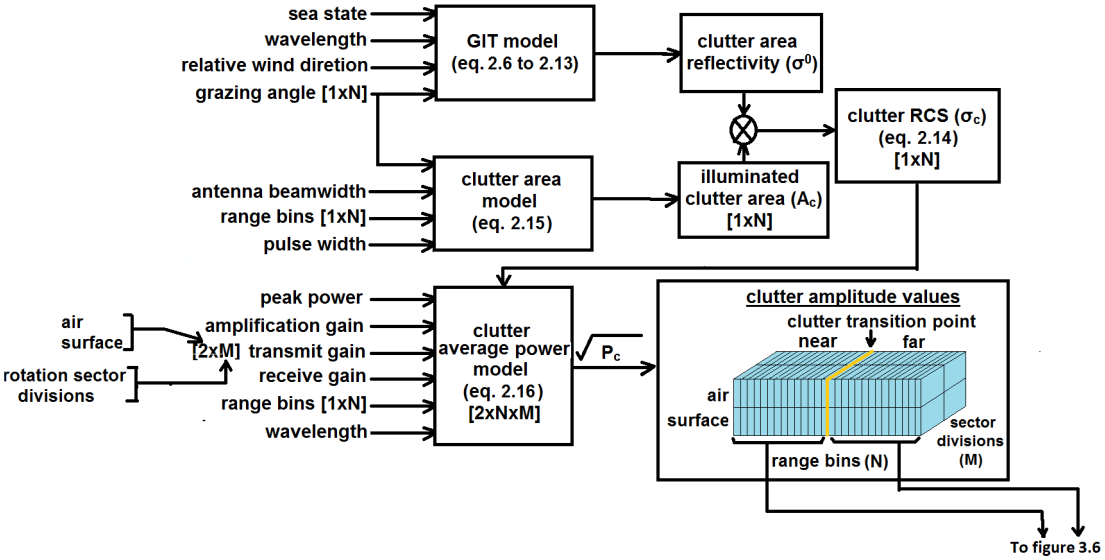

Fig. 3.5. Theoretical clutter amplitude values.

near clutter values before the transition point were divided by the near clutter average signal amplitude. The far clutter values after the transition point were divided by the far clutter average signal amplitude. This resulted in a new $2 \times N \times M$ matrix of clutter amplitude adjustment factor values.

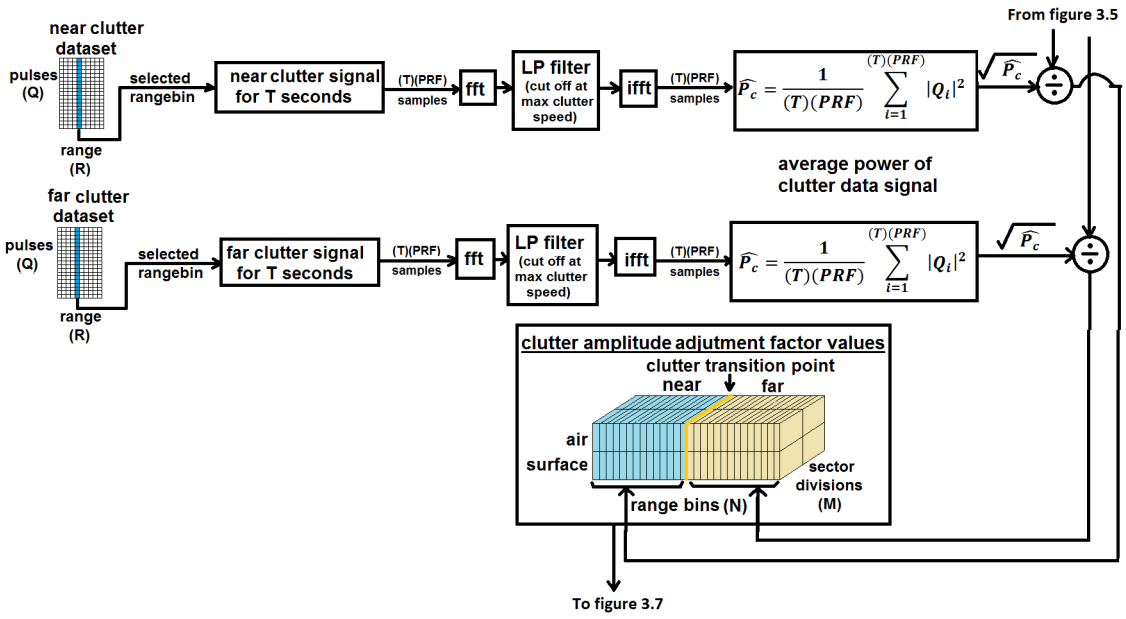

Fig. 3.6. Clutter amplitude adjustment factor values.

In the simulation model each CPI or NCPI had a predetermined dwell time and PRF. The PRF of the clutter data sets were different from this predetermined PRF. This resulted in an

incorrect clutter spectrum distribution if the clutter data set pulses are used directly with a different PRF as illustrated in Fig 3.7. The number of pulses that would fit in the simulation dwell time with the PRF as per the clutter data set was therefore firstly selected. This resulted in a $V \times R$ array where the V-dimension represented the selected clutter data set pulses and the R-dimension the range bins. The clutter data pulse selection had an offset based on the use of pulses for previous CPIs and NCPIs as well as for azimuth beam offsets.

Each of the range bins of the near and far clutter data were transformed into the frequency spectrum through a fast Fourier transform (FFT) - as shown in Fig 3.7. Additional pulses with zero amplitude data were added (or pulses were removed) and the spectrum was LP filtered with the cut-off at the maximum clutter speed. The inverse fast Fourier transform (IFFT) was then applied to each range bin and the resulting signal amplitude was scaled to obtain the original signal amplitude in a $V_{new} \times R$ matrix. This resulted in modified near and far clutter data sets with the PRF (and number of pulses) adjusted to that of the simulation model.

As each clutter pulse was required to be inserted into the target and noise return pulse, multiples of the modified data sets were stitched together with the near clutter data before the clutter transition bin and the far clutter data after the clutter transition bin up to the required maximum range. This resulted in a $1 \times N$ vector, which was element-wise multiplied along the N-dimension (range) of the selected row (channel) and page (sector division) of the clutter amplitude adjustment factor matrix values. The resulting $1 \times N$ vector contained the clutter returns, which could be inserted into the target and noise return pulse as shown in Fig 3.7. The entire clutter pulse preparation process is illustrated in Fig 3.8.

3.1.7 Target

Position and velocity

The target position (in m) and velocity (in m/s) inputs were Cartesian x, y and z position and velocity vector components. The vectors were used in the Phased Array Toolbox platform object. The target position and velocity (if accelerating) updated after every PRI.

RCS

The mean RCS (in m^2) input of the targets were used in the radar target object of the Phased Array Toolbox. The target statistical model was also allowed. For the simulations, only Swerling 0 (Non-fluctuating) targets were used.

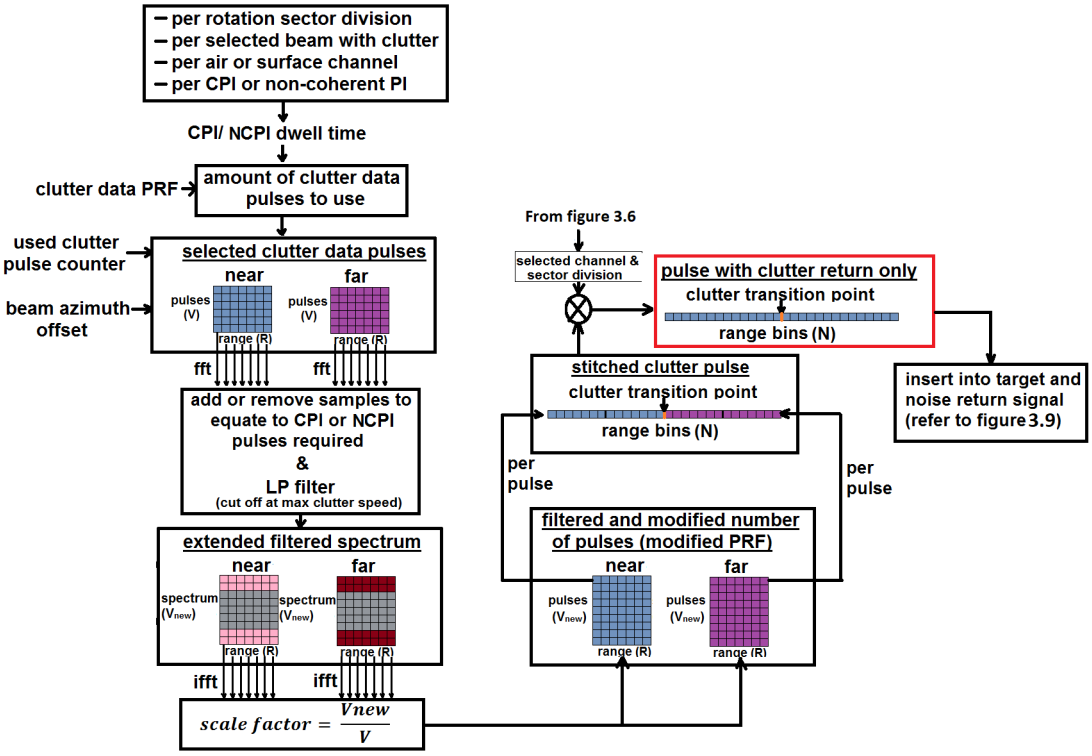

Fig. 3.7. Adjusted clutter returns.

3.1.8 Receiver

Amplification gain

The amplification gain input (in dB) defined the receive gain of the receiver amplifiers at element level. The amplification gain was used in the Phased Array Toolbox receiver pre-amplifier objects. The receiver pre-amplifier object applied the gain before the insertion of noise in the receive signal.

Noise power

The noise signal was inserted independently after each receive amplifier at element level. Inputs to determine the power of the noise signal were the noise figure (in dB), noise bandwidth (in Hz) and receiver temperature (in K). The power of the noise signal according to the Phased Array Toolbox was:

$$\sigma_n^2 = k_B B T F \tag{3.10}$$

where k_B was the Boltzmann's constant, B was the noise bandwidth (in Hz), T was the receiver temperature (in K) and F the noise figure (in linear units).

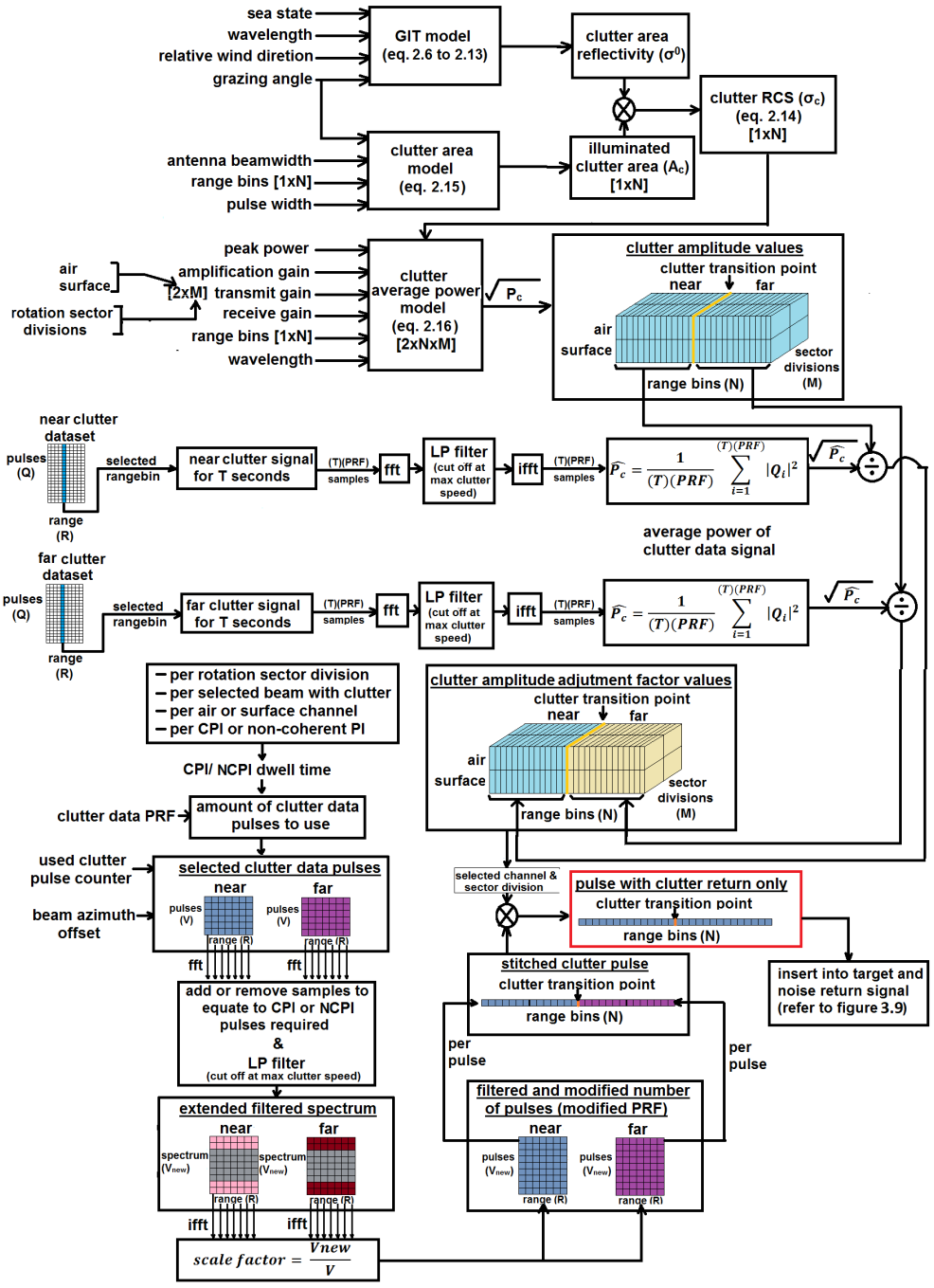

Fig. 3.8. Clutter pulse preparation process.

3.1.9 Detection

CFAR

The number of guard cells and reference cells could be specified. It formed a square 2D test data set if required in range and Doppler.

To determine the threshold for the air channel, as per equation 2.22, the GOCA-CFAR constant needed to be determined. As seen in equation 2.28, determining the constant from this mathematical model would require a complex iterative process. Instead of using the mathematical model, the desired GOCA-CFAR constant was determined through a non-rotating antenna Monte Carlo simulation. The simulation was created from the radar simulation model, with the same configuration and processing. The method repetitively allowed the antenna to scan in the thermal noise only (clutter and target free) environment. The Monte Carlo method allowed the input of a vector of threshold constants to be assessed and the number of times the test should be repeated per threshold constant. The output was a vector of estimated false alarm probabilities for each threshold constant respectively. Equation 2.28 could be used to verify that the required P_{fa} and associated constant were acceptable. The threshold was optimised for a clutter suppressed environment (as is the case for the air channel). The environment seemed clutter-free, which could justify the use of a CA-CFAR detection threshold that would be easier to determine. However, due to the edges in the suppression zones and the possibility of clutter edges extending beyond the suppression zone for ranges close (or multiples of these in medium PRF operation) to the radar a GOCA-CFAR detection threshold was preferred.

For coherent surface channel processing (with no clutter suppression), no Monte Carlo simulation was developed to determine the optimal threshold for the GOCA-CFAR method. Different thresholds for the surface channel could be tested by adjusting the GOCA-CFAR constant and running the radar simulation model.

There were additional optional configurations for the surface non-coherent channel processing and detection threshold settings:

- If the surface pulses were non-coherently integrated in a NCPI, to a single pulse, a CA-CFAR detector could be used. The surface threshold factor could be entered separately. No Monte Carlo simulation was developed to determine the optimal threshold. Different thresholds for the surface channel could be tested by adjusting the CA-CFAR constant and running the radar simulation model.
- If the surface pulses were non-coherently integrated in a NCPI, to a single pulse and subjected to a time-varying gain, a constant linear law threshold detector could be used. The surface threshold could be entered separately. A desired constant threshold was determined through a non-rotating antenna Monte Carlo simulation whereby various

thresholds were defined to determine the associated P_d and P_{fa}.

M-of-n detection

The number of detections ('m') required at a specific range and Doppler bin of the defined number of CPIs or NCPIs ('n') required for m-of-n detection, could be defined for each rotation sector division. This value had to be less or equal to the number of CPIs or NCPIs ('n') per rotation sector division. For example, in Fig 3.3, the value must be 3 or less (but larger than 0) for the first sector division and 1 for the second rotation sector division.

3.2 Simulation model configuration and processing

The radar simulation model used the inputs in a process that allowed some fundamental radar processing algorithms to produce a detection table. The independent variables, specifically the beamforming and scan pattern techniques, were adjusted to evaluate this performance. The simulation model layout and process flow is illustrated in Fig 3.9 to 3.12. The entire simulation and processing model is illustrated in Fig 3.12. It is important to note that, because the model was implemented in software, the weights could be adjusted at element level and beamforming was done on array level. This allowed flexibility to shape transmit beams and form multiple receive beams as required. Beam shapes, beamforming and scan patterns could be formed for analog, subarray digital or element digital arrays.

As shown in Fig 3.9, the radar waveform was amplified and transmitted through the phased array beamformer, which applied the calculated weights to form a transmit beam that covered the complete volume of interest. The antenna gain was applied to the signal in the antenna relative direction of the target ($|E_a(az_{target}, el_{target})|^2$). The two way free space path loss and Doppler shift was applied to the signal for the target position and velocity. For a fractional delay of the signal between range bins, linear interpolation was applied to scale the return signal amplitude per range bin. The signal amplitude was adapted based on the target RCS. It was collected in the elements with the element gain and amplified by the receiver gain. Independent noise signals were added based on the defined power. For each beam, the receive weights and summation of all weighted element signals were performed. The receive gain was inherently applied as per equation 3.8. This resulted in a $1 \times N$ signal vector, where the N-dimension represented the maximum range for the air or surface channel.

The air channel will be discussed in this paragraph. The clutter pulse calculated in subsection 3.1.6 was inserted into the signal pulse with the target and noise as shown in Fig 3.10. The signal was folded as per the specified PRF and unambiguous range (to N_{new}-range bins). At the end of the air channel CPI a $B \times P \times N_{new}$ data cube existed where the B-dimension represents the beams, the P-dimension the pulses and the N_{new}-dimension the range bins. The

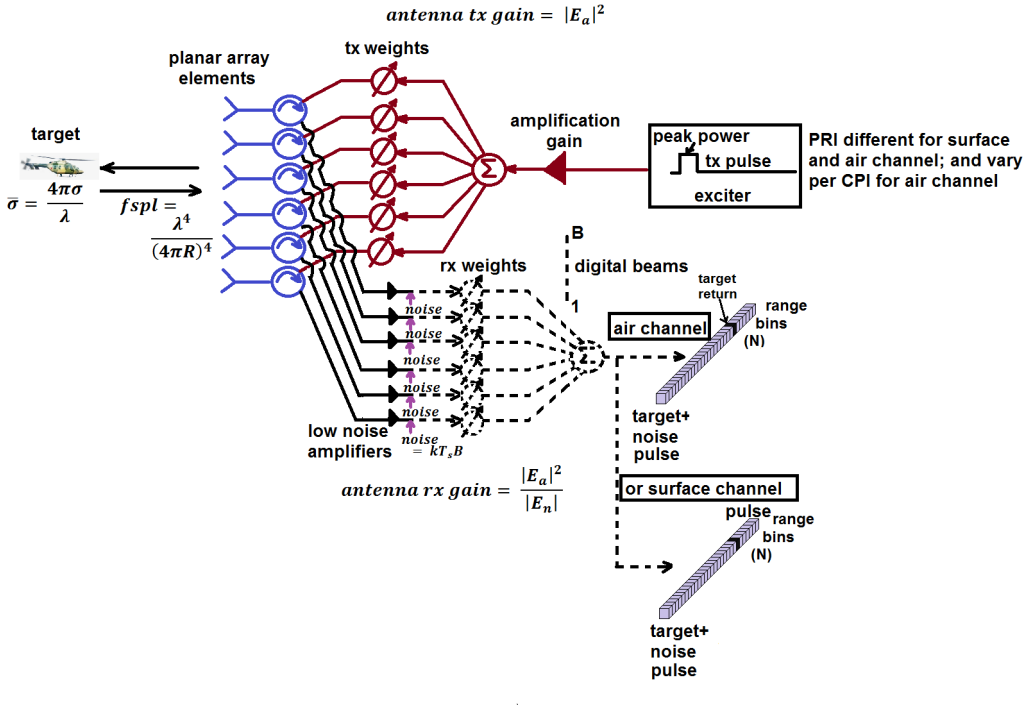

Fig. 3.9. Transmit and receive process.

beams were summed as per the user inputs and matched filtering was applied for each pulse. The bins containing the data of the range to process were isolated, and a hamming window and FFT were applied across each beam's range bin data (the hamming window would reduce FFT sidelobe levels). The result was a $B_{new} \times P \times N_{process}$ processing data cube where the B_{new}-dimension represented the summed beams, the P-dimension the velocity spectrum and the $N_{process}$ dimension the selected range bins of interest. The clutter spectrum was filtered out, as specified in beams where clutter had been inserted. GOCA-CFAR threshold detection was executed with a threshold factor determined through simulation. Thereafter, previous CPI data was used for ambiguity resolution and m-of-n detection. The detection results were then sent to the output air detection result table for the sector division.

For the surface channel the clutter pulse calculated in subsection 3.1.6 was inserted into the signal pulse with the target and noise as shown in Fig 3.11. At the end of the surface channel CPI or NCPI a $B \times P \times N$ data cube existed where the B-dimension represented the beams, the P-dimension the pulses and the N-dimension the range bins. The beams were summed as per the user inputs and matched filtering was applied for each pulse. Coherent Doppler processing could be employed as per the air channel. However, often it was found that not enough pulses are available to develop a FFT with enough Doppler bins for proper GOCA-CFAR detection processing. Therefore non-coherent processing was optionally available. The following processing schemes were available:

- A Doppler processing scheme could be selected (in a CPI), the bins containing the data

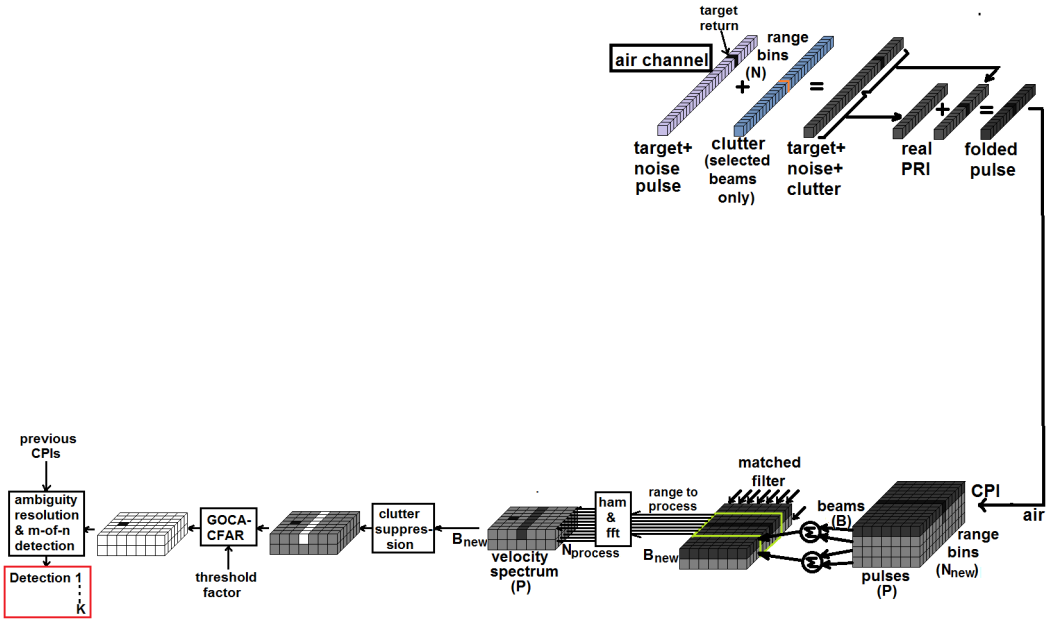

Fig. 3.10. Air channel processing.

of the range to process were now isolated, and a hamming window and FFT were applied across each beam's range bin data (the hamming window will reduce FFT sidelobe levels). The result was a $B_{new} \times P \times N_{process}$ processing data cube where the B_{new}-dimension represented the summed beams, the P-dimension the velocity spectrum and the $N_{process}$ dimension the selected range bins of interest. There was no clutter suppression as per the air channel. GOCA-CFAR threshold detection was executed with the selected threshold factor. Thereafter, previous CPI data was used for m-of-n detection. The detection results were then sent to the output surface detection result table for the sector division.

- A non-coherent integration scheme (in a NCPI) with a square law CA-CFAR detection processing could be selected. Non-coherent integration was implemented for each beam. This resulted in a $B_{new} \times 1 \times N$ datacube where the B_{new}-dimension represented the summed beams, the 1-dimension the integrated pulse and the N dimension the range bins. The bins containing the data of the range to process were now isolated, and CA-CFAR detection was performed with the selected threshold factor. Thereafter, previous NCPI data was used for m-of-n detection. The detection results were then sent to the output surface detection result table for the sector division.

- A non-coherent integration scheme (in a NCPI) with linear law constant threshold detection processing could be selected. A time-varying gain was applied across the range bins to compensate for signal power loss across the range. Non-coherent integration was implemented for each beam. This resulted in a $B_{new} \times 1 \times N$ datacube where the B_{new}-dimension represented the summed beams, the 1-dimension the integrated pulse and the

N dimension the range bins. The bins containing the data of the range to process were now isolated, and constant threshold detection was performed with the threshold that was determined through simulation. Thereafter, previous NCPI data was used for m-of-n detection. The detection results were then sent to the output surface detection result table for the sector division

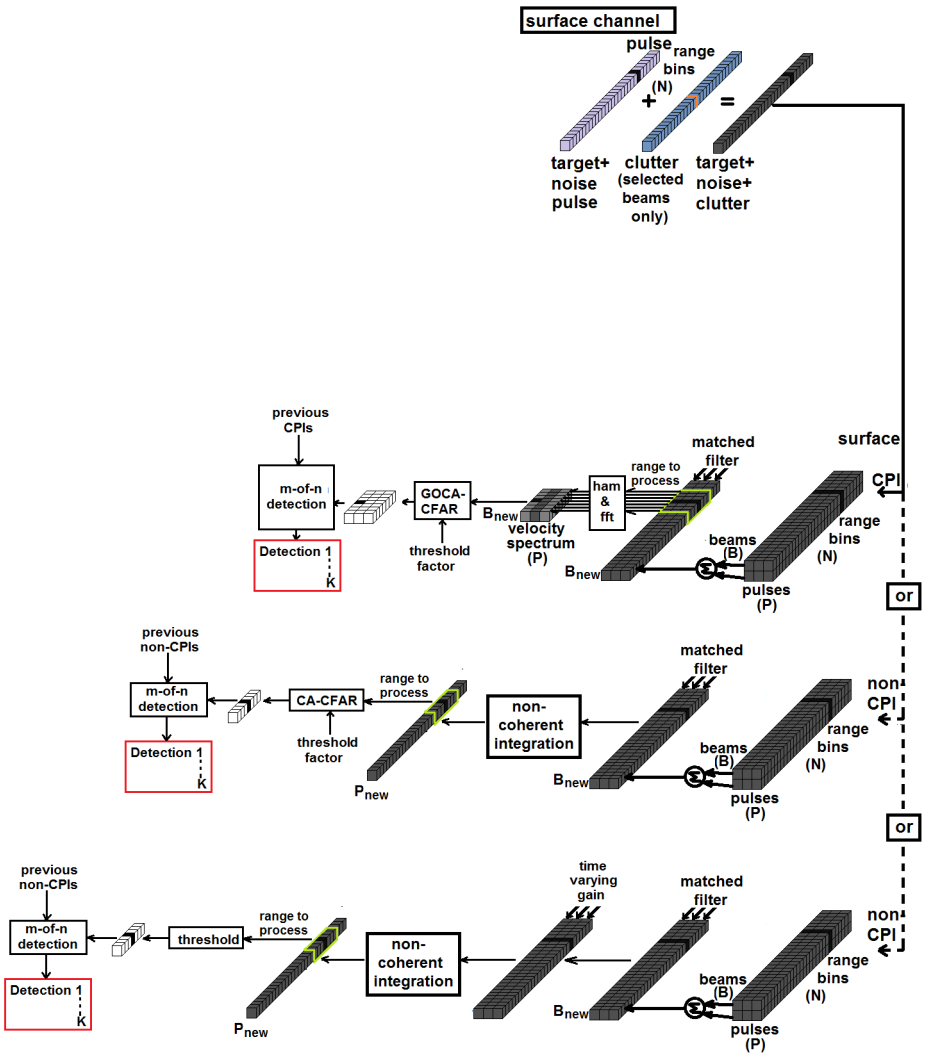

Fig. 3.11. Surface channel processing.

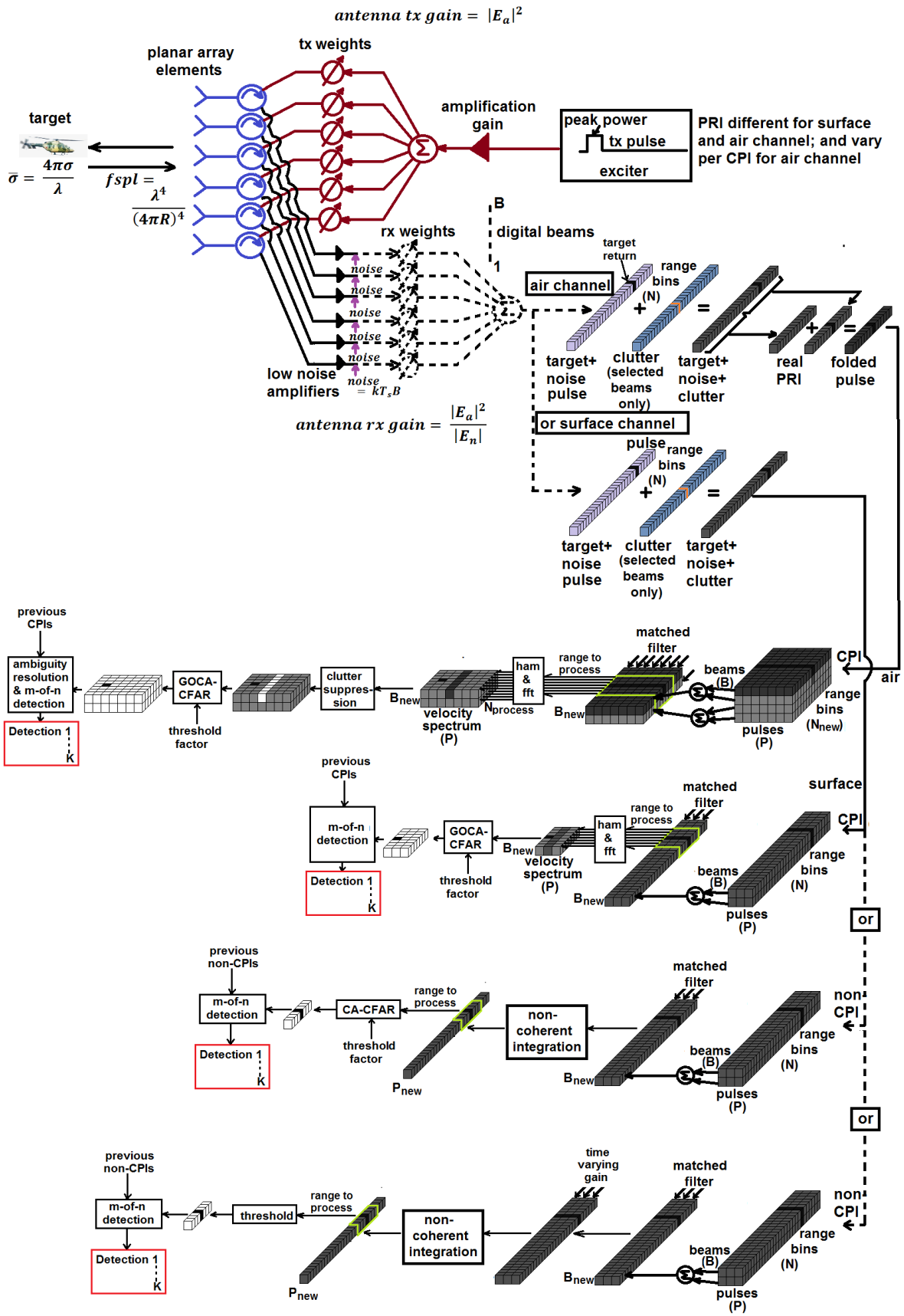

Fig. 3.12. Simulation processing model.

3.3 Outputs

The output was a detection table for the air and surface channel per rotation sector division. A table would include the sum beam, range (in m), radial velocity (in m/s) and CPI or NCPI azimuth start and end angle (ship relative, in °) for every detection.

3.4 Summary

This chapter discussed the design of the radar simulation model. Specifically, insight was provided on the user inputs; simulation model configuration and processing; and the outputs.

The user inputs included variables applicable to the transmit signal, antenna, processing sectors, PRF, transmit beams, receive beams, clutter, target, receiver and detection threshold. The variables might have had associated processing to prepare it for use in the simulation model.

The radar simulation model used the inputs in a process that allowed some fundamental radar processing algorithms to produce a detection table. The simulation model process flow was described and illustrated in this chapter. The independent variables, specifically the beamforming and scan pattern techniques were adjusted to evaluate the performance.

Chapter 4

Results and Discussion

In this chapter, the radar simulation model was used with specific fast conventional and slow asymmetric targets in sea clutter based on system specifications. Different radar beamforming and scan patterns were used to determine and compare the detection performance against these targets with the simulation model.

4.1 Target system specifications

The COO for the multi-mission naval ship in this model included conventional 'blue-water' operations and littoral warfare operations. Common threats that could be encountered are high end SSMs and low end small slow-moving targets like UAVs and small boats. The required war fighting capabilities included detection, control and engagement; detection was the capability under evaluation in this project. A system detection specification for the simulation was used for a fast low flying SSM and UAV as illustrated in Table 4.1. This is normally derived from complex analysis of various factors including the weapon channel timeline analysis. In this case the values were arbitrary.

In Table 4.1 the detection probability for the SSM after a single rotation scan was 90% at 23 km. This allowed enough time for tracking (from consecutive rotation scans) and classification of the threat when it reached a specific minimum range to allow enough time for a proper engagement. For the UAV at 1/2 the RCS ($0.05\,m^2$) of the SSM, the air channel detection range in a clutter-free environment would reduce to $(1/2)^{1/4}$ the range of the SSM for a similar detection probability. This equated to a range of $19.3\,km$. To derive a detection range performance specification for the UAV based on the available radar transmit power in the presence of real clutter, a range from $19\,km$ would be tested for constabulary duties up to an arbitrary minimum range of $7\,km$. This was to allow sufficient time for further classification by optical systems and possible engagement if required. It had to be kept in mind that the maximum $19\,km$ range is based on the air channel performance. The UAV would be tested in the clutter spectrum, which

would only be detected in the surface channel with different array transmit and integration gains. This would yield different detection performances.

Table 4.1. System specification elements example.

Air detection	
System specification	Threshold value
Single rotation scan $P_d \geq 0.9$ per sum beam for an SSM with the following characteristics: $speed \leq 333\,m/s$ $RCS \geq 0.1\,m^2$ (SW 0) $altitude \geq 10\,m$ $sea\ state \leq 3$ $P_{fa} \leq 1 \times 10^{-5}$	$23\,km$
Single rotation scan $P_d \geq 0.9$ per sum beam for a UAV with the following characteristics: $speed \leq 15\,m/s$ $RCS \geq 0.05\,m^2$ (SW 0) $altitude = 10\ to\ 1000\,m$ $sea\ state \leq 3$ $P_{fa} \leq 0.06$	$7\ to\ 19\,km$

4.2 Clutter data sets

The near and far clutter data sets that were used in this chapter were selected based on appropriate environmental, geographical and radar setup data. The two sets were taken from the same geographical position, direction and period of day. A fixed frequency non-rotating mode of operation was used.

4.2.1 Near clutter data set

Some important environmental, geographical and setup data for the near clutter data set is summarised in Table 4.2. A geographical overview of the measurement setup is shown in Fig 4.1.

The clutter amplitude data for all the pulses over the range extent is shown in Fig 4.2. The large mean wave structure was clearly visible over time with the slow decorrelation in the order of seconds for a specific range bin. Fig 4.3 is a zoomed in illustration of the first $200\,ms$ of the clutter amplitude data over the range extent. Although the large structure mean power

Table 4.2. Near clutter data set peripheral data.

Setup data	Value
Location	Overberg Test Range
Dataset	CFC17-004
Date	03 August 2006
Time	13:22:06.828
Duration	301672 PRIs (60.3342 s)
Transmit frequency	9 GHz
PRF	5 kHz
Tracking range	3000.63 m
Range extent	960 m (64 gates), 15 m resolution
Wind speed 8 hour avg.	11.4 kn, 254.7° N, (Sea State 3)
Azimuth look direction	165.5° N
Antenna height	67.03 m
Azimuth beamwidth	1.8°

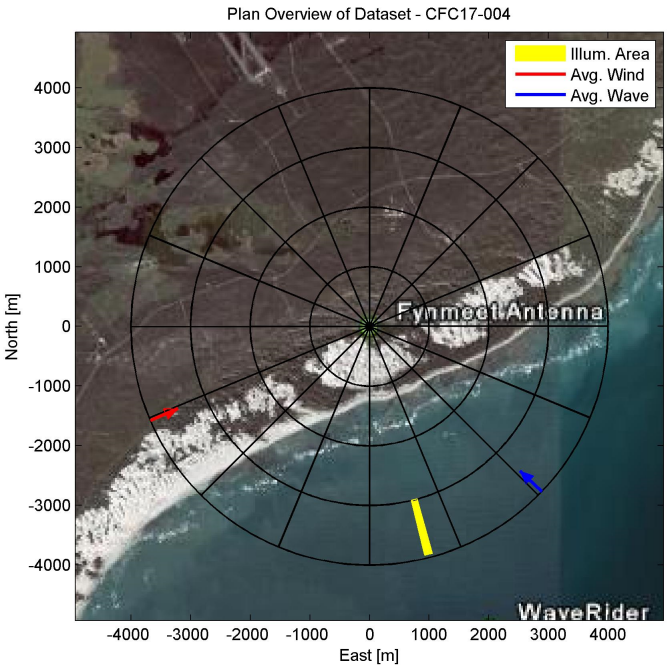

Fig. 4.1. Geographical overview for the near clutter measurement setup [CSIR].

was still visible, the speckle component with shorter decorrelation time in the order of a few milliseconds was now visible.

The clutter velocity power spectrum is shown in Fig 4.4. It could be seen that the clutter

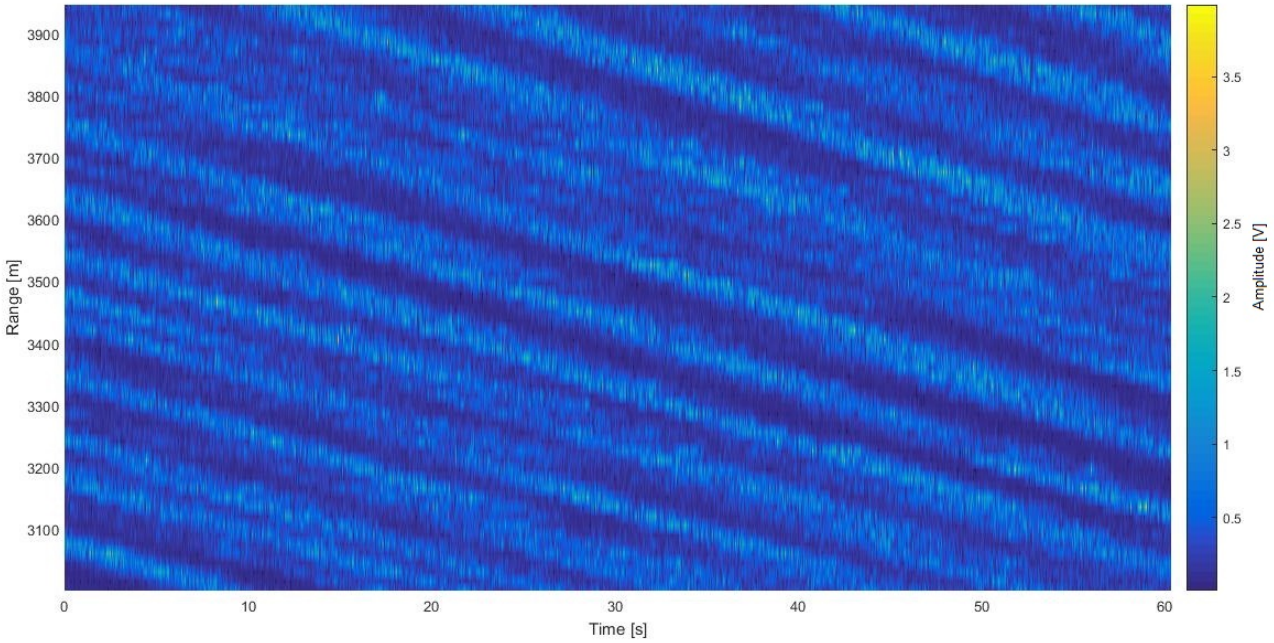

Fig. 4.2. Near clutter amplitude data for all the pulses over the range extend.

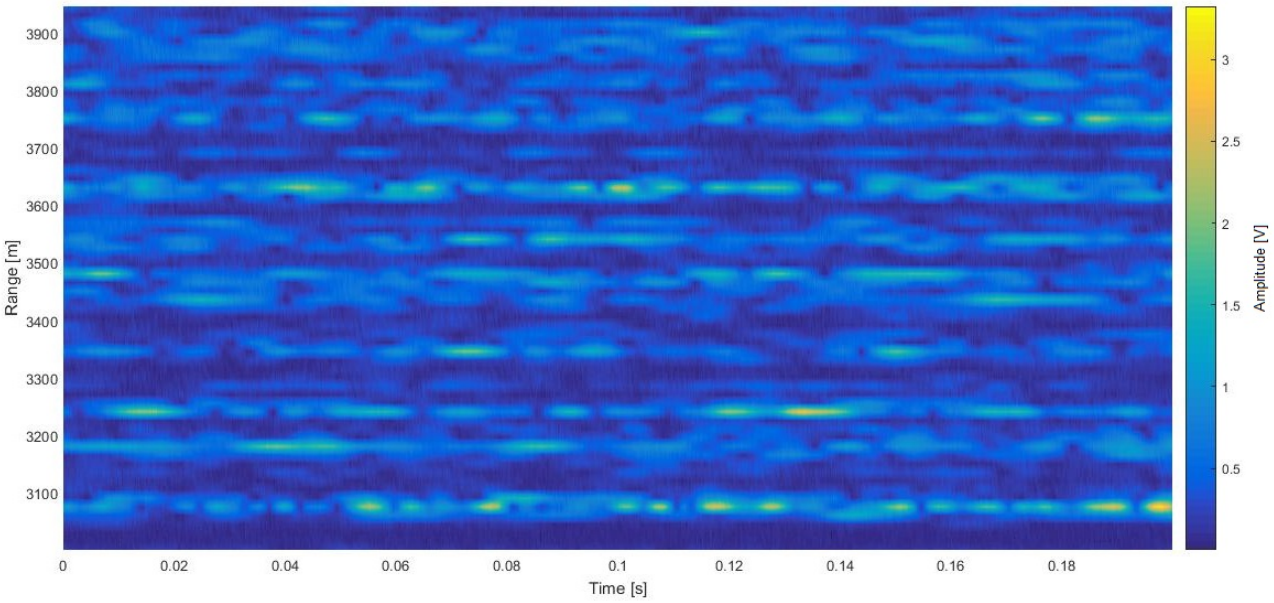

Fig. 4.3. Near clutter amplitude data for the first 200ms over the range extend.

spectrum was mostly positive, which implied a movement of the wave structure towards the radar. It was further apparent that a good clutter suppression velocity estimation was approximately $6\,m/s$ for fast target detection.

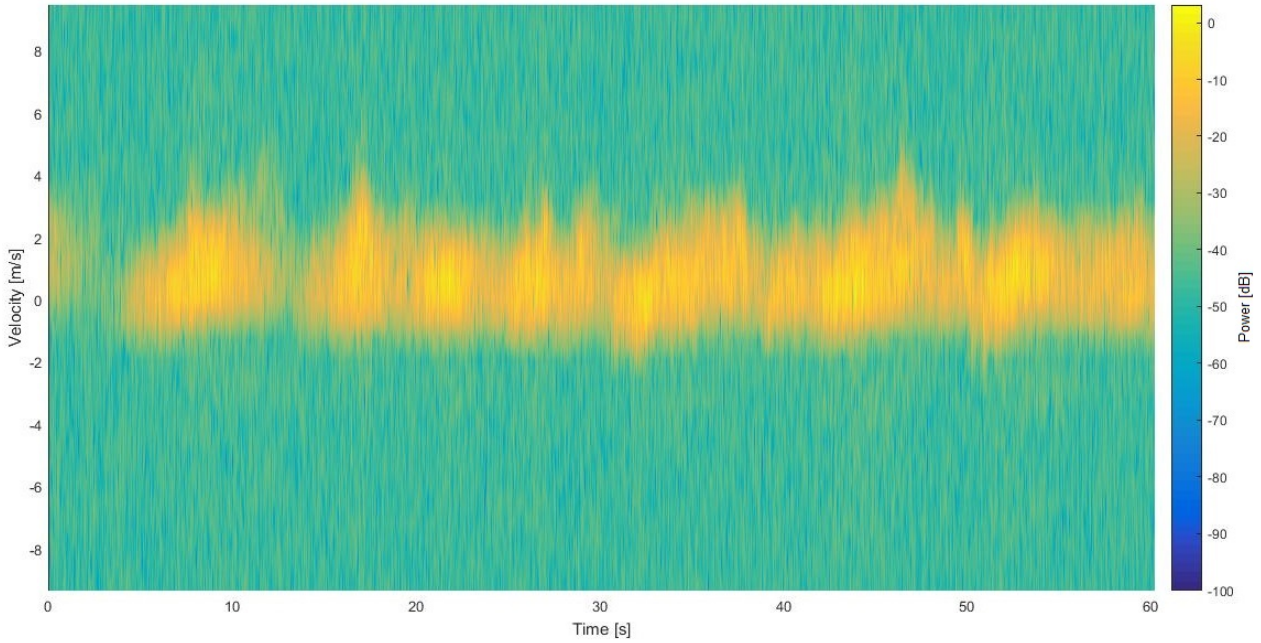

Fig. 4.4. Near clutter velocity spectrum (in dB).

A PDF histogram of all the clutter data amplitudes for the first range bin is shown in Fig 4.5. The mean amplitude was calculated and a shape parameter was selected that would approximately fit the histogram. The scale parameter was then determined using equation 2.19. A K-distribution PDF was then plotted using equation 2.18 to overlay the histogram. The shape parameter was adjusted and scale parameter recalculated until a good fit of the K-distribution over the histogram was established. The K-distribution shape parameter was estimated to be 0.7 and the scale parameter 3.07. The small shape parameter ($0 < v < 1$) implied spiky clutter, which would negatively impact the CFAR detector performance.

4.2.2 Far clutter data set

Some important environmental, geographical and setup data for the far clutter data set is summarised in Table 4.3. A geographical overview of the measurement setup is shown in Fig 4.6.

The clutter amplitude data for all the pulses over the range extent is shown in Fig 4.7. The large mean wave structure was not really visible anymore. The receiver noise possibly played a significant role due to the smaller clutter-to-noise ratio (CNR).

The clutter velocity power spectrum is shown in Fig 4.8. The clutter spectrum was mostly positive, which implied a movement of the wave structure towards the radar. The ratio of clutter power to the higher frequency noise power was less compared to that of the near clutter in Fig 4.4.

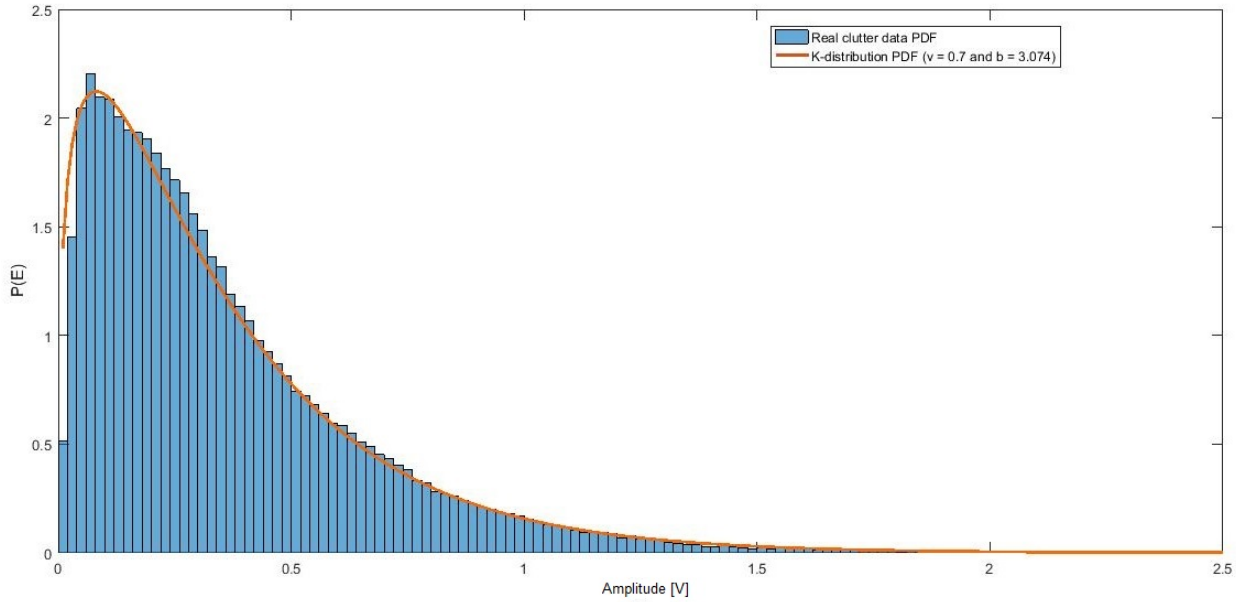

Fig. 4.5. Near clutter amplitude pdf and K-distribution.

Table 4.3. Far clutter data set peripheral data.

Setup data	Value
Location	Overberg Test Range
Dataset	CFC17-005
Date	03 August 2006
Time	13:24:51.734
Duration	301447 PRIs (60.2892 s)
Transmit frequency	9 GHz
PRF	5 kHz
Tracking range	10000.6 m
Range extent	960 m (64 gates), 15 m resolution
Wind speed 8 hour avg.	11.4 kn, 254.7° N, (Sea State 3)
Azimuth look direction	165.5° N
Antenna height	67.03 m
Azimuth beamwidth	1.8°

A PDF histogram of all the clutter data amplitudes for the first range bin is shown in Fig 4.9. A K-distribution PDF was then plotted using equation 2.18 to overlay the histogram. The shape parameter was adjusted and scale parameter recalculated until a good fit of the K-distribution over the histogram was established. The shape parameter was estimated to be 25 and the scale parameter 31.4. The larger shape parameter (compared to the near clutter PDF in Fig 4.5), implied the possibility of less spiky clutter. This could improve the CFAR detector performance. The larger shape parameter was largely contributed to the noise (small

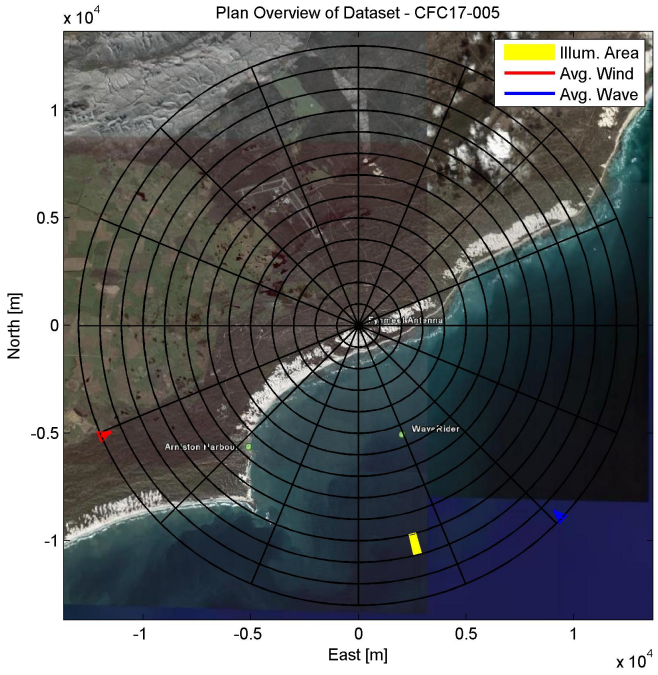

Fig. 4.6. Geographical overview for the far clutter measurement setup [CSIR].

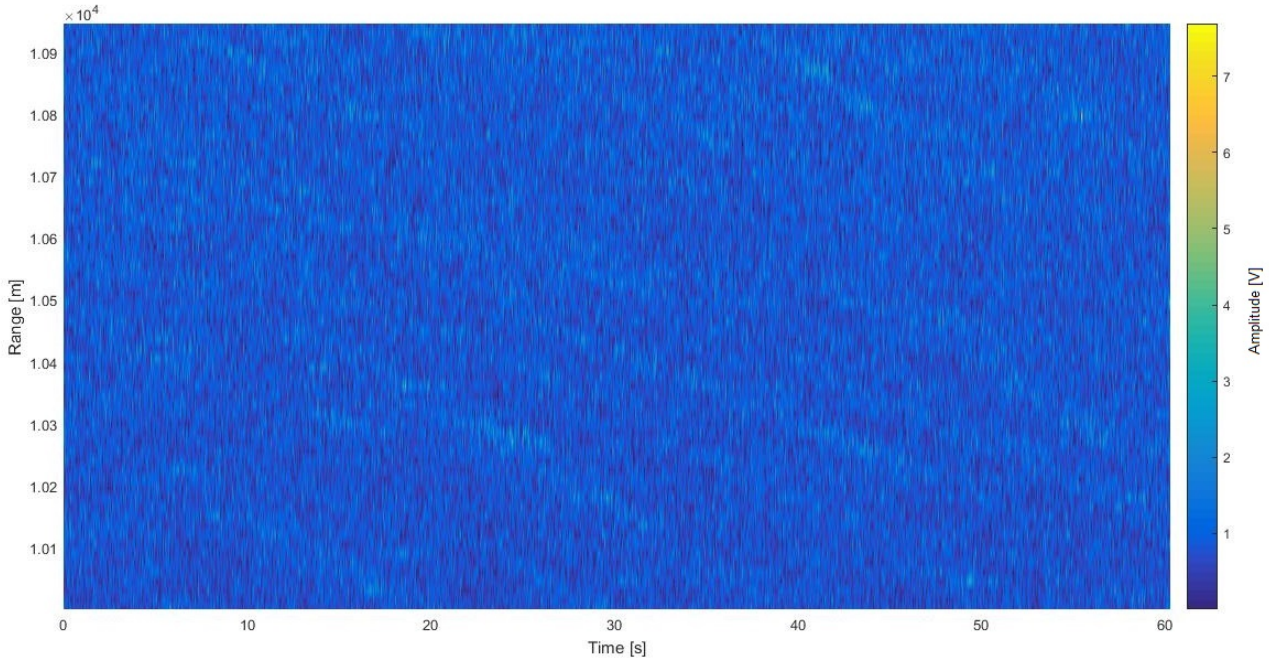

Fig. 4.7. Far clutter amplitude data for all the pulses over the range extend.

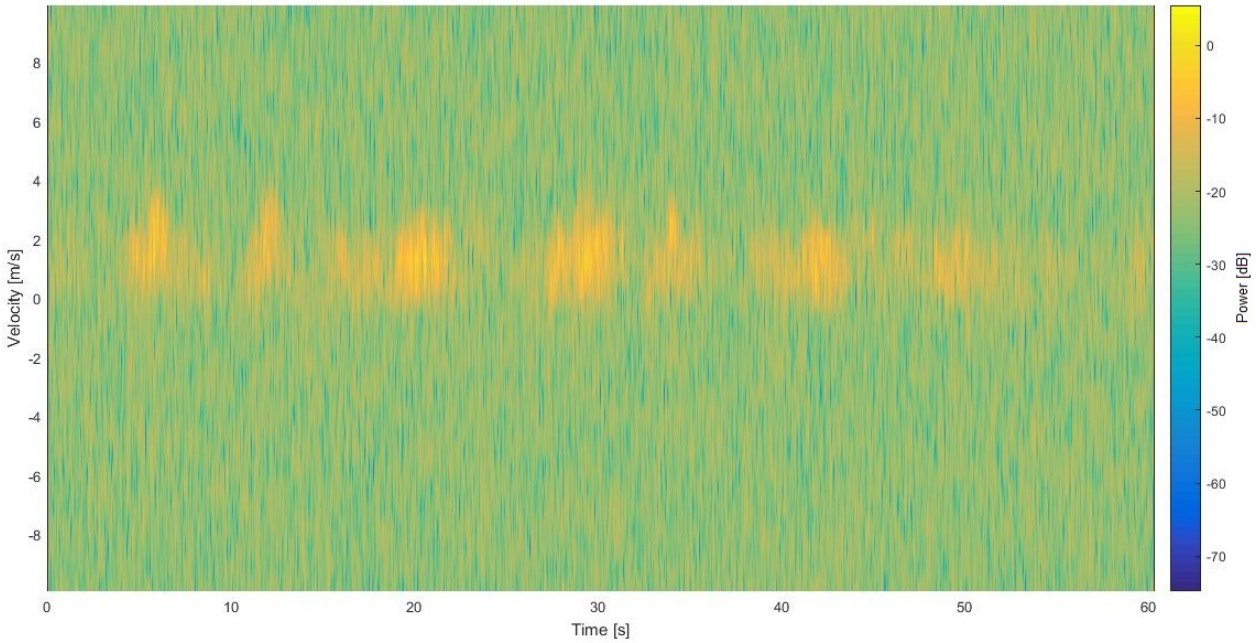

Fig. 4.8. Far clutter velocity spectrum (in dB).

CNR) and also the difference in grazing angle and clutter illuminated area. If the amplitude data was LP filtered to remove a considerable amount of the noise power, the shape parameter was then estimated to be 4 and the scale parameter 32.8 for an approximate fit as illustrated in Fig 4.10.

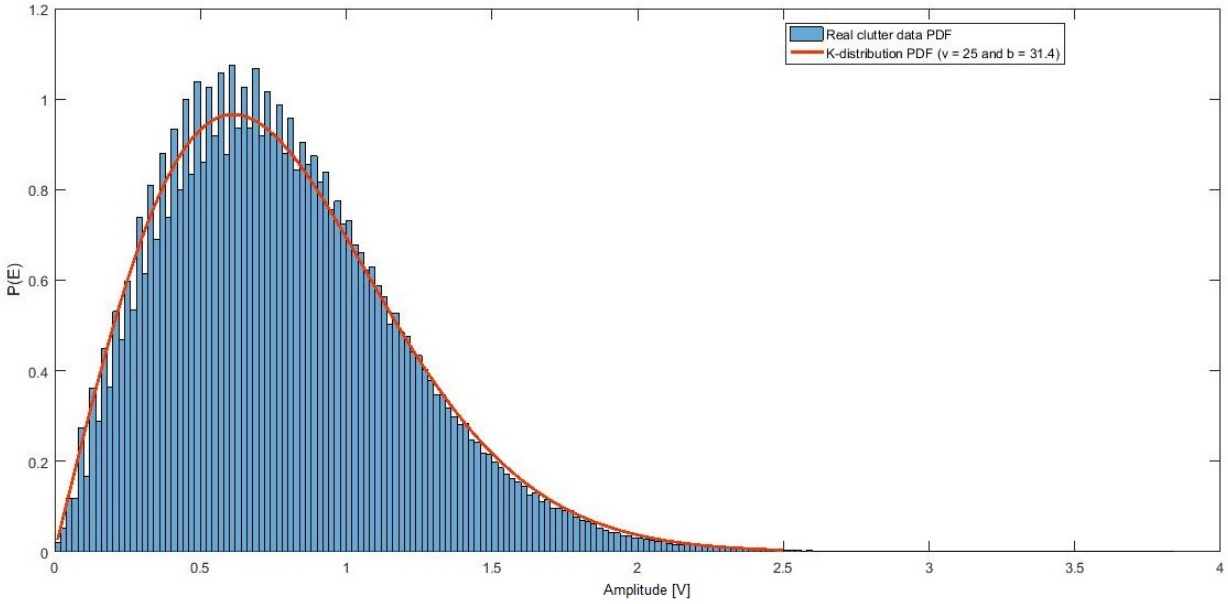

Fig. 4.9. Far clutter amplitude pdf and K-distribution.

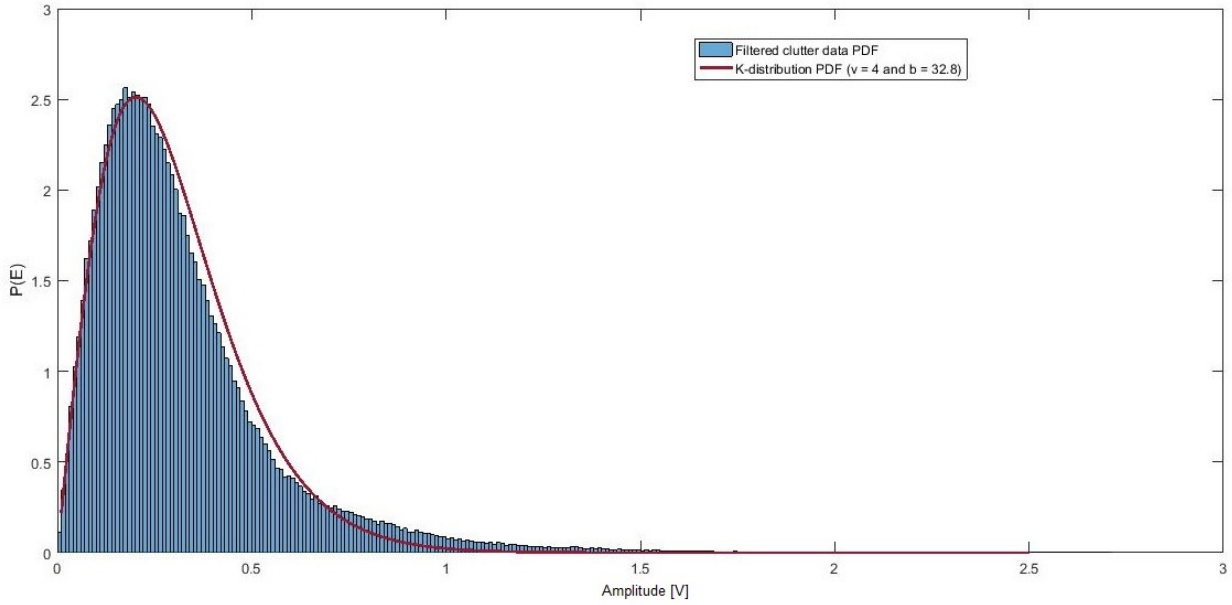

Fig. 4.10. Filtered far clutter amplitude pdf and K-distribution.

4.3 Simulations

This section covered different beamforming and scan pattern simulations to evaluate and compare performance. Two different simulations were developed. The simulations progressed from single axis non-azimuth scanning to dual axis azimuth scanning systems. Some constant inputs generally remained the same for all simulations. Table 4.4 shows some of the important inputs. The clutter suppression zone was up to $12\,m/s$, even though the clutter only spanned up to approximately $6\,m/s$, in order to also suppress some of the FFT sidelobes.

4.3.1 Scenarios

Both simulations used the target specifications as stipulated in Table 4.1. This included a SSM radially closing in on the radar at $333\,m/s$ and an UAV at $\leq 15\,m/s$.

4.3.2 Goal

The simulation model created, was used to determine if the detection performance specifications were realistic for both the low and high end threats of the multi-mission naval ship with a rotating maritime multi-beam electronically steered array surveillance radar. The goals of the simulations were to:

- Determine if a single axis beam stack with coherent air GOCA-CFAR channel processing,

Table 4.4. Inputs which are the same for all simulations.

Input	Value
Range resolution	$50\,m$
Range bin	$25\,m$
Amplification gain	$20\,dB$
Antenna position	$x = 0\,m$; $y = 0\,m$; $z = 20\,m$
Antenna velocity	$V_x = 0\,m/s$; $V_y = 0\,m/s$; $V_z = 0\,m/s$
Antenna rotation	$30\,rpm$
Rotation sector	0° to 180°
Frequency	$9\,GHz$
Elements	10 rows ($d_v = \lambda/2$); 30 per row ($d_h = \lambda/2$)
Minimum azimuth beamwidth	3.4°
Minimum elevation beamwidth	10.2°
Receiver noise	$B = 180\,MHz$; $F = 0\,dB$; $T = 290\,K$
SSM position	$x = 0\,m$; $y = 23000\,m$; $z = 10\,m$
SSM velocity	$V_x = 0\,m/s$; $V_y = -333\,m/s$; $V_z = 0\,m/s$
SSM RCS	$0.1\,m^2$ (SW 0)
SSM size	1 range bin
UAV position	$x = 0m$; $y = 19000\,m$ to $7000\,m$; $z = 10\,m$
UAV velocity	$V_x = 0\,m/s$; $V_y = -15$ to $15\,m/s$; $V_z = 0\,m/s$
Sea state	3
UAV RCS	$0.05\,m^2$ (SW 0)
UAV size	1 range bin
Clutter transfer range	$10000\,m$
Clutter suppression	$\leq 12\,m/s$

interleaved with short burst non-coherent CA-CFAR or constant threshold surface channel processing can meet the pre-determined specifications

- Determine if a dual axis beam stack with long dwell coherent GOCA-CFAR air and surface channel processing can meet the pre-determined specifications
- Compare the single and dual axis air and surface channel detection performances.

4.3.3 Simulation 1 - single axis setup

This simulation entailed a single axis receive beam stack fixed on a zero degree azimuth (no azimuth scanning). Coherent Doppler processing for the air channel with GOCA-CFAR detection was interleaved with the surface channel NCPIs. NCPIs were used for the surface channel as there were not enough pulses for Doppler processing. Both CA-CFAR and constant

threshold detection were evaluated for the surface channel.

Phased array radars that use this type of beamforming and scan pattern are systems that typically have an analog passive transmit system with phase shifters at subarray level. This allows a wide transmit beam to be shaped at a zero azimuth angle, but no azimuth scanning is possible. The receive system typically can be a subarray digital array with no phase shifters at element level. The digital beamforming at subarray level allows multiple beams to be formed in elevation. Some important simulation inputs and independent variables are shown in Table 4.5. Dwell time, PRF and pulse amounts were values produced by the simulation model based on the processing sectors and beamforming capabilities of the radar.

4.3.4 Simulation 2 - dual axis setup

This simulation entailed a dual axis multi-receive beam stack for both the air and surface channel with azimuth scanning. Coherent Doppler processing was implemented for the air and surface channels with GOCA-CFAR detection. The air channel was implemented in a rotation sector division with a scan rate of $90°/s$ and a rotation rate of $180°/s$. This implied that when the radar had rotated at a ship relative angle from 0° to 60° the radar would have scanned from 0° to 90°. The surface channel was implemented in a rotation sector division as the radar rotated between 60° and 120° with no scanning to maximise the dwell time. The air channel was again implemented in a rotation sector division as the radar rotated from 120° to 180° and the sector 90° to 180° was scanned. Through this scan pattern, the complete sector was scanned with the priority air channel on every rotation. The pattern could be altered on every rotation to shift the surface sector to complete surface surveillance after every 3 rotations, which should be sufficient as the slow-moving targets did not require a high update rate.

Phased array systems that will use this type of beamforming and scan pattern are element digital arrays. These allow a wide transmit beam to be shaped and scanned in azimuth and elevation. The digital beamforming on receive at element level allows multiple beams to be formed and scanned in elevation and azimuth. Some important simulation inputs and independent variables per rotation sector division are shown in Table 4.6 to 4.8.

4.3.5 Simulation 1 - single axis results

The clutter-free air channel GOCA-CFAR threshold constant was determined using the non-rotating Monte Carlo simulation, as explained in subsection 3.1.9, where multiple threshold constants were tested. This provided the associated P_{fa}. From this data, an appropriate threshold constant that provided the required P_{fa} of 1×10^{-5} was then selected. Fig 4.11 is the simulation result plot of the false alarm probability against the threshold constant. Also plotted is the calculated value as determined by equation 2.28. There was a good correlation

Table 4.5. Inputs and independent variables for simulation 1.

Input	Value
Rotation sector division 1 (0° to 180°)	
Scan rate	$0°/s$
M-of-n	2-of-3
Proc. intervs. per beamwidth	3
Air channel	
CPI dwell time	$4.9\,ms$
Unambiguous PRFs	$PRF_1 = 9.6\,kHz$; $PRF_2 = 8.8\,kHz$; $PRF_3 = 8.0\,kHz$
Pulses	$PRF_1 = 47$; $PRF_2 = 43$; $PRF_3 = 39$
Receive beams	$beam_n = [az°\ el°]$; $beam_1 = [0°\ 0°]$; $beam_2 = [0°\ 5°]$; $beam_3 = [0°\ 10°]$; $beam_4 = [0°\ 15°]$; $beam_5 = [0°\ 20°]$; $beam_6 = [0°\ 25°]$; $beam_7 = [0°\ 30°]$; $beam_8 = [0°\ 35°]$; $beam_9 = [0°\ 40°]$; $beam_{10} = [0°\ 45°]$
Sum beams	$sumbeam_1 = beam_1 + beam_2$; $sumbeam_2 = beam_2 + beam_3$; $sumbeam_3 = beam_3 + beam_4$; $sumbeam_4 = beam_4 + beam_5$; $sumbeam_5 = beam_5 + beam_6$; $sumbeam_6 = beam_6 + beam_7$; $sumbeam_7 = beam_7 + beam_8$; $sumbeam_8 = beam_8 + beam_9$; $sumbeam_9 = beam_9 + beam_{10}$
GOCA-CFAR	Guard cells (2D total) = 6; Reference cells (2D total) = 104
Surface channel	
NCPI dwell time	$1.4\,ms$
Unambiguous PRFs	$PRF_1 = 4.3\,kHz$; $PRF_2 = 4.3\,kHz$; $PRF_3 = 4.3\,kHz$
Unambiguous pulses	$PRF_1 = 6$; $PRF_2 = 6$; $PRF_3 = 6$
Receive beams	$beam_n = [az°\ el°]$; $beam_1 = [0°\ 0°]$; $beam_2 = [0°\ 5°]$; $beam_3 = [0°\ 10°]$
Sum beams	$Sumbeam_1 = beam_1 + beam_2$; $Sumbeam_2 = beam_2 + beam_3$
CA-CFAR	Guard cells (1D-range total) = 2; Reference cells (1D-range total) = 8

between the simulated and calculated values. However, the simulated curve started to deviate from the calculated curve at P_{fa} of approximately lower than 1×10^{-5}, because only 1.06×10^5 range-Doppler cells were tested per simulation. Fig 4.12 is the probability of false alarm error between the simulated and calculated values. The error grew larger for threshold constants above 12. The selected GOCA-CFAR threshold constant was 12 (with 6 guard cells and 104 reference cells). The amount of reference cells could be varied, but a new threshold constant would then have to be determined through simulation for the required P_{fa} and P_d.

The desired peak power input was determined, with the threshold constant as determined

Table 4.6. Inputs and independent variables for simulation 2, rotation sector division 1.

Input	Value
Rotation sector	0° to 60°
Scan rate	$90°/s$
M-of-n	2-of-3
Proc. intervs. per beamwidth	1.55
Air channel	
CPI dwell time	$8.1\,ms$
Unambiguous PRFs	$PRF_1 = 8.5\,kHz$; $PRF_2 = 7.0\,kHz$; $PRF_3 = 5.5\,kHz$
Unambiguous pulses	$PRF_1 = 69$; $PRF_2 = 57$; $PRF_3 = 45$
Receive beams	$beam_n = [az° \; el°]$; $beam_1 = [-1.7° \; 0°]$; $beam_2 = [0° \; 0°]$; $beam_3 = [1.7° \; 0°]$; $beam_4 = [-1.7° \; 5°]$; $beam_5 = [0° \; 5°]$; $beam_6 = [1.7° \; 5°]$;...$beam_{28} = [-1.7° \; 45°]$; $beam_{29} = [0° \; 45°]$; $beam_{30} = [1.7° \; 45°]$
Sum beams	$sumbeam_1 = beam_1 + beam_2 + beam_3 + beam_4 + beam_5 + beam_6$; $sumbeam_2 = beam_4 + beam_5 + beam_6 + beam_7 + beam_8 + beam_9$; ... $sumbeam_9 = beam_{25} + beam_{26} + beam_{27} + beam_{28} + beam_{29} + beam_{30}$
Clutter beams	$beam_1$; $beam_2$; $beam_3$
GOCA-CFAR	Guard cells (2D total) = 6; Reference cells (2D total) = 104

above, through a non-rotating Monte Carlo simulation where multiple transmit powers were tested in the air channel with the SSM at the specified range ($23\,km$). The resulting detection probabilities were then used to determine the appropriate peak power that would provide the required P_d of 0.9. Fig 4.13 is the simulation result plot of P_d against the transmit power. The selected transmit power was $21\,W$ (prior to amplification gain).

The simulated detection performance was determined using single CPIs. However, final detection was performed based on the results of several CPIs (m-of-n detection). This adjusted the P_d according to the cumulative probability [23]:

$$P_c = \sum_{r=M}^{N} \binom{N}{r} P^r (1-P)^{N-r} \tag{4.1}$$

where M were the successes in N trials and P the single trial probability. From equation 4.1 it

Table 4.7. Inputs and independent variables for simulation 2, rotation sector division 2.

Input	Value
Rotation sector	60° to 120°
Scan rate	$0°/s$
M-of-n	2-of-3
Proc. intervs. per beamwidth	0.87
Surface channel	
CPI dwell time	$21.7\,ms$
Unambiguous PRFs	$PRF_1 = 4.8\,kHz$; $PRF_2 = 4.8\,kHz$; $PRF_3 = 4.8\,kHz$
Unambiguous pulses	$PRF_1 = 105$; $PRF_2 = 105$; $PRF_3 = 105$
Receive beams	$beam_n = [az°\ el°]$; $beam_1 = [-4.25°\ 0°]$; $beam_2 = [-2.55°\ 0°]$; $beam_3 = [-0.85°\ 0°]$; $beam_4 = [0.85°\ 0°]$; $beam_5 = [2.55°\ 0°]$; $beam_6 = [4.25°\ 0°]$; $beam_7 = [-4.25°\ 5°]$; $beam_8 = [-2.55°\ 5°]$; $beam_9 = [-0.85°\ 5°]$; $beam_{10} = [0.85°\ 5°]$; $beam_{11} = [2.55°\ 5°]$; $beam_{12} = [4.25°\ 5°]$....$beam_{18} = [4.25°\ 15°]$
Sum beams	$sumbeam_1 = beam_1 + beam_2 + beam_3 + beam_4 + beam_5 + beam_6 + beam_7 + beam_8 + beam_9 + beam_{10} + beam_{11} + beam_{12}$; $sumbeam_2 = beam_7 + beam_8 + beam_9 + beam_{10} + beam_{11} + beam_{12} + beam_{13} + beam_{14} + beam_{15} + beam_{16} + beam_{17} + beam_{18}$
Clutter beams	$beam_1$; $beam_2$; $beam_3$; $beam_4$; $beam_5$; $beam_6$
GOCA-CFAR	Guard cells (2D total) = 6; Reference cells (2D total) = 36

was shown that for a single trail P_d of 0.9, the cumulative detection probability P_{dc} was 0.97. This was better than the required P_d.

The cumulative probability was also applicable to the P_{fa}. However, for the air channel, the m-of-n detection was integrated with ambiguity resolution. This implied that the range and Doppler multiples influenced the probability statistic especially if the single trial P_{fa} was high and the ambiguity resolution was only capable of resolving $N - 1$ targets (where N was the PRFs), resulting in ghost returns. The exact adjustment of the P_{fa} was not determined in this study. To ensure comparable results between simulations, a 2-of-3 detection integration was used for the air channel on all simulations. With this, it had to be remembered that the P_{fa} of 1×10^{-5} was not a completely accurate value, but would provide an indication of the cumulative probability for a low P_{fa} (where the cumulative false alarm probability P_{fac} was 3×10^{-10} according to equation 4.1).

Table 4.8. Inputs and independent variables for simulation 2, rotation sector division 3.

Input	Value
Rotation sector	120° to 180°
Scan rate	$90°/s$
M-of-n	2-of-3
Proc. intervs. per beamwidth	1.55
Air channel	
CPI dwell time	$8.1\,ms$
Unambiguous PRFs	$PRF_1 = 8.5\,kHz$; $PRF_2 = 7.0\,kHz$; $PRF_3 = 5.5\,kHz$
Unambiguous pulses	$PRF_1 = 69$; $PRF_2 = 57$; $PRF_3 = 45$
Receive beams	$beam_n = [az°\ el°]$; $beam_1 = [-31.7°\ 0°]$; $beam_2 = [-30°\ 0°]$; $beam_3 = [-28.3°\ 0°]$; $beam_4 = [-31.7°\ 5°]$; $beam_5 = [-30°\ 5°]$; $beam_6 = [-28.3°\ 5°]$;...$beam_{28} = [-31.7°\ 45°]$; $beam_{29} = [-30°\ 45°]$; $beam_{30} = [-28.3°\ 45°]$
Sum beams	$sumbeam_1 = beam_1 + beam_2 + beam_3 + beam_4 + beam_5 + beam_6$; $sumbeam_2 = beam_4 + beam_5 + beam_6 + beam_7 + beam_8 + beam_9$; ... $sumbeam_9 = beam_{25} + beam_{26} + beam_{27} + beam_{28} + beam_{29} + beam_{30}$
Clutter beams	$beam_1$; $beam_2$; $beam_3$
GOCA-CFAR	Guard cells (1D total) = 2; Reference cells (2D total) = 104

For the surface channel, the clutter was included. As described in subsection 3.1.6, the clutter RCS was calculated against the range bins from the input parameters of the simulation. This eventually determined the power adaptation to the clutter data that was inserted. Fig 4.14 is a plot of the RCS against the range bins at different grazing angles. It could be seen that the RCS increased linearly further away from the radar. A grazing angle of 0.25° was chosen as this would provide a challenging environment at the ranges that would be tested for the targets. The next elevation beam (at 5° elevation) that was clutter-free somewhat mitigated this, improving the SCR (the elevation beamwidth was calculated as 10.2°). For all the simulations, the next elevation beam elevation angle was kept constant to make it comparable. In reality, the next elevation beam (and other higher beams) was not completely clutter-free due to some mainlobe overlap with the clutter and sidelobe clutter interference.

For the non-coherent constant surface threshold detection, a non-rotating Monte Carlo simulation was used to determine the desired threshold and associated P_d and P_{fa}, with the

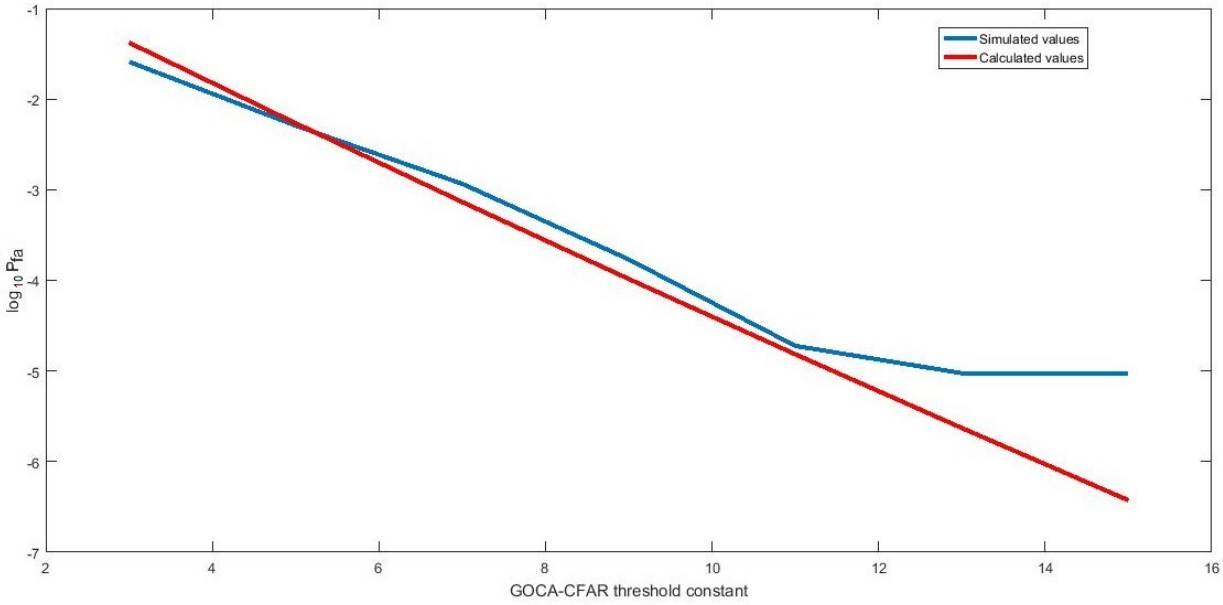

Fig. 4.11. Simulated and calculate false alarm probabilities against the GOCA-CFAR threshold constant.

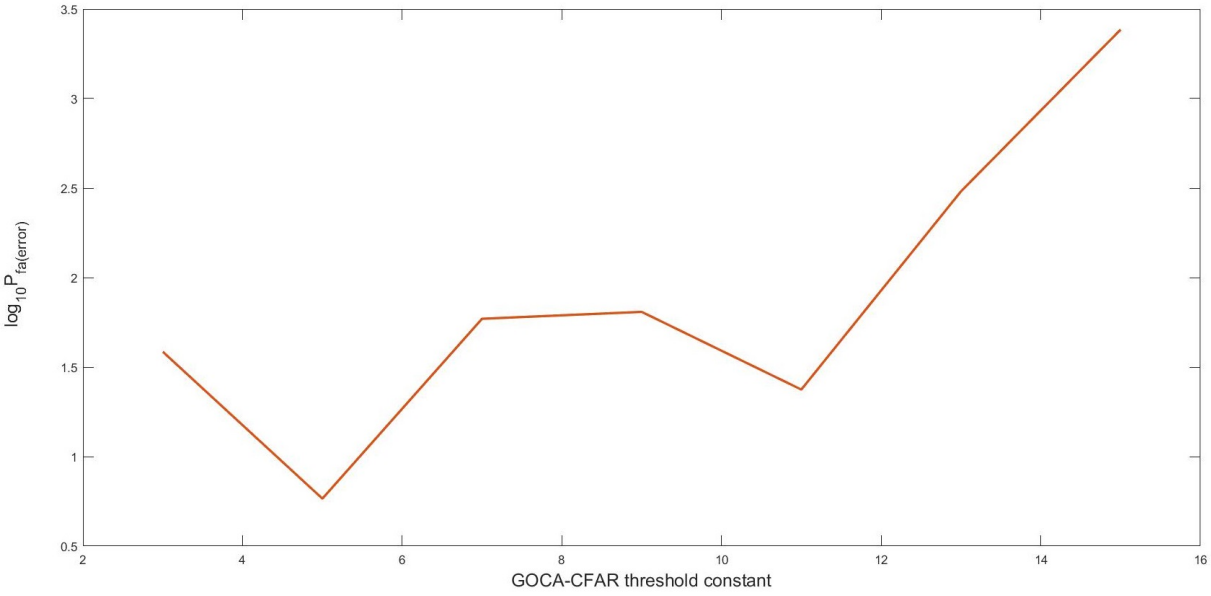

Fig. 4.12. Probability of false alarm error between simulated and calculated values against the GOCA-CFAR threshold constant.

selected transmit power as described in sub-section 3.1.9. Multiple thresholds were tested in the surface channel with the UAV at different ranges. Fig 4.15 (a) is a plot of the P_d against the threshold for the target at various ranges. As expected, the P_d plot would not vary much between the different ranges because of the time-varying gain that was used, which should keep

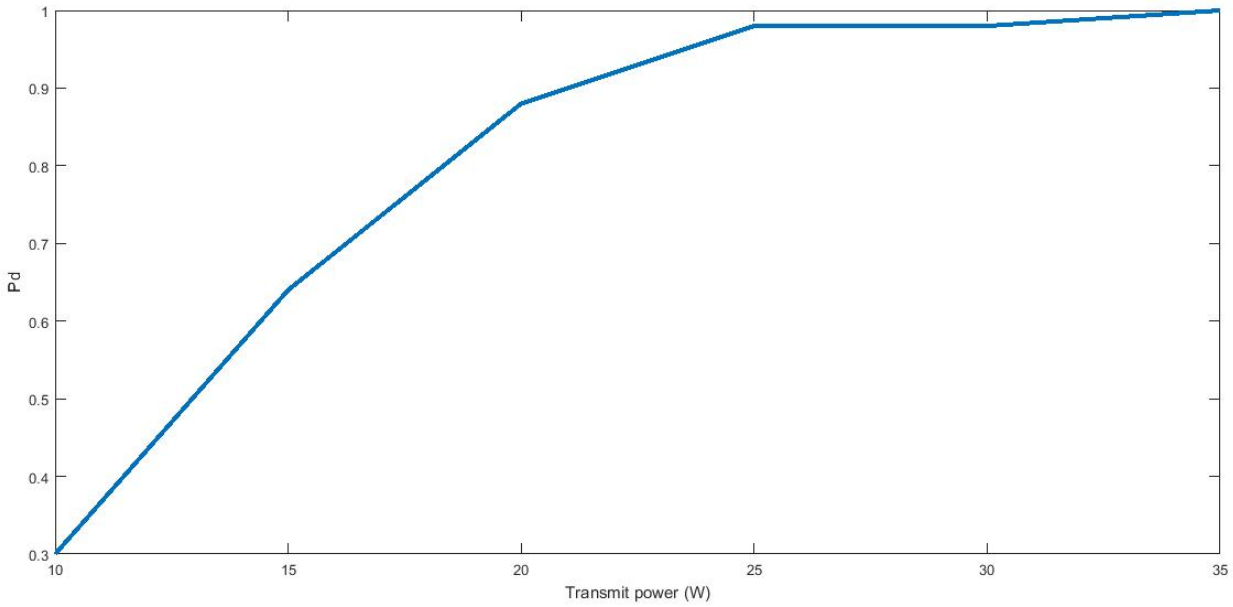

Fig. 4.13. Simulated detection probability against the transmit power.

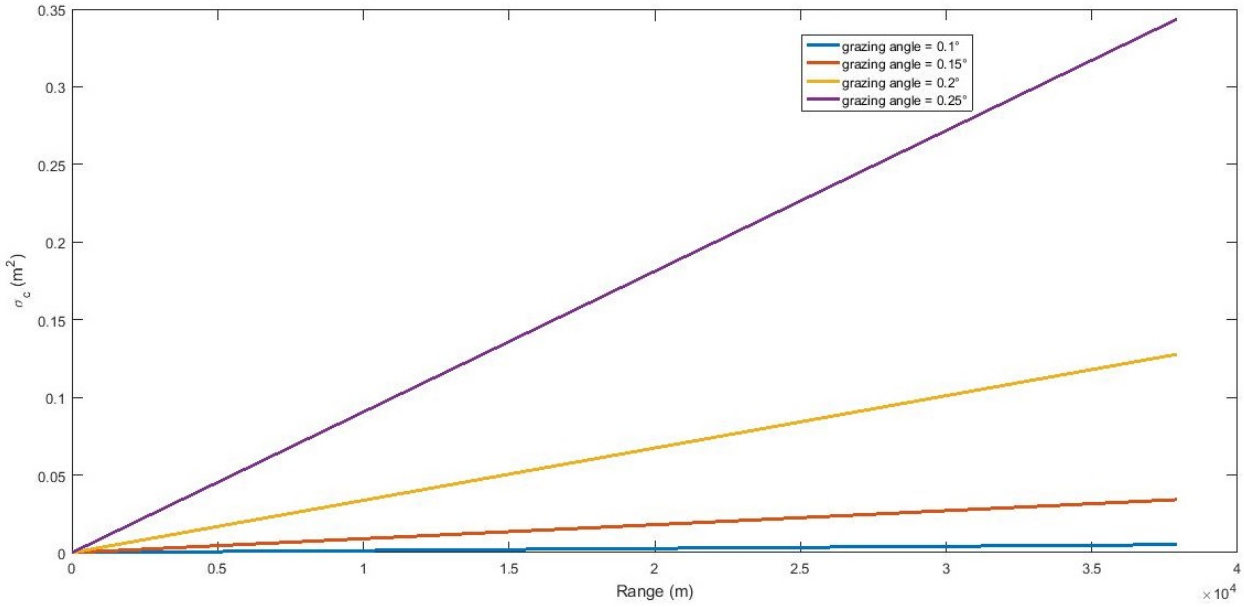

Fig. 4.14. Clutter RCS over range at different grazing angles.

the target return power constant. At high threshold values the P_d seemed to increase as the range increased. This was due to the larger clutter RCS that could provide positive detections in the target bin. Fig 4.15 (b) is a plot of the P_{fa} against the threshold for the bins surrounding the target at various ranges. It could be seen that the P_{fa} would increase across the threshold values as the range increased. This was due to the increase of the clutter RCS. A threshold of $3 \times 10^{-8}\,V$ was selected as the non-coherent constant surface threshold to be used. At $19000\,m$

the $P_d = 0.92$ and $P_{fa} = 0.14$. At $7000\,m$ the $P_d = 0.86$ and $P_{fa} = 5 \times 10^{-3}$.

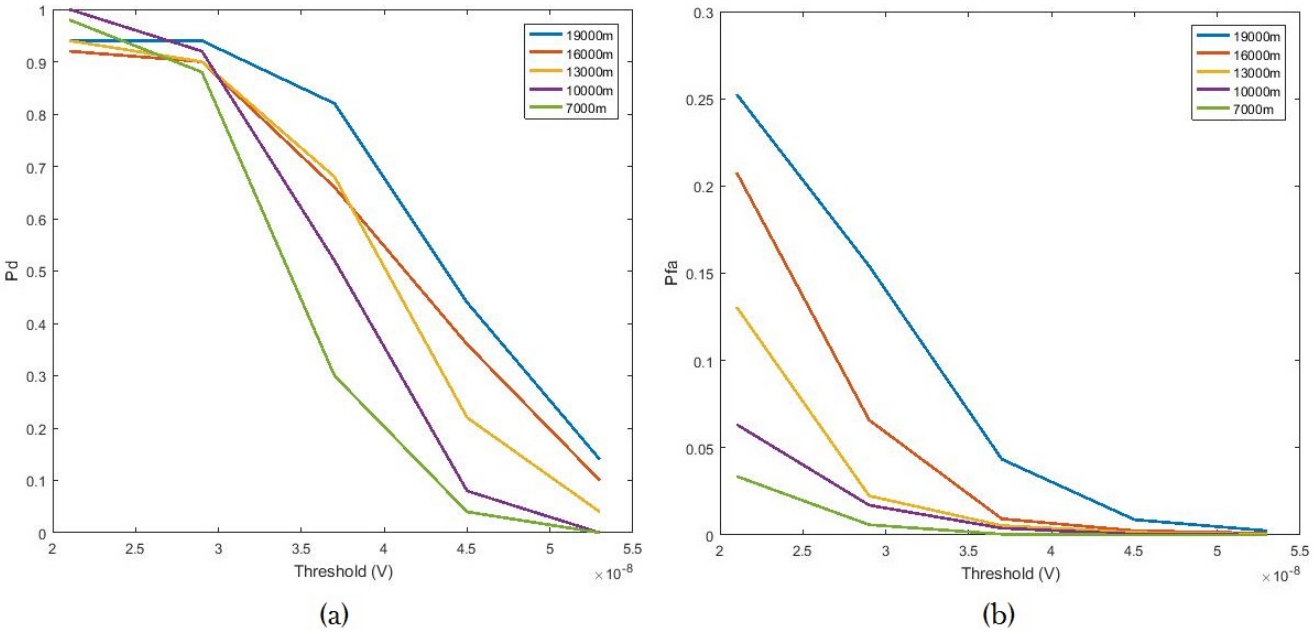

Fig. 4.15. Surface channel P_d and P_{fa} against threshold for different target ranges: (a) P_d against threshold for different target ranges; and (b) P_{fa} against threshold for different target ranges.

The cumulative probability was also applicable to the surface channel due to m-of-n detection. Equation 4.1 should provide reliable results to adjust the P_d and P_{fa}. This would adjust Pd and P_{fa} at $19000\,m$ to $P_{dc} = 0.98$ and $P_{fac} = 0.05$. At $7000\,m$ Pd and P_{fa} was adjusted to $P_{dc} = 0.95$ and $P_{fac} = 7.5 \times 10^{-5}$.

The radar simulation model was then used to test the SSM at 23km and the UAV at 19km and 7km. This was done with 5 scans at each range. The clutter data was offset with 2s after each scan in order to ensure variation in the clutter data per range. The surface channel was tested with the selected constant threshold ($3 \times 10^{-8}\,V$) and a CA-CFAR threshold of 2 different constants. The sector and range to process were selected to include 4 air channel CPIs and 4 surface channel NCPIs with 41 range bins.

Firstly, it was important to note that the MATLAB phased array toolbox applied a fractional delay linear interpolation filter with the target return signal. This weighed the target return signal amplitude per range bin over which the return signal overlapped. If the return signal for example started somewhere between two range bins, the fractional delay would be determined and a weighted amplitude would be allocated for the return signal at the first bin. The maximum amplitude would be allocated if the return signal covers both bins. For the simulation, the range resolution was set at $50\,m$ and the range bins size at $25\,m$. A maximum amplitude target signal peak return was obtained at the initial range bin, if the return signal started exactly at the

range bin and was then matched filtered. Throughout all simulations, the target position was selected such that it would start at a specific range bin when the beam scans over the target in order to make results comparable. The lower amplitude return for fractional delay interpolation and consequent matched filtering of target signals starting between range bins, could be compensated for by increasing transmit power in order to maintain P_d.

Another important underlying feature to note was the straddle loss of the FFT. If the target radial velocity was between 2 velocity Doppler bins, the amplitude would be shared between the 2 bins. A maximum amplitude would be obtained if a target had a velocity equal to a velocity Doppler bin. Throughout all simulations the target velocity was adjusted so that it would exactly correspond to the closest specific Doppler bin in order to make results comparable. The lower amplitude return for scalloping loss could be compensated for by increasing transmit power in order to maintain P_d.

Table 4.9 is a summary of the detection results for the first sum beam. It could be seen that for the SSM, the air channel simulation performed the best with similar to the predicted values with $P_{dc} = 1$ and $P_{fac} = 0$. The air channel complied to the SSM system specifications. Fig 4.16 (a) is an illustration of a single unambiguous CPI power spectrum return over the selected range to process for the air channel with the apparent target position and GOCA-CFAR threshold indicated. The SSM performance was not tested at different ranges as the folded clutter was suppressed and results were expected to be similar throughout all ranges. For the surface channel, the constant threshold did not comply to the false alarm specification for the SSM. Fig 4.16 (b) is an illustration of the return signal amplitude for a NCPI with constant threshold detection over the complete range. This figure showed that at higher ranges, the constant threshold would result in multiple false detections. A higher constant threshold could provide better results at this range for the SSM. However, the threshold was selected based on the UAV at lower ranges. The CA-CFAR threshold constant of 2 delivered the best results for for the surface channel for the SSM, but did not comply to the false alarm specification.

For the UAV at the tested ranges, the air channel did not detect the target within the clutter suppression zone. In the surface channel at the tested ranges, the predicted P_{dc} and P_{fac} for the constant thresholds were similar to that of the simulated values. A higher than predicted P_{fac} at $19km$ was due to the clutter decorrelation time being longer than the CPI duration and 4 NCPIs were used per scan with 2-of-3 detection integration. Each range bin that detected a false alarm contributed to the P_{fac} calculation. Ideally, only 3 NCPIs with 2-of-3 detection integration would provide a more accurate reflection of the P_{fac} performance. However, a CPI or NCPI did not always start exactly when the beam edge starts scanning over the target. Therefore, 4 CPIs or NCPIs were included in all simulations to ensure that no intervals with target returns were missed. This also implied that for these CPIs and NCPIs, that did not include target returns on all pulses, the target integration was not optimal. This was not compensated for in the simulation as only 2 detections were required. The loss for this integration could be compensated for by increasing the transmit power. Although, this would only provide

significant improvement in SNR, as the clutter will always be present and there would be no gain in SCR.

At $19km$ where the clutter RCS was large (small SCR) but less spiky the constant threshold and low CA-CFAR constant detectors both had a high P_{fac} and did not comply to the UAV false alarm specification. The higher CA-CFAR constant detector performed the best with $P_{dc} = 1$ and $P_{fac} = 0.03$ and complied with the UAV system specifications. This is illustrated in Fig 4.17 (a) and 4.18 (a).

At $7km$ where the clutter RCS was low (larger SCR than at far ranges) but more spiky the CA-CFAR detectors had the highest P_{fac}. The constant threshold detector performed the best if the target amplitude was well above that of the clutter and noise with $P_{dc} = 1$ and $P_{fac} = 0$, and complied with the UAV system specifications. This is illustrated in Fig 4.17 (b) and 4.18 (b).

Table 4.9. Simulation 1: Results for 5 scans. Specified SSM performance: $P_d \geq 0.9$, $P_{fa} \leq 1 \times 10^{-5}$. Specified UAV performance: $P_d \geq 0.9$, $P_{fa} \leq 0.06$. 'C' = comply. 'NC' = non-comply.

Channel	Predicted		Simulated		Specified	
	P_{dc}	P_{fac}	P_{dc}	P_{fac}	P_d	P_{fa}
SSM at $23km$						
Air (Doppler GOCA-CFAR const. = 12)	0.97	3×10^{-10}	1	0	C	C
Surface (constant threshold = 3×10^{-8})	-	-	1	0.21	C	NC
Surface (CA-CFAR constant = 1)	-	-	1	0.14	C	NC
Surface (CA-CFAR constant = 2)	-	-	1	0.02	C	NC
UAV at $19km$						
Air (Doppler GOCA-CFAR const. = 12)	0	3×10^{-10}	0	0	NC	NC
Surface (constant threshold = 3×10^{-8})	0.98	0.05	1	0.13	C	NC
Surface (CA-CFAR constant = 1)	-	-	1	0.17	C	NC
Surface (CA-CFAR constant = 2)	-	-	1	0.03	C	C
UAV at $7km$						
Air (Doppler GOCA-CFAR const. = 12)	0	3×10^{-10}	0	0	NC	NC
Surface (constant threshold = 3×10^{-8})	0.95	7.5×10^{-5}	1	0	C	C
Surface (CA-CFAR constant = 1)	-	-	1	0.12	C	NC
Surface (CA-CFAR constant = 2)	-	-	1	0.1	C	C

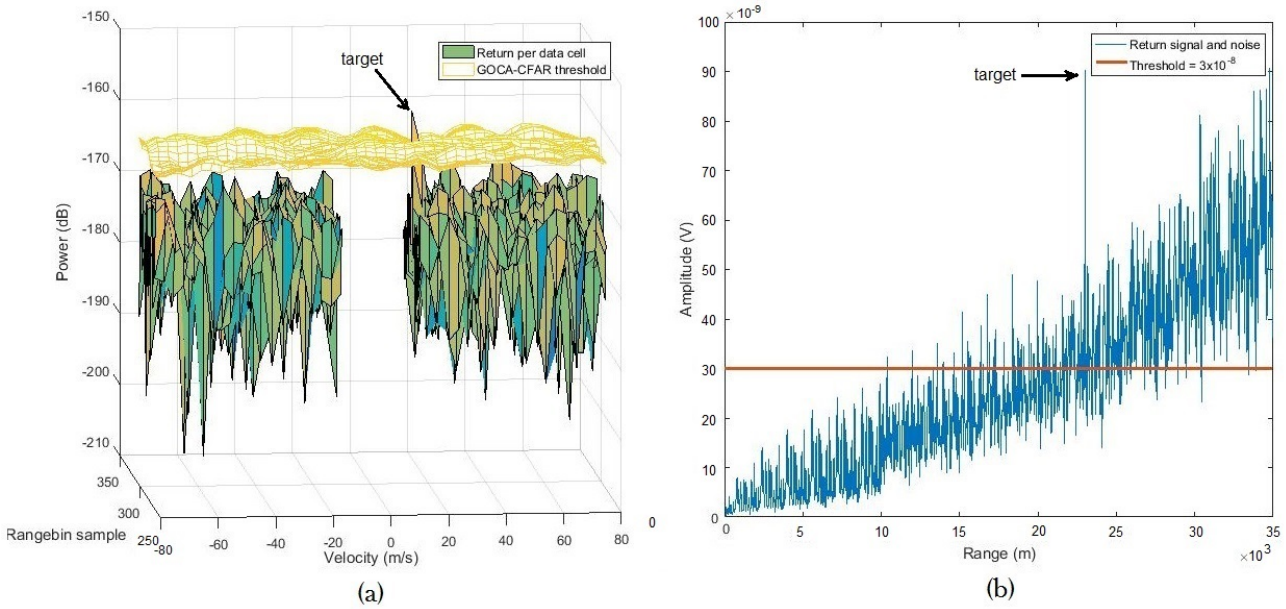

Fig. 4.16. SSM air and surface channel returns at 23 km simulation 1: (a) air channel single unambiguous CPI power spectrum return over selected range bins with the apparent target position and GOCA-CFAR threshold indicated; and (b) surface channel single NCPI amplitude return over the complete range with the target position and constant thresholds indicated.

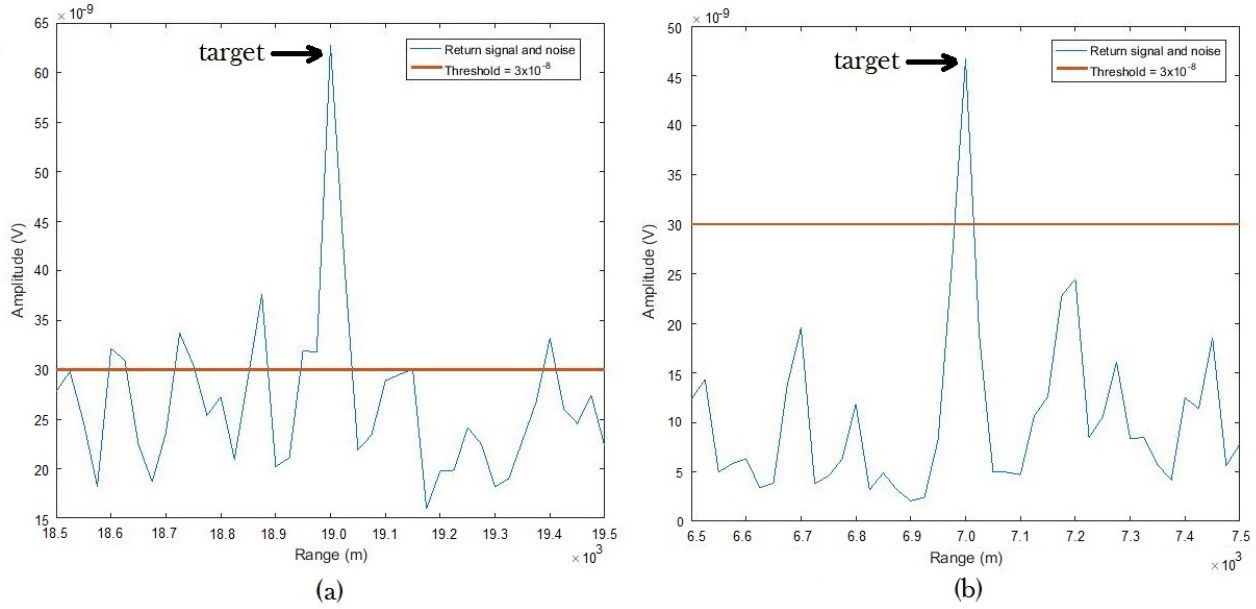

Fig. 4.17. UAV surface channel returns with constant thresholds over various ranges, simulation 1: (a) target at 19 km NCPI amplitude return over selected range bins with the target position and constant thresholds indicated; and (b) target at 7 km NCPI amplitude return over selected range bins with the target position and constant thresholds indicated.

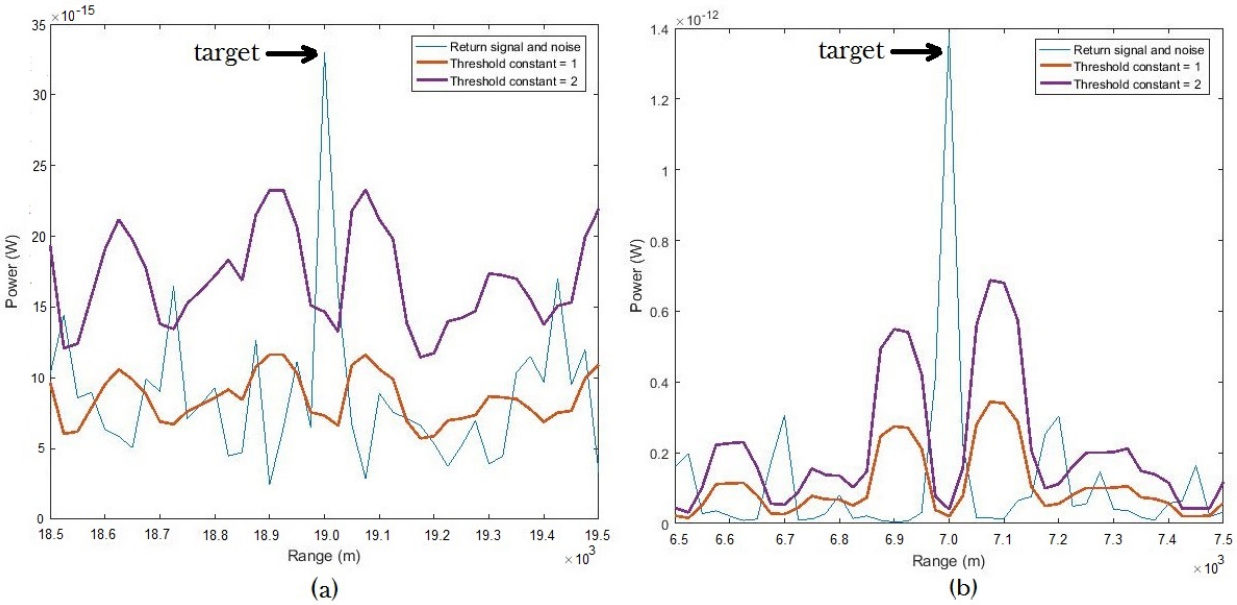

Fig. 4.18. UAV surface channel returns over various ranges simulation 1: (a) target at 19 km NCPI power return over selected range bins with the target position and CA-CFAR thresholds indicated; and (b) target at 7 km NCPI power return over selected range bins with the target position and CA-CFAR thresholds indicated.

4.3.6 Simulation 2 - dual axis results

The clutter-free air channel GOCA-CFAR threshold constant was determined using a non-rotating Monte Carlo simulation where multiple threshold constant were tested. A GOCA-CFAR threshold constant of 12 was selected to provide the required P_{fa} of 1×10^{-5}. This was the same value as for simulation 1 - which agreed with equation 2.28 that the P_{fa} was only a function of the threshold constant and number of reference cells.

The desired peak power input was determined, with the threshold constant as determined above, through a non-rotating Monte Carlo simulation where multiple transmit powers were tested in the air channel with the SSM at the specified range ($23\,km$). A transmit power of $35\,W$ was selected to provide the P_d of 0.9. The required transmit power was higher than that required in simulation 1 because of the higher noise power due to the increased number of beams in the sum beam. When clutter was introduced, the addition of the sidelobes of the FFT from the multiple beams played a substantial role as well. The transmit power was increased to $45\,W$ for proper performance. As per simulation 1, m-of-n detection again improved the detection performance.

In order to determine if dwell time and Doppler resolution impacted the detection performance of the surface channel, a shorter dwell time was first evaluated with the same beam configuration as in rotation sector division 2 with a transmit power of $3\,5W$. The CPI dwell time was reduced from $21.7\,ms$ (105 pulses) to $6.3\,ms$ (30 pulses). With the UAV in a strong and spiky clutter environment, at a radial velocity of $18.5\,m/s$ (approaching the radar), after 5 scans and at clutter data offsets of $2\,s$, it was determined that $P_{dc} = 0.8$ and $P_{fac} = 0.18$. Fig 4.19 (a) is a single unambiguous CPI power spectrum return over the selected range to process with the UAV present. The GOCA-CFAR threshold (constant = 12) is also indicated with 104 reference cells used. Reducing the velocity of the UAV to $15.8\,m/s$ resulted in $P_{dc} = 0$ and $P_{fac} = 0.19$. Fig 4.19 (b) is an illustration of the single unambiguous CPI power spectrum return over the selected range to process with the UAV at the slower velocity. The target was now masked by the surrounding clutter and was below the threshold, hence the poor detection probability.

In order to reduce the masking effect, the reference cells were reduced to 36. The effect of reducing the reference cells on the P_{fa} on the homogeneous interference from equation 2.28 is illustrated in Fig 4.20 (a). Reducing the reference cells from 104 to 36 at a threshold constant of 12 (or less) had minimal effect on P_{fa}. Fig 4.20 (b) illustrates the effect on the P_d for a signal-to-interference-plus-noise ratio (SINR) of 6 as per equation 2.29. Reducing the reference cells from 104 to 36 at a threshold constant of 12 (or less) had minimal effect on P_d. It had to be noted that in areas of spiky clutter of the range-Doppler data set (non-homogeneous areas), a change in P_d, changed clutter false alarms and hence the P_{fa}.

With the GOCA-CFAR reference cells reduced to 36, the UAV in a strong and spiky clutter environment, at a radial velocity of $13.2\,m/s$, after 5 scans and at clutter data offsets of $2\,s$,

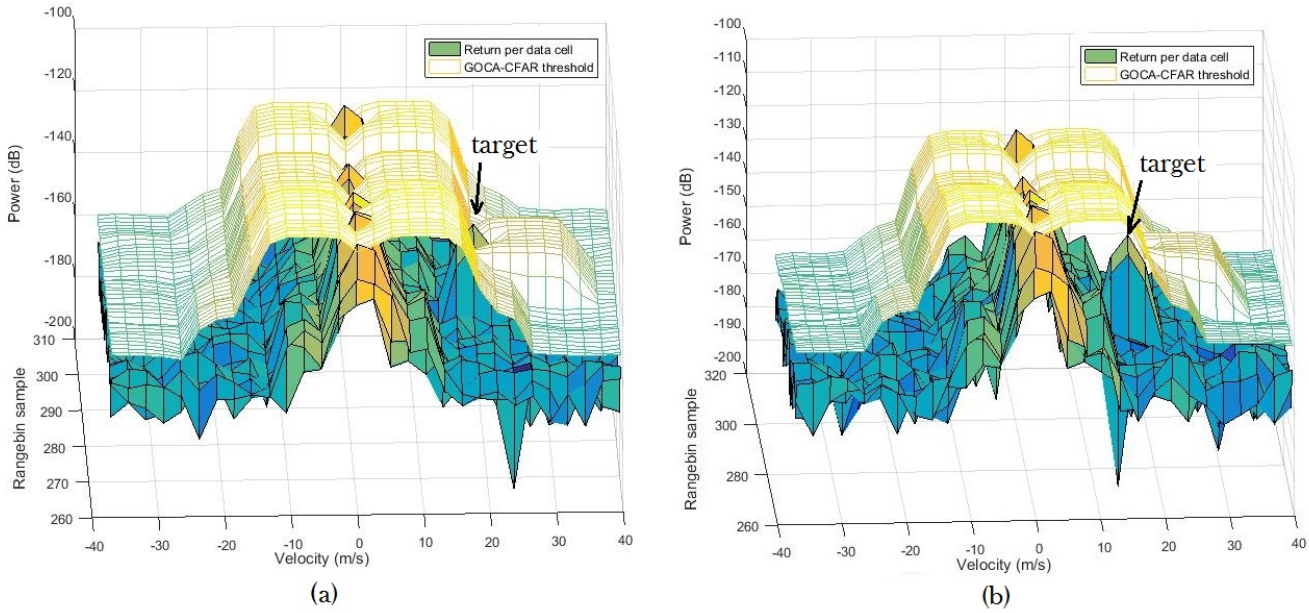

Fig. 4.19. Low Doppler resolution surface channel target return: (a) target in a strong and spiky clutter environment with unambiguous CPI power spectrum return over selected range bins with the UAV position and thresholds indicated (UAV velocity = 18.5 m/s; reference cells = 104); (b) target in a strong and spiky clutter environment with unambiguous CPI power spectrum return over selected range bins with the UAV position and thresholds indicated (UAV velocity = 15.8 m/s; reference cells = 104).

it was determined that $P_{dc} = 0.8$ and $P_{fac} = 0.19$. The target could be detected at lower velocities closer to the clutter Doppler structure. Fig 4.21 (a) is a single unambiguous CPI power spectrum return over the selected range to process with the UAV present. The GOCA-CFAR threshold is also indicated with 36 reference cells used. Reducing the velocity of the UAV to 10.6 m/s resulted in $P_{dc} = 0$ and $P_{fac} = 0.2$. Fig 4.21 (b) is an illustration of the single unambiguous CPI power spectrum return over the selected range to process with the UAV at the slower velocity. The target was now masked by the surrounding clutter and was below the threshold. Using less reference cells reduced the masking and allowed the target to be detected at lower velocities.

The longer CPI dwell time was then used, as specified in rotation sector division 2 in Table 4.8 (21.7 ms and 105 pulses). With the UAV in a strong and spiky clutter environment, at a radial velocity of 6.1 m/s (approaching the radar), after 5 scans and at clutter data offsets of 2 s, it was determined that $P_{dc} = 1$ and $P_{fac} = 0.06$. The target could be detected at much lower radial velocities with a high Doppler resolution than with a lower Doppler resolution. The false alarms were also considerably less than with a lower Doppler resolution as the clutter started

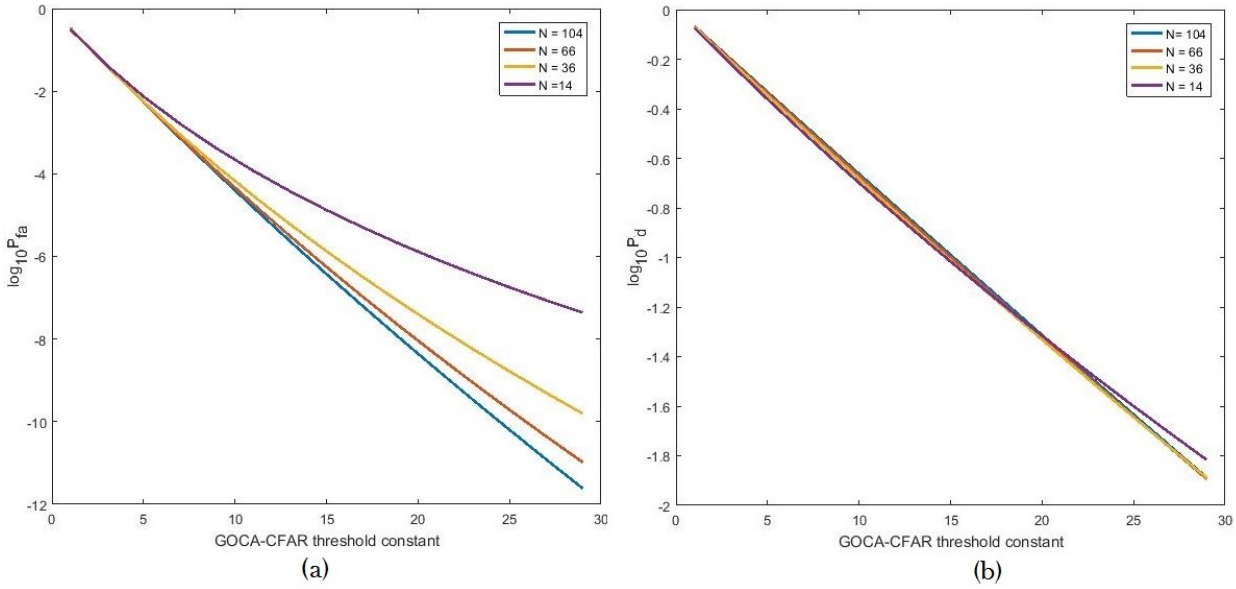

Fig. 4.20. Detection performance against threshold constant values with different threshold cell values.: (a) P_{fa} against the threshold at various reference cell values; (b) P_d against the threshold with SINR = 6 at various reference cell values.

forming a less spiky homogeneous environment. Fig 4.22 (a) is a single unambiguous CPI power spectrum return over the selected range to process with the UAV present. The GOCA-CFAR threshold (constant = 12) is also indicated with 36 reference cells used. Reducing the velocity of the UAV to $4.6m/s$ resulted in $P_{dc} = 0$ and $P_{fac} = 0.06$. Fig 4.22 (b) is an illustration of the single unambiguous CPI power spectrum return over the selected range to process with the UAV at the slower velocity. The target was now masked by the surrounding clutter and is below the threshold.

The radar simulation model was then used to test the SSM at $23\,km$ and the UAV at $19\,km$ and $7\,km$. This was done with 5 scans at each range. The clutter data was offset with $2\,s$ after each scan in order to ensure variation in the clutter data per range. The air channel was only tested for the SSM, as the clutter was suppressed and the UAV could not be detected. In the surface channel the detection performance was tested with the UAV at different velocities. And in some cases the threshold constant was also adjusted. The sector and range to process were selected to include 4 air channel CPIs and 4 surface channel CPIs with 41 range bins.

It had to be noted that for the surface channel, a much larger range-Doppler CPI dataset was used to determine detection performance than with simulation 1. In simulation 1 a 1D integrated range NCPI dataset was used to determine detection and false alarm data performance. For this study, the false alarms in simulation 2 for the surface channel, was determined only in the range dimension. In other words, a cumulative false detection in any

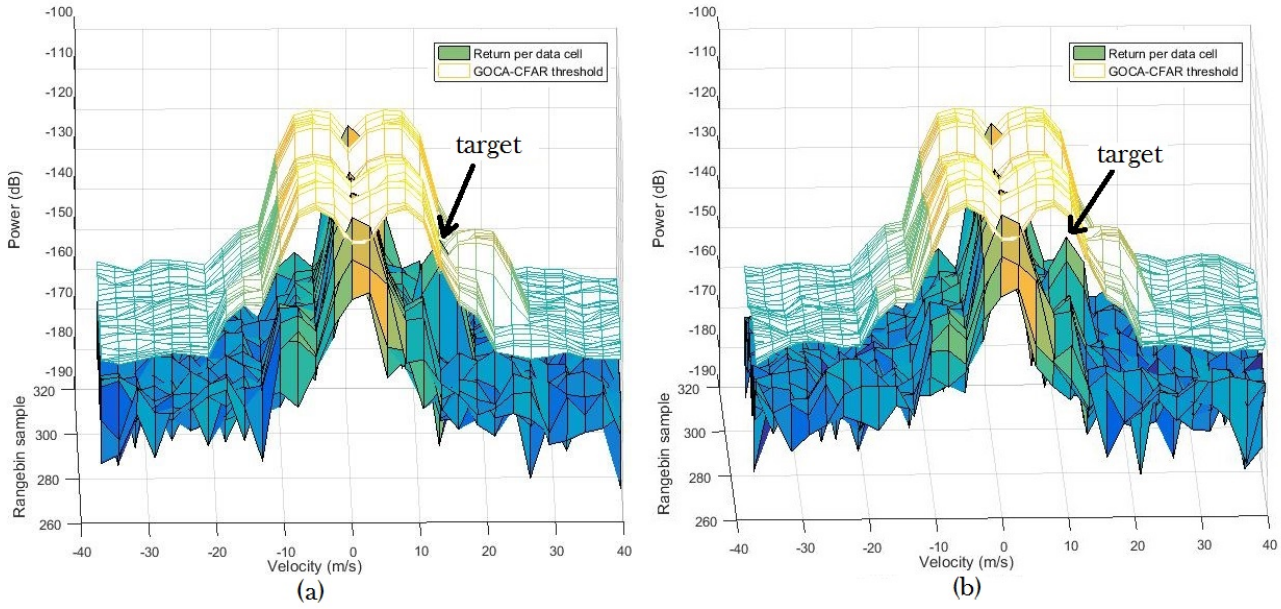

Fig. 4.21. Low Doppler resolution surface channel target returns with reduced reference cells: (a) target in a strong and spiky clutter environment with unambiguous CPI power spectrum return over selected range bins with the UAV position and thresholds indicated (UAV velocity = $13.2m/s$; reference cells = 36); (b) target in a strong and spiky clutter environment with unambiguous CPI power spectrum return over selected range bins with the UAV position and thresholds indicated (UAV velocity = $10.6m/s$; reference cells = 36).

Doppler bin would amount to a false alarm at that range bin, and the P_{fac} was determined over the range bins tested for the 5 scans. It was found that there are very few range bins in all the scans where more than one Doppler bin had cumulative false detections. This implied, that the P_{fac} values stated in the results for simulation 2 are in reality much lower, however it is done this way in order to make it comparable with simulation 1.

Table 4.10 is a summary of the detection results for the first sum beam. For the SSM, the air channel simulation performed better with an increased transmit power of $45\,W$, with $P_{dc} = 1$ and $P_{fac} = 0$. The air channel complied to the SSM system specifications. The increase in power increased the SINR, which was required due to the clutter FFT sidelobes addition from multiple beams. Fig 4.23 (a) is an illustration of a single unambiguous CPI power spectrum return over the selected range to process for the air channel with the apparent target position and GOCA-CFAR threshold (constant = 12) indicated. For the SSM in the surface channel, the detection performance was also good with a $P_{dc} = 1$ and $P_{fa} = 0.01$, although the velocity was not resolvable and it did not comply to the false alarm specification. Fig 4.23 (b) is an illustration of a single unambiguous CPI power spectrum return over the selected range to

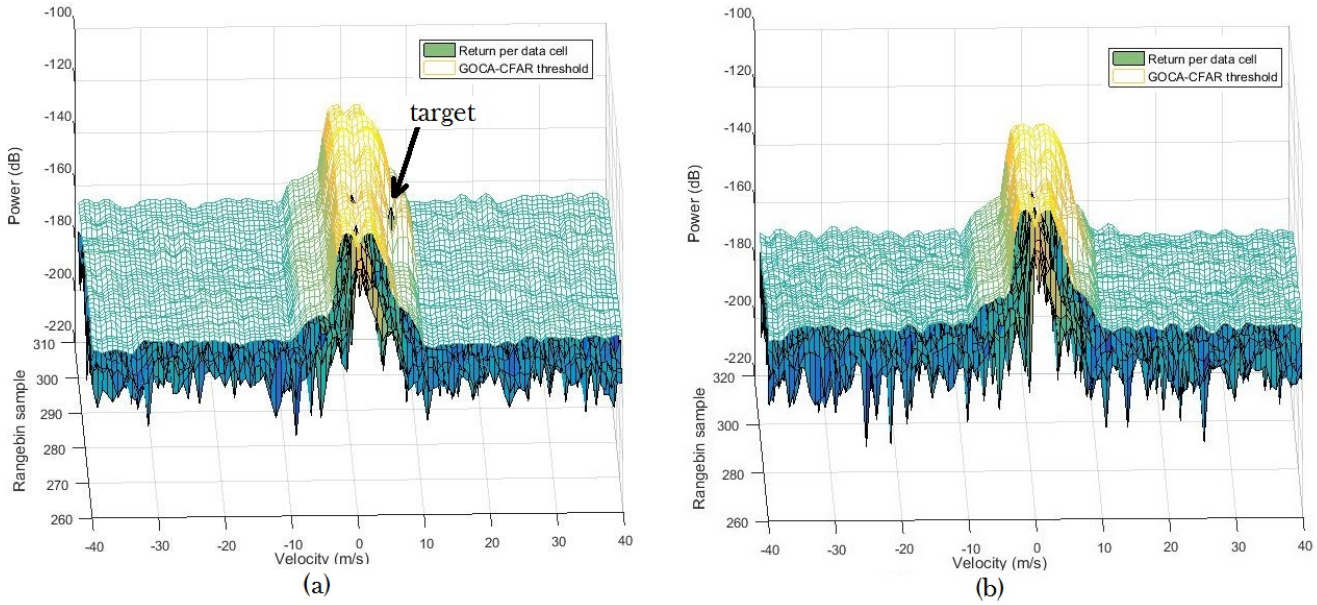

Fig. 4.22. High Doppler resolution surface channel target return: (a) target in a strong and spiky clutter environment with unambiguous CPI power spectrum return over selected range bins with the UAV position and thresholds indicated (UAV velocity = 6.1 m/s; reference cells = 36); (b) target in a strong and spiky clutter environment with unambiguous CPI power spectrum return over selected range bins with the UAV position and thresholds indicated (UAV velocity = 4.6 m/s; reference cells = 36).

process for the surface channel with the apparent target position and GOCA-CFAR threshold (constant = 12) indicated.

The UAV at 19 km was detected with a GOCA-CFAR threshold constant of 10 at a velocities of 9.2 m/s (and larger) towards and away from the radar, with $P_{dc} = 1$ and a low P_{fac}, which complied to the UAV system specifications. For slower velocities in between P_{dc} dropped considerably and it did not comply to UAV system detection specifications. The reason being the accumulation of the long dwell integrated clutter power at these velocities, which hid and masked the target return. At lower threshold constants that were tested for a UAV at 0 m/s, P_{dc} improved somewhat but P_{fac} increased. Fig 4.24 (a) is an illustration of a single unambiguous CPI power spectrum return over the selected range to process for the surface channel with the apparent target position at 19 km, velocity of 9.2 m/s and GOCA-CFAR threshold (constant = 10). As stated in subsection 4.2.1, the clutter at far ranges were less spiky and had a large RCS (small SCR) compared to the target. Also as stated before, the high Doppler resolution made the clutter more homogeneous as can be seen in Fig 4.24 (a). However, the clutter spectrum might be wider than what it would be in reality. This was due to the small CNR of

the clutter data used for the far range and LP filtering of the spectrum, which could include mostly noise between the clutter edge and filter cut off point. The data amplitude adjustment factor could allow this noise amplitude to be higher than the real noise floor especially since the RCS was large at far ranges. It was therefore possible that the target could be detected at lower velocities.

The UAV at $7\,km$ was detected within the UAV system specification with a GOCA-CFAR threshold constant of 10 at velocities of $5.4\,m/s$ (and larger) towards the radar and $3.8\,m/s$ (and larger) away from the radar, with $P_{dc} = 1$. P_{fac} was higher than at $19\,km$, due to the spiky and less homogeneous nature of the clutter as discussed in subsection 4.2.1. However, it was still reasonably low at 0.06 because the longer dwell time allowed for some degree of the homogeneous characteristic. For velocities in between these values the P_{dc} became zero. The accumulation of the long dwell integrated clutter power at these velocities hid and masked the target return. Fig 4.24 (b) is an illustration of a single unambiguous CPI power spectrum return over the selected range to process for the surface channel with the apparent target position at $7\,km$, velocity of $5.4\,m/s$ and GOCA-CFAR threshold (constant = 12). The target and clutter size RCS was of comparable size (larger SCR than at far ranges). Also, the spectrum was narrower than at $19\,km$, which could be due to the larger CNR of the data used at close ranges.

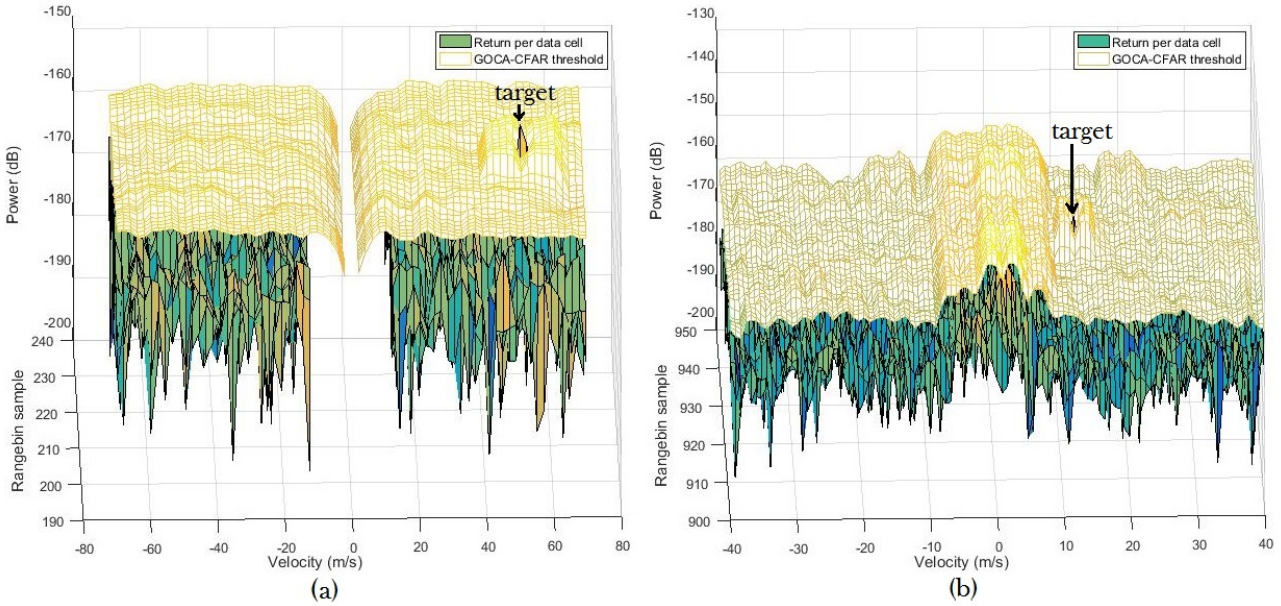

Fig. 4.23. SSM air and surface channel returns at $23\,km$ simulation 2: (a) air channel single unambiguous CPI power spectrum return over selected range bins with the apparent target position and GOCA-CFAR threshold indicated; and (b) surface channel single unambiguous CPI power spectrum return over selected range bins with the apparent target position and GOCA-CFAR threshold indicated.

Table 4.10. Simulation 2: Results for 5 scans. Specified SSM performance: $P_d \geq 0.9$, $P_{fa} \leq 1 \times 10^{-5}$. Specified UAV performance: $P_d \geq 0.9$, $P_{fa} \leq 0.06$. 'C' = comply. 'NC' = non-comply.

Channel	Simulated		Specified	
	P_{dc}	P_{fac}	P_d	P_{fa}
SSM at $23\,km$				
Air (Doppler GOCA-CFAR const. = 12, ref. cells = 104)				
Transmit power = $35\,W$	0.6	0	NC	C
Transmit power = $45\,W$	1	0	C	C
Surface (Doppler GOCA-CFAR const. = 12, ref. cells = 36)				
Transmit power = $45\,W$	1	0.01	C	NC
UAV at $19\,km$ (Transmit power = $45\,W$)				
Surface (Doppler GOCA-CFAR const. = 10, ref. cells = 36)				
Target radial velocity = $9.2\,m/s$ (towards)	1	0.01	C	C
Target radial velocity = $8.4\,m/s$	0.8	0.02	NC	C
Target radial velocity = $0\,m/s$	0	0.01	NC	C
Target radial velocity = $-6.9\,m/s$ (away)	0	0.01	NC	C
Target radial velocity = $-9.2\,m/s$	1	0.02	C	C
Surface (Doppler GOCA-CFAR const. = 4, ref. cells = 36)				
Target radial velocity = $0m/s$	0.6	0.1	NC	C
UAV at $7\,km$ (Transmit power = $45\,W$)				
Surface (Doppler GOCA-CFAR const. = 12, ref. cells = 36)				
Target radial velocity = $5.4\,m/s$	1	0.06	C	C
Target radial velocity = $0\,m/s$	0	0.05	NC	C
Target radial velocity = $-3.8\,m/s$	1	0.06	C	C

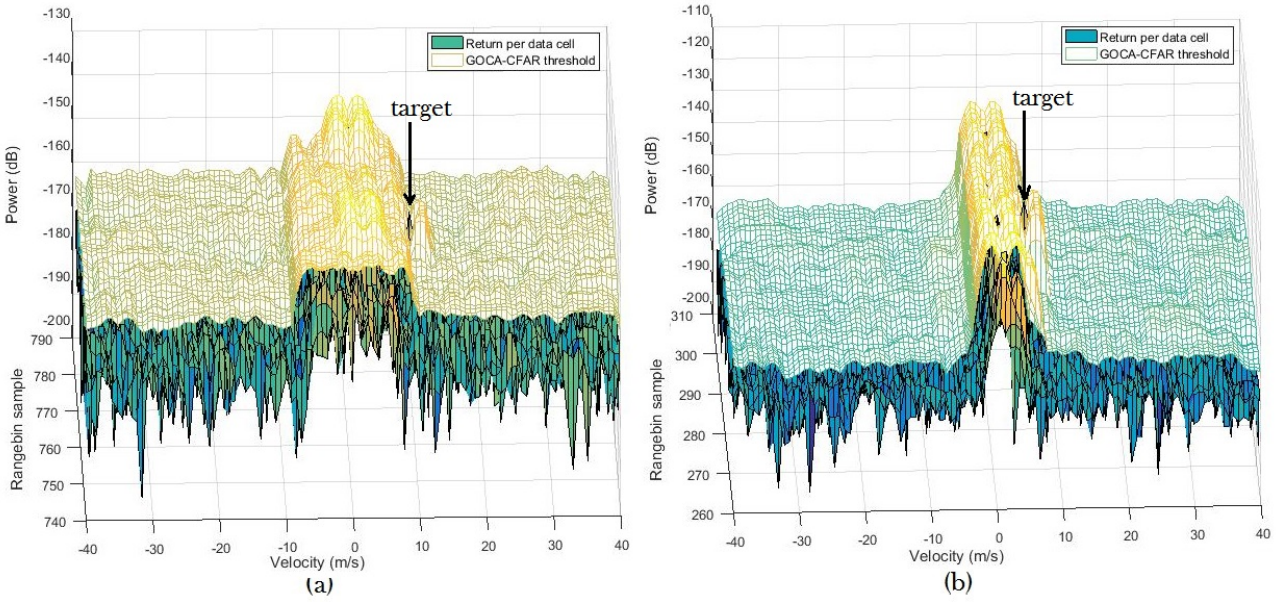

Fig. 4.24. UAV surface channel returns over various ranges simulation 2: (a) target at 19 km surface channel single unambiguous CPI power spectrum return over selected range bins with the apparent target position and GOCA-CFAR threshold indicated; (b) target at 7 km surface channel single unambiguous CPI power spectrum return over selected range bins with the apparent target position and GOCA-CFAR threshold indicated.

4.3.7 Comparison between Simulation 1 and 2

Table 4.11 is a comparison of the best results from simulation 1 and 2 that complied to the SSM and UAV system specifications. Both beamforming and scan patterns provided good detection results for the detection of the SSM at $23\,km$ in the air channel. It was expected that the detection performance would remain the same throughout all ranges less than 23 km. The sidelobes of the FFT for clutter close to the radar could cause false alarms at some range folds. However, this was not seen at the tested ranges. Surface channel detections of the SSM were good for both simulations, however it was in both instances without reliable Doppler velocity information.

For the UAV at $19\,km$ in the surface channel, the coherent high Doppler resolution GOCA-CFAR detector provided a slightly better (lower) P_{fac}, but detection degraded between between $9.2\,m/s$ and $-9.2\,m/s$. The non-coherent CA-CFAR detector (constant = 2) had a slightly higher P_{fac} but target detection performance remained the same at all specified velocities. The non-coherent constant threshold detector did not perform as well. It seemed that in a homogeneous environment with a small target SCR, the CFAR detectors performed the best.

For the UAV at $7\,km$ in the surface channel, the non-coherent constant threshold detector (threshold = $3 \times 10^{-8}\,V$) had the lowest P_{fac}. The coherent high Doppler resolution GOCA-CFAR detector provided reasonable results with a slightly higher P_{fac} but target detection degraded between $5.4\,m/s$ and $-3.8\,m/s$. The non-coherent CA-CFAR detector did not perform as well. It seemed that in a spiky environment with a large target SCR, the non-coherent constant threshold detector performed the best.

Table 4.11. Comparison of results from simulation 1 and 2.

Channel	Simulation 1		Simulation 2	
	P_{dc}	P_{fac}	P_{dc}	P_{fac}
SSM at $23\,km$				
Air	1	0	1	0
Surface	1	0.02	1	0.01
UAV at $19\,km$				
Surface	1	0.03 (CA-CFAR)	1 ($v \geq 9.2\,m/s$ or $v \leq -9.2\,m/s$)	0.02
UAV at $7\,km$				
Surface	1	0 (constant)	1 ($v \geq 5.4\,m/s$ or $v \leq -3.8\,m/s$)	0.06

Chapter 5

Conclusion and Recommendations

5.1 Conclusions

The objective of this study was to design and use a simulation model to evaluate the detection performance of different beamforming and scan pattern techniques for rotating maritime multi-beam electronically steered array surveillance radars. The detection performance was tested against a fast-moving ($333\,m/s$) SSM as well as a small ($0.05\,m^2$) slow-moving (0 to $15\,m/s$) UAV against sea clutter.

Coherent detection could typically be used in single and dual axis stacked beams for fast target surveillance. It was found that these targets move at radial velocities beyond the clutter velocity spectrum and CFAR threshold masking. Therefore, it could be detected with a high probability ($P_{dc} = 1$) and low false alarm rate ($P_{fac} = 0$) at medium PRF with a GOCA-CFAR detector. It required the clutter velocity bins to be suppressed (blind velocities). This was applicable at all ranges. For range bins that folded over the strong clutter returns close to the radar, the clutter suppression zone might have had to be extended to reduce false alarms from the FFT sidelobes. Dual axis beams could be used with azimuth beam scanning to maintain the required dwell time, despite a higher scan and rotation rate.

Non-coherent detection could typically be used in a single axis stack of beams for slow target detection, as time resources were limited to a single beamwidth dwell. A constant threshold detector could be used with non-coherent integration of low quantity pulse bursts at low PRF and time-varying gain for small targets at low velocities. This type of detector could provide good detection probabilities ($P_{dc} = 1$) with low false alarm rates ($P_{fac} = 0$) in a spiky clutter environment, provided that the sum beam of the lowest elevation beam and next higher clutter-free beam provided a good SCR (as was the case at near ranges). At a low SCR, the target became hidden in the clutter. The clutter peaks resulted in high false alarm rates (as was the case at far ranges). A CA-CFAR detector performed better at a low SCR ($P_{dc} = 1$ and $P_{fac} = 0.03$), provided that the environment was relatively homogeneous (as was the case in

far ranges).

A higher Doppler resolution (for example, 105 pulses at a dwell time of 21.7 ms compared to 30 pulses at a dwell time of 6.3 ms) coherent GOCA-CFAR detector could typically be used with a dual axis beam from a digital array with coherent integration across the multiple beams. This allowed a long dwell time at low PRF. This type of detection provided results comparable to non-coherent detection ($P_{dc} = 1$ and $P_{fac} = 0.02$ at close ranges; and $P_{dc} = 1$ and $P_{fac} = 0.06$ at far ranges). This was due to the high resolution that allowed for low velocity bins that were clutter-free. Clutter started forming a less spiky homogeneous environment reducing false alarms. The effect of speckle decorrelation due to the longer dwell time could improve detection performance, however, it was not known to what degree it had an effect. Inside the clutter velocity spectrum, the detection probability of a small target was not detectable ($P_{dc} = 0$). It was assumed that the performance would improve for larger RCS targets. The longer dwell time for the high Doppler resolution required that surface surveillance be completed in sectors and 360° coverage was only completed after a certain number of rotations. The air channel requires a specified antenna relative scan rate to complete 360° coverage per rotation.

5.2 Recommendations for future work

The simulation model provided the detection output based on a single rotation and scan. Multiple rotations and scans had to be run manually to build a picture of the detection performance across the clutter data. The model can be expanded to allow for automatic operation of a user defined number of multiple rotations and scans with offsets in the clutter data based on the rotation rate to determine the detection performance. If the detection threshold constant (or another variable) input is modified as an adjustable independent vector, it can result in a Monte Carlo simulation with an output vector of detection performance values. This is similar to the non-rotating antenna Monte Carlo simulations created in this study to determine threshold and transmit power values. With the multi-rotation and scan simulation update, the possibility exists to introduce scan-to-scan integration and consequent detection performance evaluation.

The real clutter data used in this study is from a non-rotating antenna. If real sea clutter data from a rotating antenna, can be obtained and introduced in the future, the additional decorrelating effects on the detection performance can be evaluated. Rotation rates could be comparable to that of naval surveillance radars. Additionally, it can be considered to use clutter data sets with pulse to pulse frequency agility in the NCPI processing channels to test and compare detection performance. Sea clutter returns can decorrelate from pulse to pulse with frequency agility [14].

References

[1] B. Tibbitts, E. Comstock, P. Covich, and R. Keane, "Naval Ship Design in the 21 st Century," *SNAME Transactions*, vol. 101, pp. 637–671, 1993.

[2] A. Tonnaer, "Dual Axis Multi-beam radars," in *IEEE 2013 International Conference on Radar*. IEEE, September 2013, pp. 412–416. [Online]. Available: https://ieeexplore.ieee.org/document/6652024

[3] Z. Ding, "A survey of radar resource management algorithms," in *IEEE 2008 Canadian Conference on Electrical and Computer Engineering*. IEEE, May 2008, pp. 1559–1564. [Online]. Available: https://ieeexplore.ieee.org/document/4564804

[4] C. Fowler, "Old Radar Types Never Die; They Just Phased Array or...55 Years of Trying to Avoid Mechanical Scan," *IEEE Aerosp. Electron. Syst. Mag.*, vol. 13, no. 9, pp. 24A–24L, September 1998. [Online]. Available: https://ieeexplore.ieee.org/document/715527

[5] J. Herd and M. Conway, "The Evolution to Modern Phased Array Architectures," *Proceedings of the IEEE*, vol. 104, no. 3, pp. 519–529, March 2016. [Online]. Available: https://ieeexplore.ieee.org/document/7350112

[6] S. Talisa, K. O'Haver, T. Comberiate, M. Sharp, and O. Somerlock, "Benefits of Digital Phased Array Radars," *Proceedings of the IEEE*, vol. 104, no. 3, pp. 530–543, March 2016. [Online]. Available: https://ieeexplore.ieee.org/document/7399690

[7] "Card Index of Radar Sets - Naval Radars," [Online]. Available: http://www.radartutorial.eu/19.kartei/07.naval/karte008.en.html. [Accessed Feb. 15, 2019]. [Online]. Available: http://www.radartutorial.eu/19.kartei/07.naval/karte008.en.html

[8] "MRR-3D NG Specification Sheet," [Online]. Available: http://www.thales7seas.com/html_2014/products/233/MRR3D_NG_HR.pdf. [Accessed Feb. 8, 2019]. [Online]. Available: http://www.thales7seas.com/html_2014/products/233/MRR3D_NG_HR.pdf

[9] "Hamina Class, Finland," [Online]. Available: https://thaimilitaryandasianregion.wordpress.com/2016/03/06/. [Accessed Feb. 15, 2019]. [Online]. Available: https://thaimilitaryandasianregion.wordpress.com/2016/03/06/

[10] "AN/SPY-1," [Online]. Available: https://en.wikipedia.org/wiki/AN/SPY-1. [Accessed Feb. 8, 2019]. [Online]. Available: https://en.wikipedia.org/wiki/AN/SPY-1

[11] J. Johansson, "ACE Deliverable 2.4-D1 Synthesis of Main Architectures Used in Modular Active Antennas," Tech. Rep., 2004. [Online]. Available: ace1.antennasvce.org/Dissemination/view/download?id_file=76

[12] J. van Bezouwen and M. Brandfass, "Technology Trends for Future Radar," *Microwave Journal*, p. 1, 2017. [Online]. Available: www.microwavejournal.com/articles/29367-technology-trends-for-future-radar

[13] P. Herselman, "2006 Fynmeet sea clutter measurement trial: Datasets," Tech. Rep., 2006. [Online]. Available: https://researchspace.csir.co.za/dspace/handle/10204/1847

[14] K. Ward, R. Tough, and W. Simon, *Sea Clutter: scattering, the K-distribution and radar performance, 2nd edition.* The Institution of Engineering and Technology, 2013. [Online]. Available: https://www2.theiet.org/resources/books/rsna/sea_clutter.cfm

[15] K. Ward, "Compound representation of high resolution sea clutter," *Electronics Letters*, vol. 17, no. 16, pp. 561–563, 8 1981. [Online]. Available: https://digital-library.theiet.org/content/journals/10.1049/el_19810394

[16] C. A. Balanis, *Antenna theory: analysis and design, 2nd edition.* John Wiley and Sons, Inc, 1997. [Online]. Available: https://books.google.co.za/books/about/ANTENNA_THEORY_ANALYSIS_AND_DESIGN_2ND_E.html?id=3qOrxC8IGNMC&redir_esc=y

[17] Y. Cong, G. Wang, and Z. Qi, "A Pattern Synthesis Method for Large Planar Antenna Array," *Progress In Electromagnetics Research M*, vol. 43, pp. 147–156, 2015. [Online]. Available: http://www.jpier.org/PIERM/pierm43/15.15072504.pdf

[18] M. A. Richards, J. A. Scheer, and W. A. Holm, *Principles of Modern Radar; Basic Principles.* Scitech Publishing, 2010. [Online]. Available: https://books.google.co.za/books/about/Principles_of_Modern_Radar.html?id=nD7tGAAACAAJ&redir_esc=y

[19] P. N. Nooy and J.-C. Debuisser, "Medium PRF Waveforms: an optimal solution for various applications in surface based radar," in *1998 28th European Microwave Conference.* IEEE, October 1998, pp. 572–577. [Online]. Available: https://ieeexplore.ieee.org/document/4139138

[20] M. I. Skolnik, *Radar Handbook, Third Edition.* McGRaw-Hill, 2008. [Online]. Available: https://www.amazon.com/Radar-Handbook-Third-Merrill-Skolnik/dp/0071485473

[21] H. L. van Trees, *Optimum array processing.* Wiley-Interscience, 2002. [Online]. Available: https://onlinelibrary.wiley.com/doi/book/10.1002/0471221104

[22] "Element and Array Radiation and Response Patterns," [Online]. Available: https://www.mathworks.com/help/phased/ug/element-and-array-radiation-patterns-and-responses.

html [Accessed May 15, 2019]. [Online]. Available: https://www.mathworks.com/help/phased/ug/element-and-array-radiation-patterns-and-responses.html

[23] M. A. Richards, *Fundamentals of Radar Signal Processing*. McGRaw-Hill, 2005. [Online]. Available: https://www.amazon.com/Fundamentals-Radar-Signal-Processing-Richards-ebook/dp/B005FQHFAM